SILICON PHOTONICS AND ITS APPLICATIONS IN MICROWAVE PHOTONICS

Weifeng Zhang

A thesis submitted to the
Faculty of Graduate and Postdoctoral Studies
in partial fulfillment of the requirements for the
Doctor of Philosophy Degree in Electrical and Computer Engineering

School of Electrical Engineering and Computer Science

Faculty of Engineering

University of Ottawa

ACKNOWLEDGMENTS

The work in this thesis is a five-year journey full of happiness and sadness. Looking back on this journey at this moment, I feel grateful for many helps from the people with whom I have met, discussed and learnt in the past five years. This thesis would have never been possible without the help from these people who contributed in various ways. I would like to express my heartfelt thanks and best wishes to all of them.

First and foremost, I would like to express my deepest gratitude to my supervisor, Professor Jianping Yao for his mentorship and guidance throughout this endeavor. His constant encouragement and patience are deeply appreciated. Without his trust and advice, this work would have never been possible.

Enormous appreciations are given to Ming Li, Wangzhe Li, Hiva Shahoei and Weilin Liu for their constant help. Inspiring insights from them and having valuable discussions with them help me to do my research as quickly and smoothly as possible.

I would also like to thank the following people, who are current or former colleagues working with me in the Microwave Photonics Research Laboratory at the School of Electrical Engineering and Computer Science, University of Ottawa: Jiejun Zhang, Xiang Chen, Peiwen Chen, Wentao Cui, Fanqi Kong, Hong Deng, Jishen Li, Tong Shao, Ting Hu, Yang Chen, Liang Gao, Fangjian Xing, Muguang Wang, Dan Zhu, Enming Xu, Olympio Coutinho, Xiuyou Han, Yiping Wang, and Ou Xu. Their strong supports and generous help greatly improve my research work. I will always cherish the good memories of working with them.

I would like to thank Jessica Zhang and Dan Deptuck in the CMC Microsystems, for providing the design tools and enabling the fabrication of the silicon-based on-chip devices in this thesis.

Finally, I would like to thank my beloved wife Jing Chen for her selfless devotion to our family and her strong accompany. I am eternally grateful to her for her continued love and support in all phases of this arduous process. I also would like to thank my big family including my mother, my father, my brother, my sister and my lovely nephews, for their immeasurable love and the support, materially and spiritually, throughout my life.

ABSTRACT

Thanks to its compatibility with the current CMOS technology and its potential of seamless integration with electronics, silicon photonics has been attracting an ever-increasing interest in recent years from both the academia and industry. By applying silicon photonic technology in microwave photonics, on-chip integration of microwave photonic systems could be implemented with improved performance including a much smaller size, better stability and lower power consumption. This thesis focuses on developing silicon-based photonic integrated circuits for microwave photonic applications. Two types of silicon-based on-chip devices, waveguide Bragg gratings and optical micro-cavity resonators, are designed, developed, and characterized, and the use of the developed devices in microwave photonic applications is studied.

After an introduction to silicon photonics and microwave photonics in Chapter 1 and an overview of microwave photonic signal generation and processing in Chpater2, in Chapter 3 a silicon-based on-chip phase-shifted waveguide Bragg grating (PS-WBG) is designed, fabricated and characterized, and its use for the implementation of a photonic temporal differentiator is experimentally demonstrated. To have a waveguide grating that is wavelength tunable, in Chapter 4 a tunable waveguide grating is proposed by incorporating a PN junction across the waveguide grating, to use the free-carrier plasma dispersion effect in silicon to achieve wavelength tuning. The use of a pair of wavelength-tunable waveguide gratings to form a wavelength-tunable Fabry-Perot resonator for microwave photonic signal processing is studied. Thanks to its electrical tunability, a high-speed electro-optic modulator, a tunable fractional-order photonic temporal differentiator and a tunable optical delay line

are experimentally demonstrated. To increase the bandwidth of a waveguide grating, in Chapter 5 a linearly chirped waveguide Bragg grating (LC-WBG) is designed, fabricated and evaluated. By incorporating two LC-WBGs in two arms of a Mach-Zehnder interferometer (MZI) structure, an on-chip optical spectral shaper is produced, which is used in a photonic microwave waveform generation system based on spectral-shaping and wavelength-to-time (SS-WTT) mapping for linearly chirped microwave waveform (LCMW) generation. To enable the LC-WBG to be electrically tuned, in Chapter 6 a lateral PN junction is introduced in the grating and thus an electrically tunable LC-WBG is realized. By incorporating two tunable LC-WBGs in a Michelson interferometer structure, an electrically tunable optical spectral shaper is made. By applying the fabricated spectral shaper in an SS-WTT mapping system, a continuously tunable LCMW is experimentally generated.

Compared with a waveguide Bragg grating device, an on-chip optical micro-cavity resonator usually has a much smaller dimension, which is of help to increase the integration density and reduce the power consumption. Different on-chip optical micro-cavity resonators are studied in this thesis. In Chapter 7, an on-chip symmetric MZI incorporating multiple cascaded microring resonators is proposed. By controlling the radii of the rings, the MZI could be designed to have a spectral response with a linearly-varying free spectral range (FSR), which could be used in photonic generation of an LCMW, and to have a multi-channel spectral response with identical channel spacing, which could be used in the implementation of an independently tunable multi-channel fractional-order temporal differentiator. To further reduce the footprint of an optical micro-cavity resonator, in Chapter 8 an ultra-compact microdisk resonator (MDR) with a single-mode operation and an ultra-high Q-factor is proposed, fabricated and evaluated, and its use for the implementation of a

microwave photonic filter and an optical delay line is experimentally demonstrated. To enable the MDR to be electrically tunable, in Chapter 9 an electrically tunable MDR is realized by incorporating a lateral PN junction in the disk. The use of the fabricated MDR in microwave photonic applications such as a high-speed electro-optic modulator, a tunable photonic temporal differentiator and a tunable optical delay line is experimentally demonstrated.

TABLE OF CONTENTS

LIST OF FIGURES

LIST OF TABLES

LIST OF ACRONYMS

AC	Alternating current
AWG	Arbitrary waveform generator
CMOS	Complementary metal-oxide-semiconductor
CW	Continuous wave
DAC	Digital-to-analog converter
DC	Direct current
DCF	Dispersion compensating fiber
DLP	Discrete layer peeling
DST	Space-to-time
EDFA	Erbium-doped fiber amplifier
FBG	Fiber Bragg grating
FP	Fabry-Perot
FWHM	Full-width at half maximum
IM	Intensity modulator
LCMW	Linearly chirped microwave waveform
LC-FBG	Linearly chirped fiber Bragg grating
LC-WBG	Linearly chirped waveguide Bragg grating
MC-FBG	Multi-channel fiber Bragg grating
MDR	Microdisk resonator
MLL	Mode-locked laser
MRR	Microring resonator
MZI	Mach-Zehnder interferometer
MZM	Mach-Zehnder modulator
OSC	Oscilloscope
PC	Polarization controller

PD	Photodetector
PIC	Photonic integrated circuit
POL	Polarizer
PS-FBG	Phase-shifted fiber Bragg grating
PS-WBG	Phase-shifted waveguide Bragg grating
Q-factor	Quality factor
SEM	Scanning electron microscope
SOI	Silicon-on-insulator
SOP	State of polarization
SS	Spectral shaping
SS-WTT	Spectral shaping and wavelength-to-time
TBWP	Time-bandwidth product
TE	Transverse electrical-filed
TFBG	Tilted fiber Bragg grating
TLS	Tunable laser source
WBG	Waveguide Bragg grating
WDM	Wavelength-division multiplexing
WGM	Whispering gallery mode
WTT	Wavelength-to-time
UWBG	Uniform waveguide Bragg grating

CHAPTER 1 INTRODUCTION

1.1 Silicon photonics

Silicon photonics is a field that studies the use of state-of-the-art complementary metal-oxide-semiconductor (CMOS) processing technology to develop and fabricate photonic devices which use silicon as an optical medium [1, 2]. Benefiting from its high index contrast between silicon (n = 3.45) and silica (n = 1.45), a silicon-based waveguide with a core dimension of several hundreds of nanometers exhibits a strong light confinement, which makes it possible to scale an individual photonic device in an unprecedentedly ultra-compact footprint and helps enhance nonlinear light-matter interaction when a light wave travels in the waveguide. Furthermore, intrinsic silicon is transparent from its indirect bandgap wavelength of 1.1 μm out to about 100 μm, covering the key optical wavelengths of 1310 and 1550 nm widely used for optical communications. In addition, the compatibility of silicon photonics with the current CMOS technology and its potential for seamless integration with electronics enable a potentially low-cost development of photonic integrated circuits (PICs) with high volume production. Therefore, silicon photonics has been attracting an ever-increasing interest in recent years both from the academia and industry, as an enabling and promising photonic integration platform, which holds a significant potential for diverse applications including optical interconnects [3], low-cost telecommunications [4], nano-optomechanics [5], bio-sensing [6], quantum communication [7], nonlinear optics [8] and very-long-wavelength integrated photonics [9]. In the last few years, intensive efforts have been devoted and significant breakthroughs have been made in implementing both

passive and active optical components on silicon chips [10], such as low-loss optical waveguides [11], various optical filters [12], add-drop multiplexers [13], high-speed modulators [14], and Ge-doped photodetectors [15]. Among various silicon photonic components, waveguide Bragg gratings and optical micro-cavity resonators are two types of components which can be used for microwave photonic applications. In the following, an introduction to waveguide Bragg gratings and optical micro-cavity resonators is presented. The tuning mechanisms are also discussed.

1.1.1 Waveguide Bragg grating

A waveguide Bragg grating (WBG) is a fundamental silicon photonic component [16] that is widely used as an optical spectral filter typically reflecting a light wave in a specific band of wavelength and transmitting light in all other wavelengths. A WBG has a structure with a periodic refractive index modulation along the optical mode propagation direction. Unlike a fiber Bragg grating (FBG) where the index modulation is done by exposing the photosensitive fiber core to an intense ultraviolet light using a phase mask, the index modulation of a WBG is usually done by varying the physical waveguide dimension periodically, for example, creating the periodic corrugations on top of the waveguide [17] or in the waveguide sidewalls [18]. When an incident light wave with a wavelength travelling in the WBG satisfies the Bragg condition, the light wave would be reflected; otherwise, the light wave would be transmitted. In sharp contrast to a weak index modulation in an FBG, a WBG usually has a much stronger index modulation, which is of help to have a broader reflection bandwidth with a shorter grating length. Recently, an extensive research effort has been directed to study the use of silicon photonic technology for the implementation of

WBGs, and different WBG structures have been reported with different spectral characteristics [19, 20, 21, 22, 23, 24].

Among the different WBGs, a uniform waveguide Bragg grating (UWBG) is a simplest class of gratings, which has a uniform and periodic refractive index modulation profile along the waveguide [19, 20]. Thanks to strong index modulation in the WBG, an UWBG usually has strong reflection at a wavelength satisfying the Bragg condition, which could be used to form a distributed feedback laser [25], a distributed Bragg reflector laser [26] and an add-drop filter [27]. However, in its reflection spectrum, large power fluctuations, known as sidelobes, are usually observed at the wavelengths around the main lobe, which are unwanted for most applications. To suppress the sidelobes, apodization techniques are widely employed in the design of UWBGs [28]. For example, in an UWBG, its grating strength could be designed to have a Gaussian-shape or Cosine-shape profile, which could effectively suppress the unwanted sidelobes in the reflection spectrum.

In addition to an UWBG, a phase-shifted waveguide Bragg grating (PS-WBG) is another popular class of gratings [21]. By introducing a phase-shifted block in the middle of an UWBG, a PS-WBG is produced. Owing to the phase-shift block in the middle, a compact Fabry-Perot cavity is formed with the gratings on each side functioning as a mirror. Therefore, in the transmission spectrum of a PS-WBG, a sharp resonance window within the stop band is generated. Recently, a silicon-based PS-WBG with an ultra-narrow transmission window as small as approximately 15 pm has been reported [22]. Thanks to the unique feature of an ultra-narrow transmission window in the stopband, a PS-WBG is considered a key photonic component which can find various applications such as narrowband filtering [29], optical sensing [30], and optical signal processing [31].

By linearly varying the grating period or effective index modulation along a grating, a linearly chirped waveguide Bragg grating (LC-WBG) can be generated [23, 24]. In an LC-WBG, the refractive index profile or the period of the grating is modified to have a linear variation. Thus, the resulted Bragg wavelength changes linearly along the grating, which finally broadens the spectrum. More importantly, because of the linearly varying period or index modulation, an incident light wave that is travelling along the grating will be reflected at the different position depending on the wavelength. By tuning the wavelength of the incident light wave, a tunable time delay can be achieved. For example, if the period variation is increasing along the direction of the forward propagating wave, a light wave with a longer wavelength will be reflected later than that with a shorter wavelength. Thus, a light wave with a longer wavelength has a larger time delay. This wavelength-dependent delay, termed dispersion, is a very useful feature, which could be used for chromatic dispersion compensation [32], optical beamforming [33], optical communication networking [34], and optical coherence tomography [35].

1.1.2 Optical micro-cavity resonator

Compared with a waveguide Bragg grating device, an on-chip optical micro-cavity resonator usually has much smaller dimensions, which is of help to increase the integration density and reduce the power consumption. Moreover, thanks to its small mode volume of the optical filed confined in a micro-cavity resonator, the light-matter interaction could be significantly enhanced, which is useful in strengthening its optical nonlinearities.

As the most common class of optical micro-cavity resonator, a microring resonator (MRR) has been extensively researched [36]. A typical MRR consists of a loop waveguide, known

as ring, and a bus waveguide in close proximity to the ring. Such configuration often refers to as an all-pass MRR. An incident light wave travelling along the bus waveguide would be coupled into the ring via evanescent field coupling. If the coupled light wave undergoes a phase change with an integer multiple of 2π after each round trip in the ring, the light wave in the ring would be exactly in-phase with the incoming light. Thus, constructive interference happens, and the wavelength is one resonance wavelength of the ring. If the light wave does not satisfy the phase condition, the light wave would be transmitted through the bus waveguide. In order to collect the resonance light wave of the ring, an additional waveguide could be placed in the opposite side of the ring. Such configuration refers as to an add-drop MRR. Compared with an all-pass MRR, an add-drop MRR has four ports, which has more widespread applications. For example, an add-drop MRR can be employed as a compact wavelength filter that is widely used in a wavelength-division multiplexing (WDM) network [37]. To enable a filter to have a flat top, one solution is to cascade multiple MRRs with specifically designed coupling gaps [38]. Thanks to the strong light-confining capacity of a ring resonator, an MRR could also be used as an optical delay line with a large time delay. For example, in [39] an MRR was used as an on-chip optical delay line with a time delay as large as 500 ps To make an optical delay line with a wide bandwidth, a double-series-coupling multiple MRRs, known as a coupled resonator optical waveguide, could be employed [40].

Also as a common class of on-chip optical micro-cavity resonators, a microdisk resonator (MDR) exhibits attractive advantages in terms of footprint and light-confining capacity [41]. Distinct from an MRR with two etched sidewalls, an MDR has only one etched sidewall. Owing to the fabrication imperfections, sidewall roughness always exists, which would cause

a scattering loss to the confined optical field in the resonator. Since an MDR has only one etched sidewall, it has a much smaller scattering loss, which is important to have an improved light-confining capacity. In addition, the radius of an MDR can be smaller than that of a ring resonator for a given light-confining capacity. Note that the light-confining capacity can be characterized by its Q-factor, which is calculated by the ratio between its resonant wavelength and its 3-dB bandwidth. However, in sharp contrast to widespread applications of MRRs, much less demonstrations have been reported to the use of MDRs in silicon photonics. From the perspective of a chip, a smaller physical size of an individual device is always highly preferred for high-density integration with a low overall cost. The main limitation hindering MDRs from wide applications is the co-existing multiple different-order whispering-gallery-modes (WGMs) since a single-mode operation over the entire free spectral range (FSR) is usually required. In addition, resonance-splitting as a result of Rayleigh scattering from the disk sidewall roughness of an MDR would distort its ideal Lorentzian-shaped spectrum. To circumvent these limitations, different approaches have been proposed. Non-fully etched MDR with a radius as large as 20 μm has been demonstrated using a thin pedestal layer of silicon under the disk to improve the Q-factor [42]. Thanks to the pedestal layer under the disk, its Q-factor is largely increased to $2x10^6$ [42]. By using a specifically-designed wrap-around bus waveguide, a planar silicon nitride MDR working in single mode has been demonstrated [43]. Therefore, an MDR supporting single-mode operation with no resonance-splitting can be realized, which could find potential applications in optical systems where an MDR with a high Q-factor is needed.

1.1.3 Tuning mechanisms

Generally, the optical properties of a passive silicon photonic device are predetermined by its design, which are usually fixed once the devices are fabricated. However, in practical applications, it is highly needed that the optical properties of silicon photonic devices could be tuned. In order to meet such need, in silicon photonics, two tuning mechanisms, the thermal-optic effect [44] and the free-carrier plasma dispersion effect [45], are widely used. Thermal-optic effect is actually a temperature-dependent effect, in which the refractive index of silicon is modulated by the temperature. When the temperature is raised or lowered, the refractive index of silicon is changed. Owing to its large thermo-optic coefficient of 1.8×10^{-4} K^{-1}, thermal-optic effect is an attractive option in silicon. The common approach is to place a high-resistivity metallic micro-heater on the top of silicon waveguide [46]. By controlling the applied direct-current (DC) voltage on the micro-heater, the heat is generated and varied, and hence the optical property of the device is tuned. The main advantage of this tuning mechanism is its simple construction structure, which highly ease the fabrication. However, the incorporated metal also brings a problem of light absorption, which would lead to a large optical loss. To overcome this problem, a thick silicon dioxide layer (SiO_2) is typically required between the silicon waveguide and the metallic micro-heater to prevent the light absorption and thus reduce the loss. In the meanwhile, the introduction of the SiO_2 layer would impede heat transport and dissipation owing to the low thermal conductivity of SiO_2 as small as 1.44 $W\cdot m^{-1}$ K^{-1} [47], which lowers the tuning efficiency. Moreover, its slow response in the scale of micro-seconds makes it unsuitable for ultra-fast tuning or high-speed modulation required by practical applications, for example, in modern telecommunications applications, and its comparatively high drive power (several milliwatts) is also a main shortcoming. To achieve an ultra-fast tuning, free-carrier plasma dispersion effect is a

feasible option in which silicon's refractive index is changed with the free-carrier density in the waveguide. For example, when the free-carrier density is increased, the refractive index of silicon waveguide is decreased. Usually, the free-carrier density in the waveguide could be manipulated by the methods of carrier injection, accumulation or depletion. The main advantage of this tuning mechanism is its ultra-fast response in a scale of nano-seconds, which makes an ultra-fast tuning or a high-speed electro-optic modulation possible in silicon. Three typical configurations including forward biased p-i-n diode [48], MOS capacitor [49], and reverse biased PN junction [50] have been proposed and demonstrated to achieve high-speed phase modulation, which presents the exceptional advantages of low-power consumption, compact footprint, and ultra-fast response. Free-carrier plasma dispersion effect is a strong tuning mechanism that allows the implementations of tunable silicon photonic devices, significantly boosting the development of silicon photonics in terms of device performance and integration level.

1.1.4 Fabrication

Prototype fabrication is a critical step in the silicon photonic ecosystem. Thanks to the worldwide rapidly-increasing interest in developing silicon photonic devices, a fabless model has been possible, which makes direct use of multi-project-wafer runs provided by commercial foundries for fabrication. In this way, the fabrication cost is largely decreased by allowing multiple users to share a run [51]. In this thesis work, the passive silicon components are usually fabricated using a CMOS-compatible process with 193-nm deep ultraviolet lithography at IMEC in Belgium [52], and the active silicon components are usually fabricated using a CMOS-compatible process with 248-nm deep ultraviolet lithography at IME in Singapore [53]. In addition, the commercial software package

including MODE Solutions, FDTD Solutions, DEVICE, and INTERCONNECT from the Lumerical Inc. is used to simulate the different optical devices [54], and the layout is done by using the commercial software Pyxis from the Mentor Graphics Ltd. [55]. Considering the impact of the fabrication imperfections such as sidewall roughness and lithography smoothing of the grating on the performance of the fabricated device, parameter variation of the proposed devices is required in the layout phase.

1.2 Microwave photonics

Microwave photonics is a field that studies the interactions between microwave and optical waves for the generation, processing, control and distribution of microwave signals by means of photonics [56, 57, 58, 59, 60, 61]. The key motivation of using photonics for microwave applications is the wide bandwidth and low loss offered by modern photonics, which makes the implementation of certain important functions possible while in the electrical domain the same functions may not be realizable or the systems become extremely complicated and costly. In the past few years, there has been an increasing effort in researching microwave photonic techniques for different applications such as broadband wireless access networks, sensor networks, radar, satellite communications, instrumentation, and warfare systems. Among the different applications, photonic generation of arbitrary microwave waveforms [62] and photonic processing of microwave signals [63, 64] are two important topics and have been extensively studied. In the following, an introduction to photonic generation of arbitrary microwave waveforms and photonic processing of microwave signals is presented.

1.2.1 Photonic generation of arbitrary microwave waveforms

Microwave waveforms with a large time-bandwidth product (TBWP) offer a great potential for applications in communication systems to increase data transmission rate [65, 66] and in modern radar systems to enhance the range resolution [67]. Particularly, a linearly chirped microwave waveform (LCMW) with a large TBWP in the order of 10^2 or 10^3, is highly preferred for microwave pulse compression in modern radar systems. In the past, LCMWs are usually generated electronically using a voltage controlled electronic oscillator [68] or a digital waveform generator [69]. However, because of the relatively low speed of electronic devices, electronically generated LCMWs are limited in the central frequency and bandwidth, usually less than a few to tens of gigahertz, which is too small to meet the requirements of future radar systems. In addition, the time jitter, the limited speed and the nonlinearity of currently available digital-to-analog converters (DACs) set a limitation on the sampling rate, which inhibits from generating microwave waveforms at a high frequency with a large TBWP. To circumvent the obstacles, the generation of microwave waveforms in the optical domain has been considered a potential solution, which brings the inherent advantages of broad bandwidth and low loss offered by photonics to the microwave systems. In addition, the large flexibility in frequency tuning and system reconfiguration provides additional advantages. In the past few years, numerous approaches to the generation of LCMWs based on photonics have been proposed and demonstrated.

Firstly, an LCMW can be generated by beating two complementarily parabolically phase-modulated optical pulses [70, 71] or simply two linearly chirped optical pulses with different chirp rates [72, 73, 74]. In an optical beating system, by beating two light waves that are complementarily phase modulated by a parabolic microwave waveform or two linearly chirped optical pulses with different chirp rates at a photodetector (PD), an LCMW could be

generated. However, the large phase noise of the generated LCMW is a problem. To reduce the phase noise, one solution is to use an optical filter to select two phase-modulated light waves from an externally modulated light wave, or send an ultra-short chirp-free pulse from a mode-locked laser (MLL) into two dispersive elements with different dispersions to get the two linearly chirped optical pulses. However, the major limitation in beating two phase-correlated light waves is that the TBWP of the generated LCMW is usually small, only in the order of 10 due to a small phase modulation index, and the usage of the optical filter limits the large frequency tuning range of the generated LCMWs. The major limitation in beating two linearly chirped optical pulses is that the system lacks of the reconfigurability. The generated LCMW cannot be changed once the two dispersive elements are selected.

An LCMW can also be generated based on direct space-to-time (DST) mapping. In a typical DST mapping system, an ultrashort optical pulse is launched into an optical pulse shaper to generate a pulse burst with increasing or decreasing temporal spacing. After detection at a PD, an LCMW with its chirp rate determined by the profile of the temporal spacing is generated [75, 76]. However, the optical pulse shaper is a key device and the path number determines the number of the circles of the generated LCMW, which hinders the elevation of the TBWP.

Optical spectral-shaping and wavelength-to-time (SS-WTT) mapping is considered one of the most important techniques [77, 78], thanks to the flexibility in tailoring the shape of a waveform by controlling the optical spectral shaper. A typical SS-WTT mapping system consists of an ultra-short pulse source, an optical spectral shaper, a dispersive element, and a PD. The optical spectral shaper is the key device which is specifically designed to have a spectral response with a shape that is a scaled version of the microwave waveform to be

generated. For LCMW generation, the spectral shaper usually has a spectral response with an increasing or decreasing FSR. By passing an ultra-short pulse (with a flat spectrum) through this spectral shaper, and allowing the spectrally shaped pulse to undergo WTT mapping in a dispersive element, an LCMW is generated at the output of a PD. Several approaches based on SS-WTT have been proposed recently to generate an LCMW. In [79], a spectral shaper consisting of two superimposed linearly chirped fiber Bragg gratings (LC-FBGs) is proposed for LCMW generation. The generated LCMW has a central frequency of 15 GHz and a TBWP of 37.5. In [80], a single spatially discrete FBG acting as a spectral shaper is proposed and demonstrated for LCMW generation. The generated LCMW has a central frequency of 27.5 GHz and a TBWP of 16.8. Moreover, a spectral shaper having a Mach-Zehnder interferometer (MZI) structure incorporating an optically pumped LC-FBG in one arm is also reported for LCMW generation [81]. The central frequency of the generated microwave waveform is about 39.54 GHz and a TBWP of 24.5. The major limitation of these approaches is the use of an FBG, which is highly sensitive to environment changes, thus the system stability is poor, or dedicated packaging must be made to increase the stability. In addition, the TBWPs of the generated LCMWs are too small which may not meet the requirements for practical applications. To have a large TBWP, in [82, 83], a spectral shaper is incorporated in one arm of an MZI with its function similar to an LC-FBG is proposed. An LCMW with a TBWP as large as 600 is generated. Although the stability is improved, the size is still very large and the cost is still very high.

To overcome the inherent disadvantages of a fiber-optics based system, it is desirable that a waveform generation system is implemented based on PICs [84, 85, 86]. Recently, chip-level optical spectral shapers have been proposed and demonstrated for LCWM generation.

In [87], a silicon-based spectral shaper consisting of multiple cascaded MRRs is proposed. By thermally tuning the rings, a spectral shaper with an increasing or decreasing FSR is obtained. The generation of an LCMW with a central frequency of 8 GH is demonstrated. However, due to the limited thermal-tuning range, the TBWP and the chirp rate of the generated LCMW are limited. In [88], a silicon-based integrated distributed Fabry–Perot cavity is used as a spectral shaper for the generation of an LCMW. Again, due to the limited group delay, the generated LCMW has a central frequency of 20 GHz and a small TBWP of 14.5. Photonic generation of an LCMW with a high TBWP using a silicon-based on-chip optical spectral shaper based on SS-WTT mapping is a research point in this thesis.

1.2.2 Photonic processing of microwave signals

Photonic processing of microwave signals has also been a topic of interest and has been intensively investigated in the last few years. Compared with the conventional microwave signal processing techniques based on digital or analog electronic circuits, photonic-assisted signal processing solutions provide a much higher speed, wider bandwidth and greater tuning range. Various techniques have been proposed and demonstrated. These signal processors include microwave photonic filters [89], photonic temporal differentiators and integrators [90], Hilbert transformers [91], microwave mixers [92], and microwave phase shifters [93]. Among the different signal processors, photonic temporal differentiator is a basic signal processing block for advanced computing and information processing circuits. In addition, microwave photonic delay line, capable of controlling the time delay of a microwave signal in the optical domain, is a basic and important element that can find applications in radar, communications, and signal processing. An introduction to photonic temporal differentiator and microwave photonic delay line is presented.

Photonic temporal differentiator, performing temporal differentiation of the complex envelope of an arbitrary optical signal, is a basic signal processing block, which can find numerous applications such as in ultrafast computing [94], ultra-short pulse generation [95, 96] and ultra-short pulse characterization [97]. In general, a photonic temporal differentiator can be realized using an optical device that has a transfer function given by $[j(\omega - \omega_0)]^n$, where n is the differentiation order, ω is the optical frequency and ω_0 is the optical carrier frequency. When the differentiation order n is not one, the operator is generalized to be a fractional-order photonic temporal differentiator [98, 99]. Due to the inherent advantages such as much higher speed and wider bandwidth offered by photonics, a temporal differentiator implemented in the optical domain can perform the differentiation at an ultra-high speed with a wideband operation, which is not achievable by the electronic counterpart. Different schemes based on fiber optics have been proposed. For example, a photonic temporal differentiator is implemented using a PS-FBG [100]. The temporal differentiator based on a PS-FBG is relatively easy to implement, but it is highly sensitive to environmental changes, which cause a poor stability of the system. To have a better stability, integrate solutions are highly preferred. Recently, the integrated photonic temporal differentiator has been demonstrated using a silicon-based MRR [101] or a silicon-based PS-WBG [102]. The silicon-based temporal differentiator based on an MRR or a PS-WBG has the advantages of small footprint and can be potentially integrated with other optical and electronic devices. However, the differentiation order of the differentiators is one, which is fixed and not tunable. Due to the potential applications in pulse shaping, signal processing and ultrafast optical signal coding, a temporal differentiator with a tunable fractional-order is highly desired. Recently, a tunable fractional-order temporal differentiator using a polarization-dependent

silicon-based MRR incorporating a multimode interference (MMI) coupler is experimentally demonstrated [103]. By continuously tuning the polarization state of the input light wave, the fractional order of the differentiator is continuously tuned. However, the change of the polarization state usually involves mechanical movement, making the system complicated with low accuracy. To generate an electrically tunable fractional-order photonic temporal differentiator using a silicon-based on-chip component is another research point in this thesis.

Microwave photonic delay line, capable of controlling the time delay of a microwave signal in the optical domain, is a basic and important element that can find applications in radar, communications, and signal processing. Compared with a conventional electrical delay line, a photonic microwave delay line usually has a wider bandwidth and large tunability. A typical microwave photonic delay line system consists of a tunable laser source (TLS), an intensity modulator (IM), an optical delay line and a PD. The microwave signal to be delayed is modulated on a light wave via an IM, and by passing the modulated light wave through an optical delay line and applying at a PD, the microwave signal is recovered. Thanks to the dispersion in an optical delay line, the input light wave with different wavelength experience different time delays by passing through the optical delay line, and thus the retrieved microwave signal has the different time delays. By tuning the wavelength of the input light wave, a tunable time delay of the microwave signal is achieved. To reduce the system cost, it is highly preferred a cheaper laser diode is used to replace the TLS. Thus, a tunable optical delay line is an essential element in a microwave photonic delay line system.

So far, various techniques have been demonstrated to achieve a tunable optical delay line. For example, a linearly chirped fiber Bragg grating (LC-FBG) is a strong candidate to act as an optical delay line. However, the optical properties of the FBG are predetermined by the

design and fixed once fabricated, which makes the LC-FBG unfeasible to realize a tunable optical delay line. To overcome this obstacle, several approached are proposed including mechanical [104, 105, 106], or thermal [107] tuning of an LC-FBG. However, the tuning speed is very low. Moreover, the stability of the system is poor, especially for mechanical tuning. To have a better stability, silicon-based PICs can also be employed to realize an optical delay line. A straightforward approach is use the waveguides with different propagation lengths. By incorporating an optical switch to select the different path, different time delay could be achieved [108, 109]. For example, an eight-channel waveguide optical delay line network with a tunable time delay of 12.3 ps over a frequency range of 2-20 GHz was experimentally demonstrated. However, the main shortcoming is the small time delay. To achieve a large time delay, the waveguide length needs to be largely increased, which is unfeasible because of the waveguide loss and chip dimensions. Thanks to its strong light-confining capacity, MRRs can also be used as an optical delay line either by single ring or cascading multiple ring resonators [110, 111, 112]. However, the narrow working bandwidth and the large suffering loss are the main limitations. In addition to MRRs, a WBG is a strong candidate to function as an optical delay line. By apodizing the grating in the way of varying the rib width along the gratings, the light wave with different wavelengths would be reflected at the different position in the grating. Thus, an optical delay line is realized, and the tuning of the time delay can be done electronically or thermally [113, 114, 115]. Making a tunable optical delay line with a wide operation bandwidth and large tunability using a silicon-based on-chip component is also a research point in this thesis.

1.3 Major contributions of this research

This thesis focuses on developing silicon-based photonic integrated circuits for microwave photonic applications. Two types of silicon-based on-chip devices, waveguide Bragg gratings and optical micro-cavity resonators, are designed, developed, and characterized, and the use of the developed silicon photonic devices for microwave photonic applications is studied.

1) A silicon-based on-chip phase-shifted waveguide Bragg grating (PS-WBG) is designed, fabricated and characterized, and its use for the implementation of a photonic temporal differentiator is experimentally demonstrated. The fabricated PS-WBG is measured to have a reflection notch with a 3-dB bandwidth of approximately 0.3 nm, and by using the fabricated PS-WBG, a photonic temporal differentiator with a bandwidth of 37.5 GHz is experimentally demonstrated.

2) To have a waveguide grating that is wavelength tunable, we propose to implement a tunable waveguide grating by incorporating a PN junction across the waveguide grating, to use the free-carrier plasma dispersion effect in silicon to achieve wavelength tuning. The use of a pair of wavelength-tunable waveguide gratings to form a wavelength-tunable Fabry-Perot resonator for microwave photonic signal processing is studied. Thanks to its electrical tunability, a high-speed electro-optic modulator, a tunable fractional-order photonic temporal differentiator and a tunable optical delay line are experimentally demonstrated. The use of the tunable resonator for implementation of an electro-optic modulator with a 3-dB modulation bandwidth of ~5.6 GHz is experimentally demonstrated, and the performance of using the resonator to perform modulation of a 3.5 Gb/s 2^7-1 non-return-to-zero pseudorandom binary sequence is evaluated. In addition, the use of the tunable resonator for the implementation for a

tunable fractional-order photonic temporal differentiator with a tunable differentiation order from 0.99 to 1.53 and an electrically tunable optical delay-line with a tunable time delay as large as 110 ps is also experimentally demonstrated.

3) To increase the bandwidth of a waveguide grating, a linearly chirped waveguide Bragg grating (LC-WBG) is designed, fabricated and evaluated. The fabricated LC-WBG is measured to have a time delay of 228 ps and a bandwidth of 11 nm. By incorporating two LC-WBGs in two arms of an MZI structure, an on-chip optical spectral shaper with a spectral response of a linearly-varying FSR is produced. The fabricated spectral shaper was applied in a photonic microwave waveform generation system based on SS-WTT mapping, and an LCMW with a large TBWP is experimentally generated. By using a spectral shaper with the length of the offset waveguide equal to zero, an LCMW having a symmetrical chirp profile is experimentally generated. The positive and negative chirp rates are, respectively, 5.4 GHz/ns and -4.9 GHz/ns, and the TBWP is 359.7. By using a spectral shaper with the length of the offset waveguide equal to the length of the gratings, an LCMW having a uniform chirp profile is experimentally generated. The chirp rate is 1.54 GHz/ns and the TBWP is 615. This is the largest TBWP ever reported based on SS-WTT mapping technique, to the best of our knowledge.

4) To enable the LC-WBG could be electrically tuned, a lateral PN junction is introduced in the grating and thus an electrically tunable LC-WBG is realized. By incorporating two tunable LC-WBGs in a Michelson interferometer structure, an electrically tunable optical spectral shaper is made. By applying the fabricated spectral shaper in an SS-WTT mapping system, a continuously tunable LCMW is experimentally generated.

5) An on-chip symmetric MZI incorporating multiple cascaded microring resonators is proposed. By specifically designing the radii of the rings, the interferometer could be designed to have a spectral response with a linearly-varying FSR. By applying the interferometer as an optical spectral shaper in an SS-WTT mapping system, a largely chirped microwave waveform with a bandwidth of 15.55 GHz and a chirp rate of 17.2 GHz/ns is experimentally generated. By specifically designing the radii of the rings, the interferometer could also be designed to have a multi-channel spectral response with identical channel spacing. Thanks to two-photon absorption induced nonlinear thermo-optic effect in the ring, the phase responses of the rings could be independently changed by tuning the power of the pumping light at one resonant wavelength of the ring. The use of the fabricated interferometer in the implementation of a five-channel temporal differentiator with independently tunable differentiation order is experimentally demonstrated.

6) To further reduce the footprint of an optical micro-cavity resonator, an ultra-compact microdisk resonator (MDR) with a single-mode operation and an ultra-high Q-factor is proposed, fabricated and evaluated. The key features of the fabricated MDR include ultra-compact footprint, single-mode operation, no resonance-splitting, and ultra-high Q-factor, which make the MDR have a high potential for microwave photonic applications. The use of the fabricated MDR for the implementation for a microwave photonic filter and an optical delay line is experimentally demonstrated.

7) To enable the MDR could be electrically tuned, by incorporating a lateral PN junction in the disk, an electrically tunable MDR is realized. Thanks to its electrical tunability, the use of the fabricated MDR in microwave photonic applications such as a high-speed

electro-optic modulator, a tunable photonic temporal differentiator and a tunable optical delay line is experimentally demonstrated. An electro-optic modulator with a 3-dB modulation bandwidth of ~30.5 GHz is experimentally demonstrated. In addition, a tunable fractional-order photonic temporal differentiator with a tunable differentiation order from 0.38 to 1.53 and an electrically tunable optical delay-line with a tunable time delay as large as 72 ps is also experimentally demonstrated.

1.4 Organization of this thesis

The thesis consists of ten chapters.

In Chapter 1, a brief review of silicon photonic fundamentals and microwave photonic applications with an emphasis on photonic generation of microwave waveform and photonic processing microwave signals is introduced, as well as the summarized major contributions of the research.

In Chapter 2, a theoretical overview of photonic microwave arbitrary waveform generation system based on spectral-shaping and wavelength-to-time mapping is presented, and the theoretical principles of photonic temporal differentiator and microwave photonic delay line are introduced. Some conclusions will be used in the following chapters.

In Chapter 3, a silicon-based on-chip PS-WBG is designed, fabricated and characterized, and its use for the implementation of a photonic temporal differentiator is experimentally demonstrated.

In Chapter 4, to have a waveguide grating that is wavelength tunable, we propose to implement a tunable waveguide grating by incorporating a PN junction across the waveguide grating, to use the free-carrier plasma dispersion effect in silicon to achieve wavelength tuning. The use of a pair of wavelength-tunable waveguide gratings to form a wavelength-tunable Fabry-Perot resonator for microwave photonic signal processing is studied. Thanks to its electrical tunability, a high-speed electro-optic modulator, a tunable fractional-order photonic temporal differentiator and a tunable optical delay line are experimentally demonstrated.

In Chapter 5, to increase the bandwidth of a waveguide grating, an LC-WBG is designed, fabricated and evaluated. By incorporating two LC-WBGs in two arms of an MZI structure, an on-chip optical spectral shaper is produced, which is used in a photonic microwave waveform generation system based on SS-WTT mapping for LCMW generation.

In Chapter 6, to enable the LC-WBG could be electrically tuned, a lateral PN junction is introduced in the grating and thus an electrically tunable LC-WBG is realized. By incorporating two tunable LC-WBGs in a Michelson interferometer structure, an electrically tunable optical spectral shaper is made. By applying the fabricated spectral shaper in an SS-WTT mapping system, a continuously tunable LCMW is experimentally generated.

In Chapter 7, a silicon-based on-chip symmetric MZI incorporating multiple cascaded MRRs is designed, fabricated and evaluated. By specifically designing the radii of the rings, the interferometer could be designed to have a spectral response with a largely increasing or decreasing FSR, and its use for the photonic generation of a chirped microwave waveform is experimentally demonstrated. By specifically designing the radii of the rings, the

interferometer could also be designed to have a multi-channel spectral response with identical channel spacing, and its use for the implementation of an independently tunable multi-channel fractional-order temporal differentiator is experimentally demonstrated.

In Chapter 8, to further reduce the footprint of an optical micro-cavity resonator, a silicon-based on-chip ultra-compact MDR with a single-mode operation and an ultra-high Q-factor is proposed, fabricated and evaluated. The key features of the fabricated MDR include ultra-compact footprint, single-mode operation, no resonance-splitting, and ultra-high Q-factor, which make the MDR have a high potential for microwave photonic applications. Its use for the implementation for a microwave photonic filter and an optical delay line is experimentally demonstrated.

In Chapter 9, to enable the MDR could be electrically tuned, by incorporating a lateral PN junction in the disk, a silicon-based on-chip electrically tunable MDR is proposed, fabricated and evaluated. The key features of the tunable MDR include ultra-compact footprint, single-mode operation, no resonance-splitting, and flexible electrical tunability. Thanks to its electrical tunability, the use of the fabricated MDR in microwave photonic applications such as a high-speed electro-optic modulator, a tunable photonic temporal differentiator and a tunable optical delay line is experimentally demonstrated.

Finally, a conclusion is drawn in Chapter 10 with recommendations for future work.

CHAPTER 2 THEORETICAL OVERVIEW

Among different microwave photonic applications, photonic generation of arbitrary microwave waveforms and photonic processing of microwave signals are two important topics. In this chapter, we present a theoretical overview of photonic arbitrary microwave waveform generation based on spectral-shaping and wavelength-to-time mapping, and introduce the theoretical principles of photonic temporal differentiator and microwave photonic delay line.

2.1 Photonic generation of arbitrary microwave waveform

Microwave waveforms with a large time-bandwidth product (TBWP) offer a great potential for applications in communication systems to increase data transmission rate and in modern radar systems to enhance the range resolution. In the past, microwave waveforms were generated in the electrical domain using digital electronics. However, the time jitter, the limited speed and the nonlinearity of currently available digital-to-analog converters (DACs) set a limitation on the sampling rate, which inhibits from generating a microwave waveform at a high frequency with a large TBWP. To circumvent the obstacle, photonic generation of microwave waveforms has been considered a potential solution, which brings the inherent advantages of broad bandwidth and low loss offered by photonics to the microwave systems. In the past few years, numerous approaches to the generation of microwave waveforms based on photonics have been proposed and demonstrated. Thanks to its flexibility and simplicity,

spectral-shaping and wavelength-to-time mapping has been considered one of the most important photonic-assisted solutions for arbitrary microwave waveform generation

2.1.1 Spectral shaping and wavelength-to-time mapping

The fundamental principle of spectral shaping and wavelength-to-time (SS-WTT) mapping technique is shown in Fig. 2.1. As can be seen, a typical SS-WTT mapping system consists of an ultrashort optical pulse source, an optical spectral shaper, a dispersive element, and a high-speed photodetector. An ultrashort optical pulse emitted from a pulse laser source is firstly spectrally shaped by an optical spectral shaper. Then, the spectrum-shaped optical pulse is sent to a dispersive element, which could be a length of dispersive fiber or a chirped fiber Bragg grating, to perform linear WTT mapping. At the output of a high-speed photodetector, a microwave waveform with the shape identical to that of the shaped optical spectrum is generated. As can be seen, in an SS-WTT mapping system the optical spectral shaper is the key device which is specifically designed to have a spectral response with a shape that is a scaled version of the microwave waveform to be generated. For example, in order to generate a linearly chirped microwave waveform, the spectral shaper needs to have a spectral response with a linearly increasing or decreasing free spectral range.

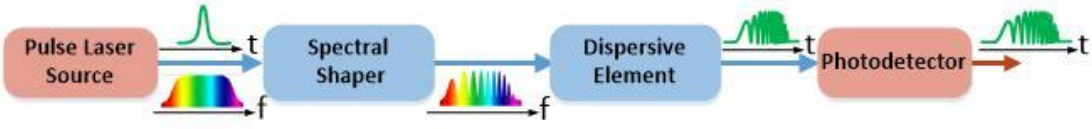

Fig. 2.1 Schematic of a microwave waveform generation system based on SS-WTT mapping

Mathematically, an ultrashort optical pulse is firstly spectrally shaped by an optical spectral shaper. At the output of the spectral shaper, the spectrally-shaped pulse is written as *g(t)* with

a temporal width Δt_0. Then, the spectrum-shaped optical pulse is sent to a dispersive element. If the dispersive element is a length of fiber with a dispersion value of $\ddot{\Phi}$, its transfer function could be described as:

$$h(t) = e^{j\frac{t^2}{2\ddot{\Phi}}} \tag{2-1}$$

At the output of the dispersive element, the optical pulse could be written as:

$$\begin{aligned} y(t) = g(t) * h(t) &= \int_{-\infty}^{+\infty} g(\tau)\cdot e^{j\frac{(t-\tau)^2}{2\ddot{\Phi}}} d\tau \\ &= \int_{-\infty}^{+\infty} g(\tau)\cdot e^{j\frac{t^2-2t\tau+\tau^2}{2\ddot{\Phi}}} d\tau \\ &= e^{j\frac{t^2}{2\ddot{\Phi}}} \int_{-\infty}^{+\infty} g(\tau)\cdot e^{j\frac{-2t\tau+\tau^2}{2\ddot{\Phi}}} d\tau \\ &= e^{j\frac{t^2}{2\ddot{\Phi}}} \int_{-\infty}^{+\infty} g(\tau)\cdot e^{j\frac{-t\tau}{\ddot{\Phi}}} \cdot e^{j\frac{\tau^2}{2\ddot{\Phi}}} d\tau \\ &\approx e^{j\frac{t^2}{2\ddot{\Phi}}} \int_{-\infty}^{+\infty} g(\tau)\cdot e^{j\frac{-t\tau}{\ddot{\Phi}}} d\tau \\ &= e^{j\frac{t^2}{2\ddot{\Phi}}} \cdot G(\omega)\Big|_{\omega=\frac{t}{\ddot{\Phi}}} \end{aligned} \tag{2-2}$$

where $G(\omega)$ is the Fourier transform of *g(t)*.

As can be seen, the optical signal envelope at the output of the dispersive element is proportional to the Fourier transform of the spectrally-shaped optical signal envelope when the temporal width of the input ultrashort pulse Δt_0 and the second-order dispersion $\ddot{\Phi}$ of the dispersive element satisfy the following condition:

$$\left|\frac{\Delta t_0^2}{2\ddot{\Phi}}\right| \ll 1 \tag{2-3}$$

which means the phase term $\frac{\tau^2}{2\ddot{\Phi}}$ in (2-2) satisfies $\frac{\tau^2}{2\ddot{\Phi}} \le \frac{\Delta t_0^2}{2\ddot{\Phi}} \ll 1$, thus we have $e^{j\frac{\tau^2}{2\ddot{\Phi}}} \approx 1$.

Thus, at the output of the high-speed photodetector, a microwave waveform in the electrical domain with the temporal waveform identical to the shaped optical spectrum is generated. The key advantage of the approach based on SS-WTT mapping is its large flexibility in tailing the shape of a waveform by controlling the optical spectral shaper, since the spectral response of the spectral shaper can be easily reconfigured.

2.1.2 Optical spectral shaper

An optical spectral shaper is a key device in a photonic arbitrary microwave waveform generation system based on SS-WTT mapping, since its spectral response determines the temporal profile of the generated microwave waveform. In general, for generation of a specific microwave waveform, the optical spectral shaper is designed to have a specific spectral response with a shape that is a scaled version of the microwave waveform required to be generated.

Linearly chirped microwave waveform (LCMW) is an important microwave waveform with a linearly varying instantaneous frequency in the time domain. An LCMW with a large TBWP is widely used in modern radar systems for the high resolution. In order to generate an LCMW at a high frequency with a wide bandwidth, it is highly preferred to use a photonic microwave waveform generation system based on SS-WTT mapping. For LCMW generation, the optical spectral shaper is required to have a spectral response with a linearly varying free spectral range (FSR). To implement such an optical spectral shaper, a typical

configuration is a Mach-Zehnder interferometer (MZI) structure incorporating a pair of linearly chirped fiber Bragg grating (LC-FBG) with different chirp rates.

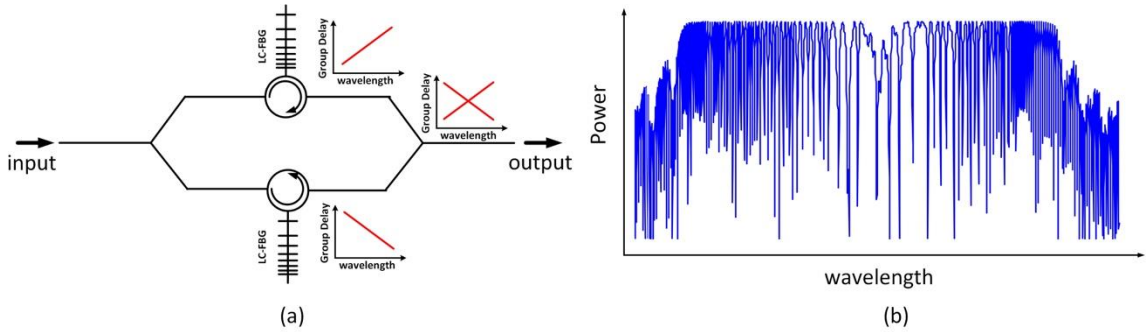

Fig. 2.2 (a) Schematic of an optical spectral shaper with a symmetric MZI configuration; and (b) simulated spectral response of the spectral shaper.

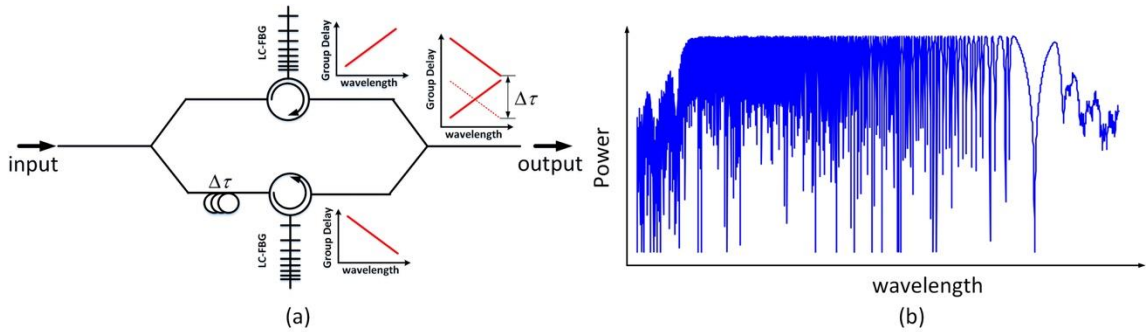

Fig. 2.3 (a) Schematic of an optical spectral shaper with an asymmetric MZI configuration; and (b) simulated spectral response of the spectral shaper.

Fig. 2.2(a) illustrates a schematic of an optical spectral shaper with a symmetric MZI configuration incorporating two LC-FBGs with opposite chirp rates. An input light wave is split by the first 3-dB coupler into two beams to travel through the LC-FBGs in the upper and lower arms of the MZI. Spectral components of the light waves with different wavelengths are reflected from different positions in the LC-FBGs. By the optical circulators

in the two arms, the reflected light waves are collected and recombined at the second 3-dB coupler at the output. As a result of the optical interference at the recombination, the optical spectral shaper with a wavelength-dependent FSR is achieved. Fig. 2.2(b) shows the simulated spectral response of the spectral shaper, which has a symmetrically linearly-varying FSR. Away from the center, the FSR is linearly increasing. The FSR of the optical spectral shaper is defined here as the wavelength separation between two adjacent spectral peaks. Thus, an optical spectral shaper with a linearly varying FSR is generated, which satisfies the requirement of a photonic microwave waveform generation based on the SS-WTT mapping technique for LCMW generation. In addition, to tune the center frequency of the generated LCMW, an optical delay line could be added in one arm of the spectral shaper to introduce a length difference between the two arms. Fig. 2.3(a) illustrates a schematic of an optical spectral shaper with an asymmetric MZI configuration. Thanks to the length difference between the two arms resulted by an offset length of the fiber, as shown in Fig. 2.3(b), the spectral response of the spectral shaper has a linearly decreasing FSR. By tune the length of the offset fiber, the central frequency of the generated LCMW could be tuned. By carefully designing the LC-FBGs and the length of the offset fiber, the spectral response of the spectral shaper is controlled to have a symmetrical, a uniformly increasing or decreasing FSR.

Mathematically, the spectral shaper incorporating a pair of LC-FBGs with the opposite chirp rates can be modeled as a two-tap delay-line filter. The transfer function of the spectral shaper is given by

$$T(\lambda)=\frac{1}{2}W(\lambda)\left[1+\cos\left(\frac{2\pi n_{eff}}{\lambda}2\Delta L\right)\right],\quad \left(\left|\lambda-\lambda_0\right|\le\frac{B_\lambda}{2}\right) \tag{2-3}$$

where $W(\lambda)$ is the intensity reflection spectrum of the LC-FBG, B_λ is the bandwidth of the spectral shaper where we assume that the input ultra-short pulse has a spectral width that is wider than the bandwidth of the spectral shaper, n_{eff} is the effective refractive index of the fiber, and ΔL is the length difference between the two arms of the MZI in the spectral shaper, which includes the wavelength-independent path difference ΔL_0 caused by the offset fiber (since the length of the offset waveguide is small, the dispersion can be ignored), and the wavelength-dependent length difference introduced by the chirp of the LC-FBG $\Delta L_1(\lambda)$. ΔL_0 can be controlled by selecting the length of the offset fiber, and $\Delta L_1(\lambda)$ is determined by the bandwidth and the chirp rate of the LC-FBG, which can be calculated using $\Delta L_1(\lambda) = \delta\lambda/C$, where $\delta\lambda$ (nm) is the wavelength detuning from the center wavelength λ_0, and C (nm/mm) is the chirp rate of the LC-FBG. Note that $\delta\lambda$ is positive when the reflection position is at shorter wavelength than λ_0, and $\delta\lambda$ is negative when the reflection position is at longer wavelength than λ_0. Then, the transfer function $T(\lambda)$ can be rewritten as

$$T(\lambda) = \frac{1}{2} W(\lambda) \left\{ 1 + \cos\left[\frac{2\pi n_{eff}}{\lambda} \left(2\Delta L_0 + 2 \cdot 2\Delta L_1 \right) \right] \right\} \tag{2-4}$$

where n_{eff} is the effective refractive index of the fiber. It is worth noting that since a pair of LC-FBGs with opposite chirp rates are incorporated in the two arms of the MZI, the wavelength-dependent length difference introduced by ΔL_1 is doubled, which also leads to the doubling in the chirp rate, and thus the TBWP of the generated microwave waveform.

The spectral response of the spectral shaper presents a varying FSR due to the chirp of the LC-FBGs. The FSR of the optical spectral shaper response is a function of wavelength and can be expressed as

$$FSR = \frac{\lambda^2}{2n_{eff}\Delta L} \cong \frac{\lambda_0^2}{2n_{eff}\left(\Delta L_0 + 2\frac{\delta\lambda}{C}\right)} \tag{2-5}$$

According to (2-5), by properly selecting the parameters of the LC-FBGs and controlling the length of the offset fiber, the FSR of the optical spectral shaper can be specifically controlled to be symmetrical, linearly increasing or decreasing, which is required for LCMW generation.

However, since the spectral shaper with an MZI configuration is realized using the discrete fiber-based components, the stability of the spectral shaper is very poor. To improve the stability, a dedicated packaging is needed, which would heavily increase the system cost. Therefore, integrated solutions are highly preferred for the implementation of such an optical spectral shaper.

2.2 Photonic processing of microwave signal

Photonic processing of microwave signals has also been a topic of interest and has been intensively investigated in the last few years. Compared with the conventional microwave signal processing techniques based on digital or analog electronic circuits, processing microwave signals in the optical domain by taking advantage of the low loss and large bandwidth offered by photonics provides a much higher speed, wider bandwidth and greater tuning range. Various techniques have been proposed and demonstrated. These signal processors include microwave filters, photonic temporal differentiators and integrators, Hilbert transformers, microwave mixers, and microwave phase shifters. Among various signal processors, photonic temporal differentiator is a basic signal processing block for advanced computing and information processing circuits. In addition, microwave photonic

delay line, capable of controlling the time delay of a microwave signal in the optical domain, is a basic and important element that can find applications in radar, communications, and signal processing. An introduction to the theoretical principles of photonic temporal differentiator and microwave photonic delay line is presented.

2.2.1 Photonic temporal differentiator

Photonic temporal differentiator, as one of the basic signal processing blocks, performs temporal differentiation of the complex envelope of an arbitrary optical signal. For example, an *Nth*-order (N = 1; 2; 3…) photonic temporal differentiator is a device that performs the *Nth*-time derivation on the complex envelope of an input arbitrary optical waveform. Fig. 2.4 shows a typical operation of an *Nth*-order photonic temporal differentiator. An input optical signal is launched into the temporal differentiator. At the output of the temporal differentiator, an optical signal with a complex temporal envelope proportional to the *Nth*-order temporal derivative of the input complex envelope is generated.

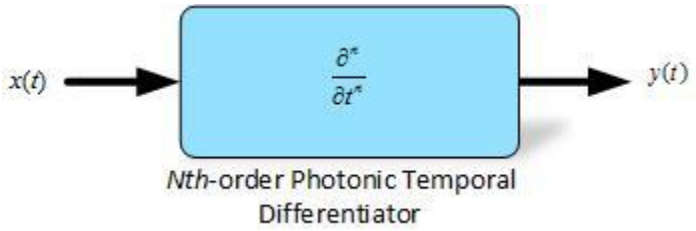

Fig. 2.4. Operation of a *Nth*-order photonic temporal differentiator

Mathematically, the *Nth*-order temporal differentiation performed by the differentiator on the input optical signal could be written as:

$$y(t) = \frac{\partial^n}{\partial t^n} x(t) \tag{2-6}$$

where *x(t)* is the input optical signal and *y(t)* is the output optical signal.

The relationship in (2-6) between the input and output temporal envelopes can be expressed in the frequency domain using the well-known Fourier transform:

$$\left[y(t) \right] = \mathcal{F}\left[\frac{\partial^n}{\partial t^n} x(t) \right]$$

$$Y(\omega) = (j\omega)^n \cdot X(\omega) \tag{2-7}$$

where $X(\omega)$ and $Y(\omega)$ are the Fourier transforms of the input and output signal, *x(t)* and *y(t)*, respectively.

As can be seen, a *Nth*-order photonic temporal differentiator can be realized using an optical device that has a transfer function given by $\left[j(\omega - \omega_0) \right]^n$, where n is the differentiation order, ω is the optical frequency and ω_0 is the optical carrier frequency. When the differentiation order n is equal to one, it is a first-order temporal differentiator. When the differentiation order n is not one, the processor is generalized to be a fractional-order photonic temporal differentiator, which could find applications in edge enhancement in the image processing. Note that for the implementation of a temporal differentiator, the phase response is more important than the magnitude response. The magnitude response of an ideal temporal differentiator may not be exactly satisfied, while the phase response plays a key role [116].

A simulation is made to study the impact of the differentiator magnitude response on the performance of the temporal differentiator in detail. An input Gaussian pulse with a temporal duration of 100 ps, corresponding to a 3-dB bandwidth of 8.8 GHz, is sent to a first-order temporal differentiator in the simulation. By changing the magnitude response of the differentiator, the impact of the magnitude response on the performance of the differentiator is studied. Fig. 2.5 (a) and (b) show the input Gaussian pulse waveform in the time and frequency domain, respectively. As can be seen, the pulse has a temporal duration of 100 ps and a 3-dB bandwidth of 8.8 GHz.

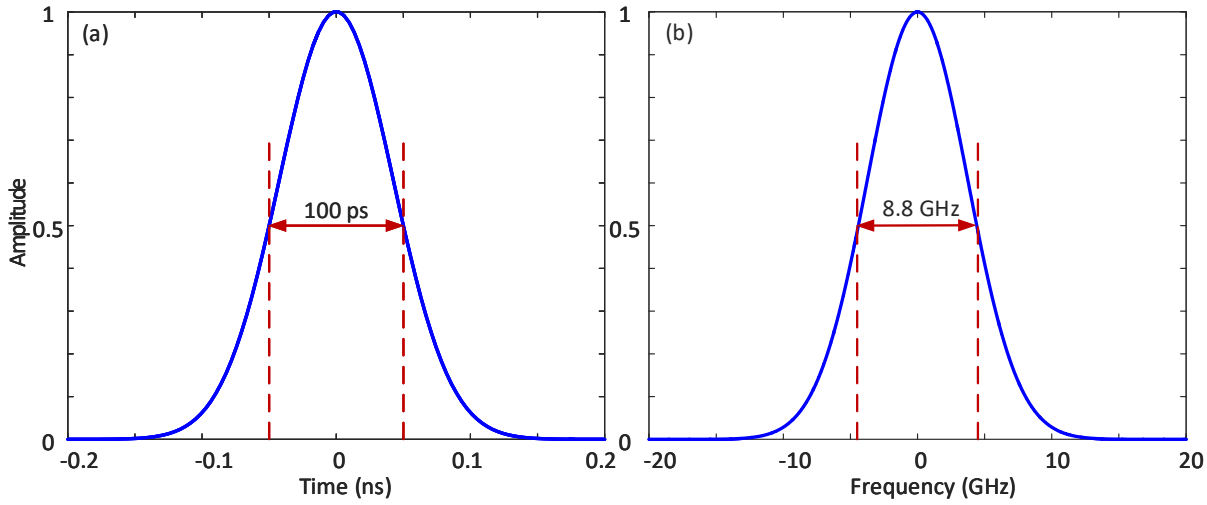

Fig. 2.5 (a) and (b) input Gaussian pulse waveform in the time and frequency domain.

Fig 2.6(a) and (b) show the theoretical first-order temporally differentiated Gaussian pulse in the time and frequency domain, respectively. Fig. 2.7(a) shows the different magnitude responses of the differentiator. The blue line gives the magnitude response of the ideal first-order differentiator in theory, and the purple line gives the magnitude response with a sinusoidal shape, which represents the case of using an Mach-Zehnder interferometer to perform the first-order differentiator. Fig. 2.7(b) shows the simulation results of the first-

order temporally differentiated Gaussian pulse when the different magnitude response of the differentiator is used. As can be seen, the simulation results overlap completely, which verifies that the magnitude response of the differentiator is not an important role in the temporal differentiation operation.

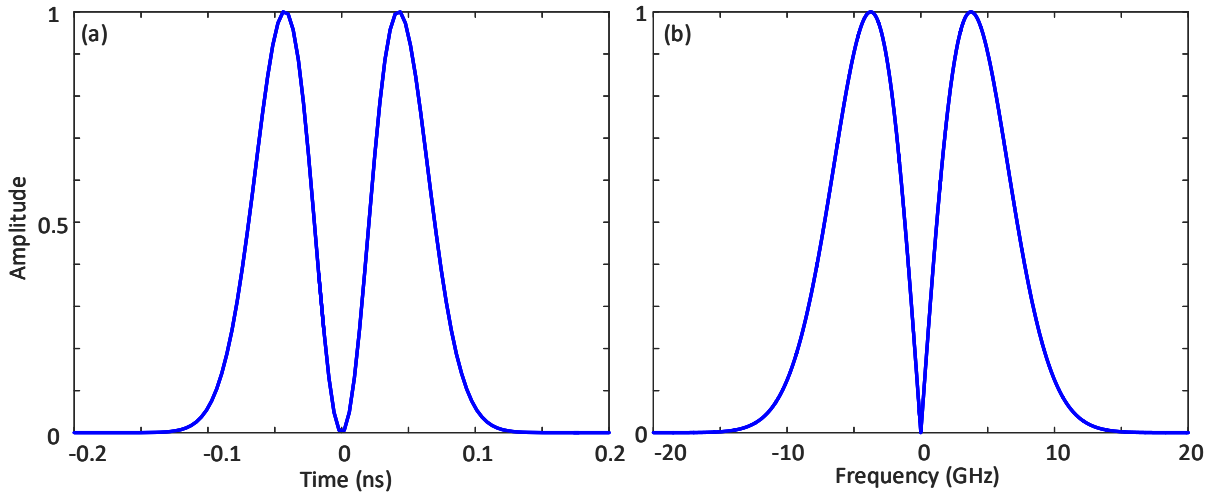

Fig. 2.6 (a) and (b) theoretical first-order temporally differentiated Gaussian pulse in the time and frequency domain.

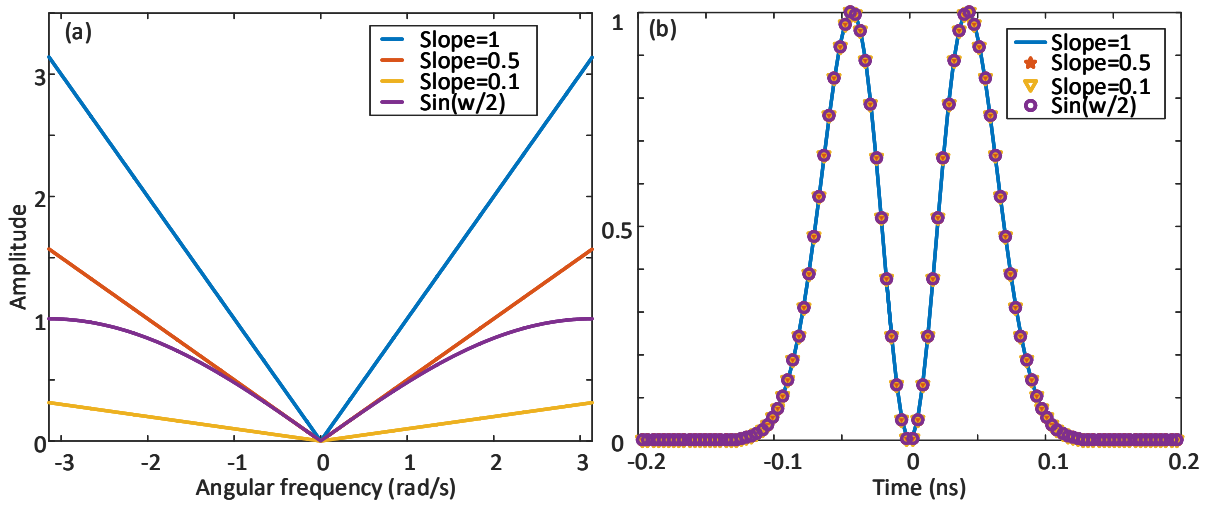

Fig. 2.7(a) Different magnitude responses of the differentiator and (b) simulation results of first-order temporally differentiated Gaussian pulse when the different magnitude response of the differentiator is used

Therefore, the magnitude response of the differentiator is not an important role in the temporal differentiation operation. So far, different schemes to implement a photonic temporal differentiator have been proposed and demonstrated, mainly based on fiber-optics. To reduce the size and enhance the stability, integrated solutions are highly needed.

2.2.2 Optical delay line

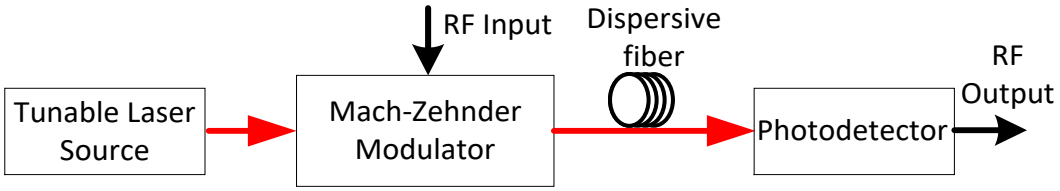

Fig. 2.8 Tunable microwave photonic delay line structure by using an optical delay line of a length dispersive fiber.

Microwave delay line, capable of controlling the time delay of a microwave signal, is a basic and important element that can find applications in radar, communications, and signal processing. The conventional delay lines implemented in the electrical domain can have time delays from a few nanoseconds to several microseconds. However, the narrow bandwidth and small tunability is the main disadvantage of the electrical delay line. To overcome this problem, a solution is to use photonics for the implementation of a microwave delay line. Fig. 2.8 shows a typical tunable microwave photonic delay line using an optical delay line of a dispersive fiber. As can be seen, a light wave emitted from a tunable laser source is sent to a Mach-Zehnder modulator (MZM), where an electrical radio-frequency (RF) signal is modulated on the light wave. Then, the modulated light wave is sent to an optical delay line, which could be a length of single-mode fiber or a dispersion compensating fiber (DCF). At

the output of the fiber, the modulated light wave is converted to the RF signal by a photodetector, and the time delay of the light wave experienced in the dispersive fiber could be transfer to the time delay of the RF signal. Thanks to the chromatic dispersion in the fiber, the modulated light wave with different carrier wavelengths would experience different time delays when traveling through the dispersive fiber. By tuning the wavelength of the input light wave, the achieved time delay of the RF signal could be tuned. Assuming the time delay at a reference wavelength λ_0 is t_0, the time delay at a different wavelength with a wavelength $\lambda_0 + \Delta\lambda$ in a dispersive fiber with a length of L and a dispersion parameter of D can be expressed as:

$$\tau = \tau_0 + L \cdot D \cdot \Delta\lambda \tag{2-8}$$

It can be seen in (2-8) that the tunability in this delay line can be achieved by changing the carrier wavelength or the length of the fiber, or the dispersion of the fiber. When using the photonics in the implementation of a microwave delay line, a broad bandwidth and flexible tunability is offered.

An optical delay line is a key component in the implementation of a microwave photonic delay line. It is highly preferred if the optical delay line could be tuned. Thus, a laser diode could be used to replace the tunable laser source, which would significantly reduce the overall system cost. Therefore, a tunable optical delay line is highly required. Different approaches have been proposed and demonstrated. For example, mechanically or thermally tunable LC-FBGs have been used as a tunable optical delay line. However, the sensitivity of the fiber-based optics to environmental variations leads to a poor stability of the system. To

have a better stability, integrated solutions are highly preferred for the implementation of a tunable optical delay line.

CHAPTER 3 SILICON-BASED ON-CHIP PHASE-SHIFTED WAVEGUIDE BRAGG GRATING

A waveguide Bragg grating is a fundamental silicon photonic device, which is widely used as an optical spectral filter typically reflecting light in a specific band of wavelengths and transmitting light in all other wavelengths. In particular, a phase-shifted waveguide Bragg grating (PS-WBG), thanks to its ultra-narrow transmission window in its stopband, is a key photonic component, which can find considerable applications in narrowband filtering, optical sensing and optical signal processing. In this chapter, we propose a silicon-based on-chip PS-WBG fabricated on a single-mode ridge waveguide and study the use of the fabricated PS-WBG for the implementation of a first-order photonic temporal differentiator.

3.1 Phase-shifted waveguide Bragg grating

Waveguide Bragg gratings are expected to play a significant role in future silicon-based optical communications and sensing systems [16]. Compared with a uniform Bragg grating, a phase-shifted waveguide Bragg grating (PS-WBG) with an ultra-narrow transmission band can find applications such as in narrowband filtering [29], optical sensing [117] and optical signal processing [31]. For example, the phase jump at the resonant frequency of a PS-WBG makes it possible for the implementation of a photonic temporal differentiator, a fundamental building block for optical signal processing. The method of using electron-beam lithography and reactive ion etching has been demonstrated in the fabrication of a PS-WBG on a silicon-on-insulator (SOI) platform [118], but its high fabrication cost prevents it from commercial

applications. Another method is to use deep ultraviolet (DUV) lithography [119], which brings advantages such as high throughput and low cost. In [19], a uniform Bragg grating was realized by corrugating the sidewalls of the waveguide, either on the ridge or the slab. In [22], a narrow-band transmission filter based on a PS-WBG in a silicon waveguide was demonstrated, in which the grating was corrugated on the sidewalls of the strip waveguide. In a strip waveguide, the high refractive index contrast between the core (silicon, n = 3.42 at 1550 nm) and the cladding (silicon dioxide or air, n = 1.52 or 1.00 at 1550 nm) makes the light strongly confined in the waveguide core. Due to the small cross section of the strip waveguide, the vertical sidewalls of the waveguide would heavily affect the field distribution of the confined light mode. The advantage of such a waveguide configuration is that a small periodic perturbation on the sidewalls can cause a considerably large grating coupling coefficient, which makes it possible to obtain a strong grating. However, the main disadvantage of the strip waveguide includes a high propagation loss because of Rayleigh scattering resulted from the sidewall roughness [120] and a large difficulty in achieving a fine-tuning of the coupling coefficient in the gratings. In contrast, a ridge waveguide typically has a much larger cross section, which would mitigate the impact of the sidewall roughness on the confined light, and thus has a high potential in producing a PS-WBG with a lower propagation loss and a higher fabrication tolerance.

3.1.1 Design of a PS-WBG

To make a PS-WBG have a lower propagation loss and a higher fabrication tolerance, we report a PS-WBG fabricated on a single-mode ridge waveguide. The design of a PS-WBG is performed firstly. Fig. 3.1(a) illustrates the cross section of the ridge waveguide on which a grating is fabricated. There is a top silicon layer of 220 nm in thickness and a bottom silica

layer of 2 μm in thickness. The shallow-etched ridge width is 500 nm and the etch depth is 130 nm. The slab width is 1000 nm. The waveguide with the described dimensions supports a single transverse-electric (TE) mode propagation.

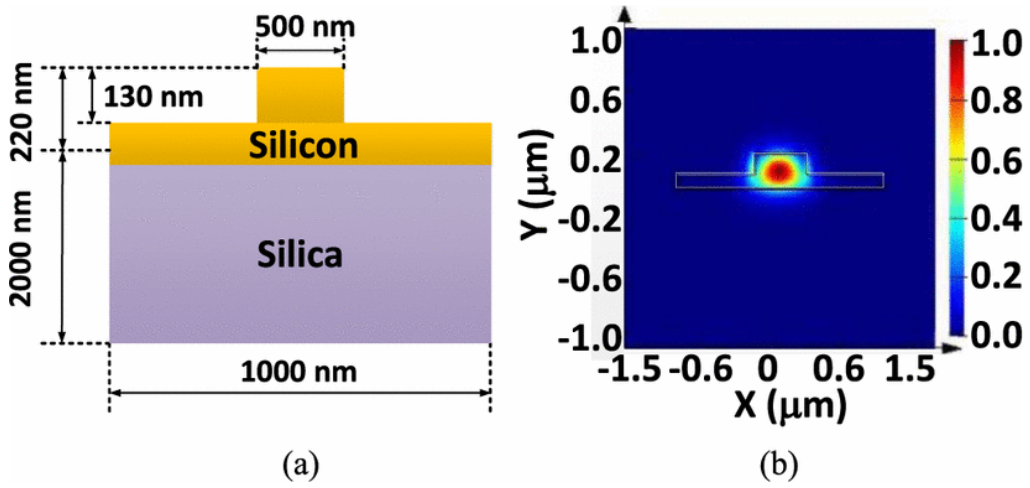

Fig. 3.1 (a) Schematic diagram of the cross section of the ridge waveguide; (b) simulated fundamental TE mode profile in the ridge waveguide.

A two-dimension simulation method [121] is applied to evaluate the optical mode distributions in the ridge waveguide. Fig. 3.1(b) shows the calculated mode profile of the fundamental TE mode in the ridge waveguide at 1550 nm. As shown in Fig. 3.1(b), most of the light is confined in the ridge and the distribution of the optical field around the sidewalls is very low, for both the ridge and slab sidewalls. Thanks to this low distribution, the propagation loss is reduced compared to a strip waveguide, since the propagation loss in a silicon waveguide mainly arises from the light scattering due to the sidewall roughness [122]. By creating periodic corrugations in the sidewall of the ridge, a grating is achieved.

Fig. 3.2 shows the perspective of the proposed PS-WBG. As can be seen, the grating is realized by introducing periodic sidewall corrugations in the ridge. The grating period Λ is

designed to be 320 nm, with a duty cycle of 60%, and the total length of the gratings is 1920 μm. A phase-shifted block, with a length of 160 nm corresponding to half of the grating period to introduce a π phase shift, is allocated at the center of the grating. Note that in the mask design, the shape of the corrugations is perfectly squared; however, the corrugations in a real fabricated grating are severely rounded due to the limited fabrication resolution. Therefore, a larger corrugation depth is used in the mask design to obtain a coupling coefficient that is identical to that of the designed grating.

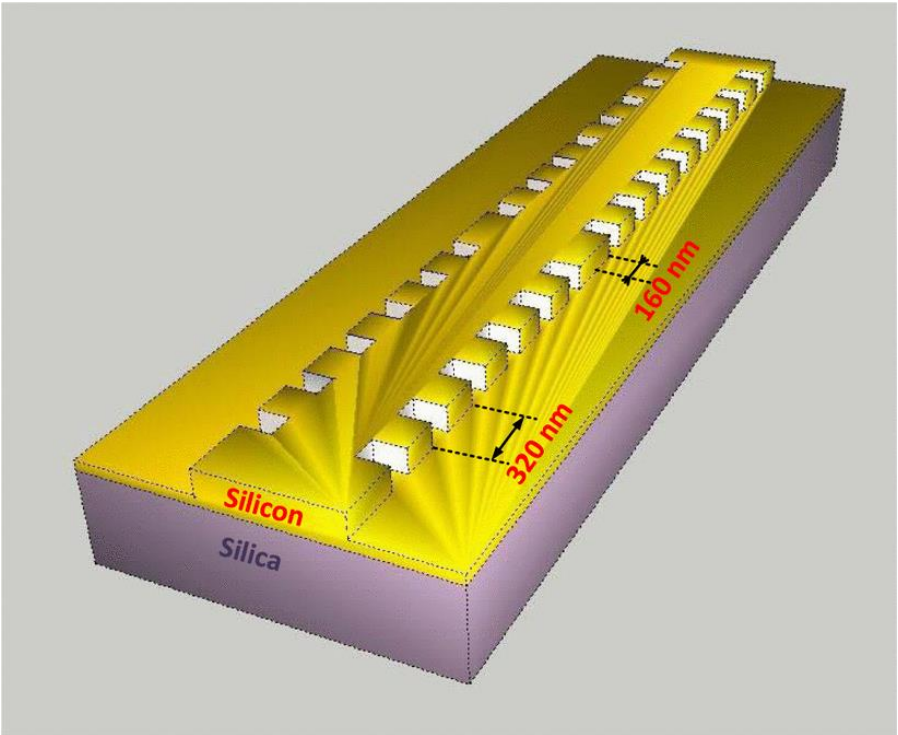

Fig. 3.2 Perspective view of the proposed PS-WBG in the ridge waveguide.

Fig. 3.3(a) shows the schematic layout of the proposed PS-WBG. At the two ends of the grating there are two integrated waveguide-to-fiber grating couplers, which are used to couple the light wave into and out of the chip. To minimize the chip footprint and reduce the

bending loss, a strip waveguide is incorporated in the design to guide the light wave from the input grating coupler to the PS-WBG and from the PS-WBG to the output grating coupler. Due to the different waveguide structure of the strip waveguide from the ridge waveguide on which the gratings are fabricated, a double-layer linear taper waveguide of a length of 50 μm is needed to achieve the mode transition between the strip and the ridge waveguides.

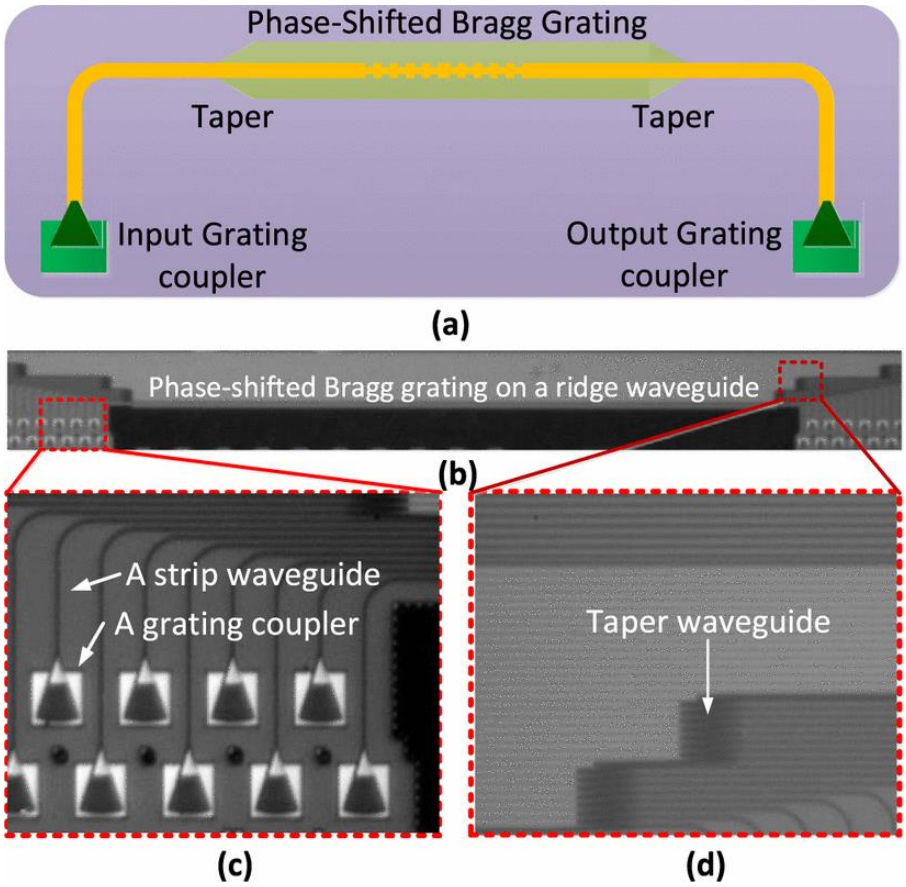

Fig. 3.3 (a) Schematic layout of the proposed PS-WBG; (b) image of the fabricated PS-WBG captured by a microscope camera; (c) image of the grating couplers and the strip waveguides; (d) image of a taper waveguide for the mode transition between a strip waveguide and a ridge waveguide.

Then, the designed grating is sent for fabrication using a standard CMOS compatible process with 248-nm deep ultraviolet lithography. Fig. 3.3(b) shows the image of the fabricated PS-

WBG captured by a microscope camera. Fig. 3.3(c) shows the zoom-in view of the grating couplers and the strip waveguides, and Fig. 3.3(d) shows the zoom-in view of the taper waveguides for the mode transition between the strip and ridge waveguide.

3.1.2 Evaluation of a PS-WBG

The optical performance of the fabricated PS-WBG is performed. The spectral response of the fabricated grating is measured using an optical vector analyzer (LUNA OVA CTe). Fig. 3.4(a) shows the measured reflection (blue line) and transmission spectrum (red line) of the fabricated PS-WBG, of which the corrugation depth is 125 nm in the mask design. It can be seen there is a resonant transmission window within the stop band in the transmission spectrum. The measured Bragg wavelength is at around 1557 nm, which is shorter than the theoretical value of 1580 nm in the design. The blue shift of the Bragg wavelength is caused by the fact that the fabricated waveguide has a lower effective refractive index than the designed waveguide due to the fabrication imperfections. To ensure the grating to work at the designed Bragg wavelengths, the fabrication imperfections should be taken into consideration in the selection of the grating period. Note that a grating on a ridge waveguide is usually has a smaller transmission bandwidth than a grating on a strip waveguide if all design parameters are controlled identical. However, in our design, in order to implement a photonic temporal differentiator with a wide bandwidth, the grating is deliberately designed to have a wide reflection notch by increasing the depth of the corrugations. As shown in Fig. 4.4(b), the width of the reflection notch (top-to-top width) of the fabricated PS-WBG is approximately 0.3 nm (or 37.5 GHz). The phase response is also shown in Fig. 4.4(b). It is clearly seen that a phase jump of π at the Bragg wavelength is produced. Thanks to this phase jump, the fabricated PS-WBG with such a spectral response can be used for the

implementation of a first-order photonic temporal differentiator with an operation bandwidth of 37.5 GHz.

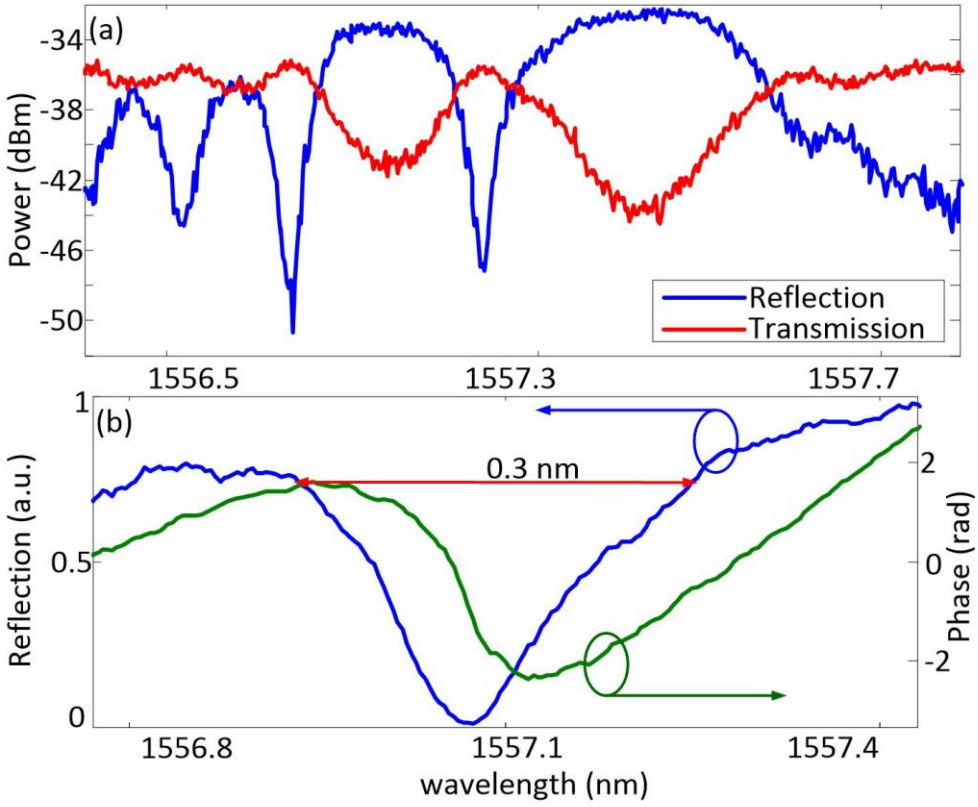

Fig. 3.4 (a) Measured reflection and transmission spectral responses of the fabricated PS-WBG with a designed corrugation depth of 125 nm; (b) zoom-in view of the reflection notch and its phase response.

3.2 Its application in photonic temporal differentiation

Different schemes have been proposed recently for the implementation of photonic temporal differentiators. For example, a photonic temporal differentiator can be implemented using a phase-shifted fiber Bragg grating [31] or a silicon microring resonator [123, 124]. A temporal differentiator based on a phase-shifted fiber Bragg grating is relatively easy to

implement, but its high sensitivity to environmental changes makes it unusable for practical applications or complicated packaging is needed to increase its stability. A silicon-microring-resonator-based temporal differentiator has the advantage of small footprint. However, the high thermo-optic coefficient of silicon (1.86×10^{-4} K^{-1}) and the high wavelength selectivity make the resonators susceptible to fluctuations in temperature [125]. In addition, optical coupling to the ring resonator is achieved by directional couplers. Controlling the coupling is crucial and requires an elaborate design in the coupling structure. Recently, a temporal differentiator using a silicon-based Mach-Zehnder Interferometer (MZI) was experimentally demonstrated [126]. Compared with an integrated grating, the structure based on an MZI is bulky, and the splitting ratios of the Y-branches must be precisely controlled, which would increase the fabrication tolerances.

To ease the design and have a high fabrication tolerance of the silicon-based device acting as a photonic temporal differentiator, we propose to use a PS-WBG fabricated on a single-mode ridge waveguide for the implementation of a photonic temporal differentiator. A first-order temporal differentiator provides the first-order temporal derivative of the complex envelope of an input optical signal. A temporal differentiator can be considered as a linear time-invariant (LTI) system with a frequency response given by

$$H(\omega) = j(\omega - \omega_0) = \begin{cases} |\omega - \omega_0| e^{j\frac{\pi}{2}}, & \omega > \omega_0 \\ |\omega - \omega_0| e^{-j\frac{\pi}{2}}, & \omega < \omega_0 \end{cases} \tag{3-1}$$

where ω is the optical angular frequency and ω_0 is the angular frequency of the optical carrier.

As can be seen from (3-1), a first-order photonic temporal differentiator can be implemented using an optical filter that has a magnitude response of $|\omega - \omega_0|$ and a phase response of $\frac{\pi}{2}$ for $\omega > \omega_0$ and $-\frac{\pi}{2}$ for $\omega < \omega_0$ corresponding to a phase jump of π at ω_0. The frequency response of the PS-WBG at the reflection notch is close to that of the optical filter given by (3-1), thus a first-order photonic temporal differentiator can be implemented using the fabricated PS-WBG.

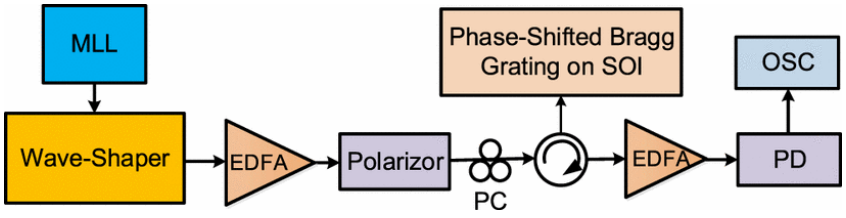

Fig. 3.5 Experimental setup. MML: mode lock laser. EDFA: erbium-doped fiber amplifier. PC: polarization controller. PD: photodetector. OSC: oscilloscope.

To verify the effectiveness of using the fabricated PS-WBG for the implementation of a first-order photonic temporal differentiator, an experiment is performed. Fig. 3.5 shows the experimental setup. A mode-locked laser (MLL) is used to generate a short Gaussian pulse with a temporal full-width at half-maximum (FWHM) of 550 fs, centered at 1558.5 nm. A WaveShaper (Finisar 4000S) is connected after the MLL to extend the temporal FWHM of the Gaussian pulse to 24 ps (corresponding to a spectral width of 37.5 GHz) centered at 1557.05 nm. An erbium-doped fiber amplifier (EDFA) connected at the output of the WaveShaper is used to compensate for the insertion losses of the system. A polarizer (POL) is used to make the light wave from the EDFA linearly polarized, and a polarization controller (PC) connected to the POL is used to control the polarization state of the input

light to the PS-WBG. Two lensed fibers are used, one is to couple the light into the chip and the other is to collect the transmitted light from the chip. A second EDFA is employed to amplify the reflected light wave. The temporally differentiated signal is detected by a photodetector (PD, New Focus, 45 GHz bandwidth) and its waveform is observed by a real-time oscilloscope (OSC, Agilent DSO-X93204A).

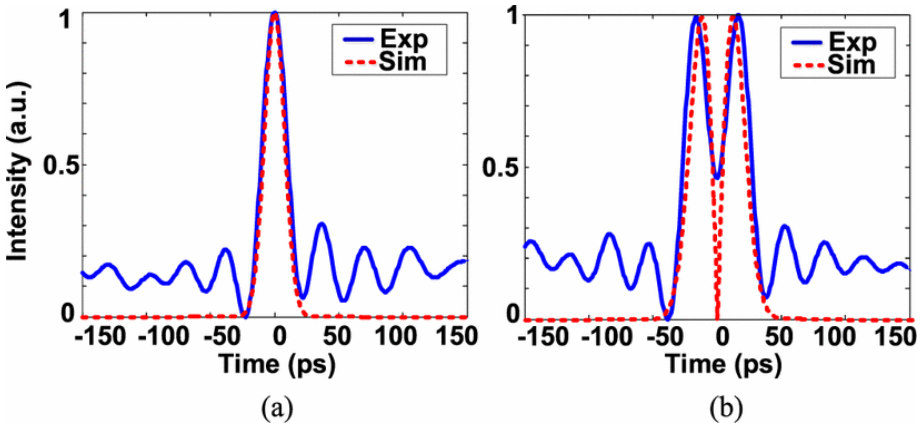

Fig. 3.6 (a) An input Gaussian pulse with an FWHM of 25 ps, and (b) the temporally differentiated pulses by simulation and experiment.

Fig. 3.6(a) shows the Gaussian pulse (blue-solid line) at the output of the WaveShaper. A simulated Gaussian pulse (red-dashed line) is also shown for comparison. The ripples observed at the tails of the measured Gaussian pulse are resulted from the OSC due to the limited sampling rate. Fig. 3.6(b) shows the corresponding temporally differentiated pulse (blue-solid line). Again, a simulated temporally differentiated pulse (red-dashed line) is also shown for comparison. As can be seen the experimentally generated pulse is close to the simulated pulse, which confirms the effectiveness of the use of the PS-WBG to perform a first-order temporal differentiator. Some ripples are observed in the experimentally generated pulse, which are again resulted from the OSC due to the limited sampling rate. We also note

that the dip in the center of the experimentally differentiated pulse is not as deep as the simulated pulse, which is mainly caused by the limited bandwidth of the PD (45 GHz). To study the impact of the bandwidth limitation of the photodetector on the performance of the differentiator, a simulation is done. An input Gaussian pulse with a temporal duration of 100 ps, corresponding to a 3-dB bandwidth of 8.8 GHz, is used in the simulation. By using a Butterworth filter with a different bandwidth before the photodetector, the impact of the bandwidth limitation of the photodetector on the performance of the differentiator could be studied.

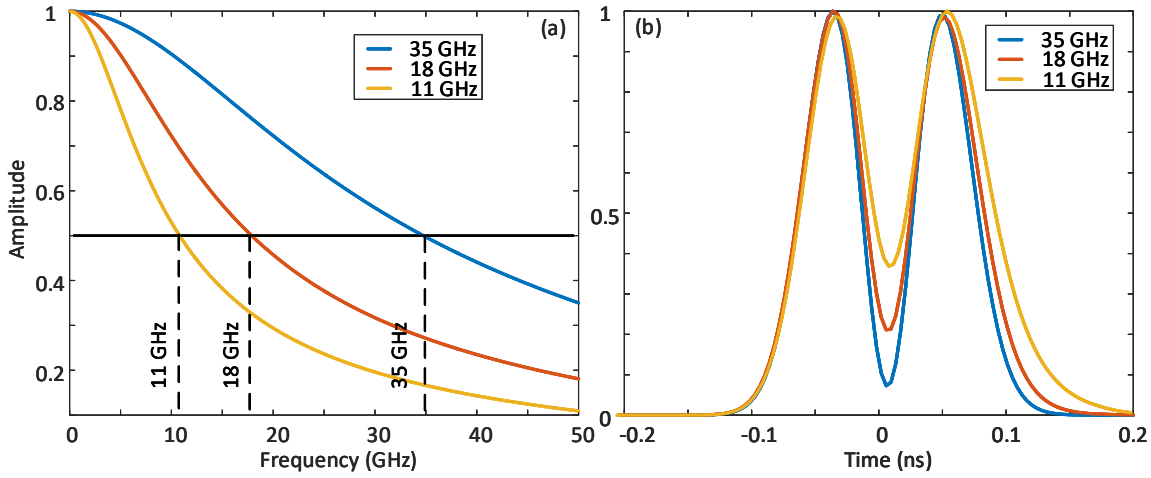

Fig. 3.7 (a) Different frequency responses of the Butterworth filter and (b) simulation results of the first-order temporally differentiated Gaussian pulse when the filter with a different bandwidth is used before the photodetector

Fig. 3.7(a) shows the frequency response of the Butterworth filter with a different bandwidth. The filter with the different bandwidth is applied on the first-order temporally differentiated Gaussian pulse in the simulation, which is equivalent to the impact of the PD bandwidth limitation imposed on the pulse. Fig. 3.7(b) shows the simulation results of the first-order

temporally differentiated Gaussian pulse when the filter with a different bandwidth is used before the photodetector. As can be seen, as the bandwidth of the filter is decreased from 35 to 18 and to 11 GHz, the notch center of the temporally differentiated Gaussian pulse gradually goes up, which could verify that the reason why the notch center of the differentiated Gaussian pulse does not reach zero is due to the bandwidth limitation of the photodetector.

3.3 Conclusion

In conclusion, a silicon-based on-chip PS-WBG was designed, fabricated and evaluated, and its use for the implementation of a first-order photonic temporal differentiator was experimentally demonstrated. The device was fabricated using a CMOS compatible process with 248-nm deep ultraviolet lithography. After fabrication, the optical performance of the fabricated PS-WBG was evaluated, which showed a reflection notch with a 3-dB bandwidth of approximately 0.3 nm. By using the fabricated PS-WBG as a first-order photonic temporal differentiator, an optical Gaussian pulse with a bandwidth of 37.5 GHz was temporally differentiated. The key advantage of using the PS-WBG to realize a photonic temporal differentiator includes flexible design and high fabrication tolerance. However, the main disadvantage is the fixed optical properties of the PS-WBG, which makes the differentiation order of the implemented temporal differentiator untunable once the PS-WBG is fabricated.

CHAPTER 4 Silicon-based on-chip electrically-tunable sidewall-Bragg-grating Fabry-Perot filter

To have a waveguide grating that is wavelength tunable, in this Chapter we propose to implement a tunable waveguide grating by incorporating a PN junction across the waveguide grating, to use the free-carrier plasma dispersion effect in silicon to achieve wavelength tuning. The use of a pair of wavelength-tunable waveguide gratings to form a wavelength-tunable Fabry-Perot resonator for microwave photonic signal processing is studied. Thanks to its electrical tunability, a high-speed electro-optic modulator, a tunable fractional-order photonic temporal differentiator and a tunable optical delay line are experimentally demonstrated.

4.1 Electrically tunable sidewall-Bragg-grating Fabry-Perot filter

Owing to the unique feature of a narrow transmission window within its stopband, a Bragg grating Fabry-Perot filter (BG-FPF) [127, 128] has been considered a key photonic component which can find numerous applications such as narrowband filtering, optical sensing, and optical signal processing. In addition, a BG-FPF with an ultra-narrow transmission window can also be used in a photonic sub-system for mode selection. For example, a BG-FPF can be incorporated in a laser cavity to ensure narrow linewidth operation [129]. In a high-capacity optical communications system where dense wavelength division multiplexed (DWDM) is employed, accurate channelization is needed, which can be implemented using an array of BG-FPFs with precisely controlled wavelength spacing [130]. However, the optical properties of a BG-FPF are predetermined by its design, which

are fixed once the device is fabricated. In addition, due to fabrication imperfections, there are always discrepancies in the optical properties of an actually fabricated BG-FPF. Therefore, the fixed optical properties and the unavoidable fabrication discrepancies may limit BG-FPFs for wide applications. Furthermore, for an adaptive sensor system and a reconfigurable optical communication network, a frequency-tunable transmission filter is always required [131]. A frequency-tunable BG-FPF is a candidate for such applications.

4.1.1 Design of an electrically tunable SBG-FPF

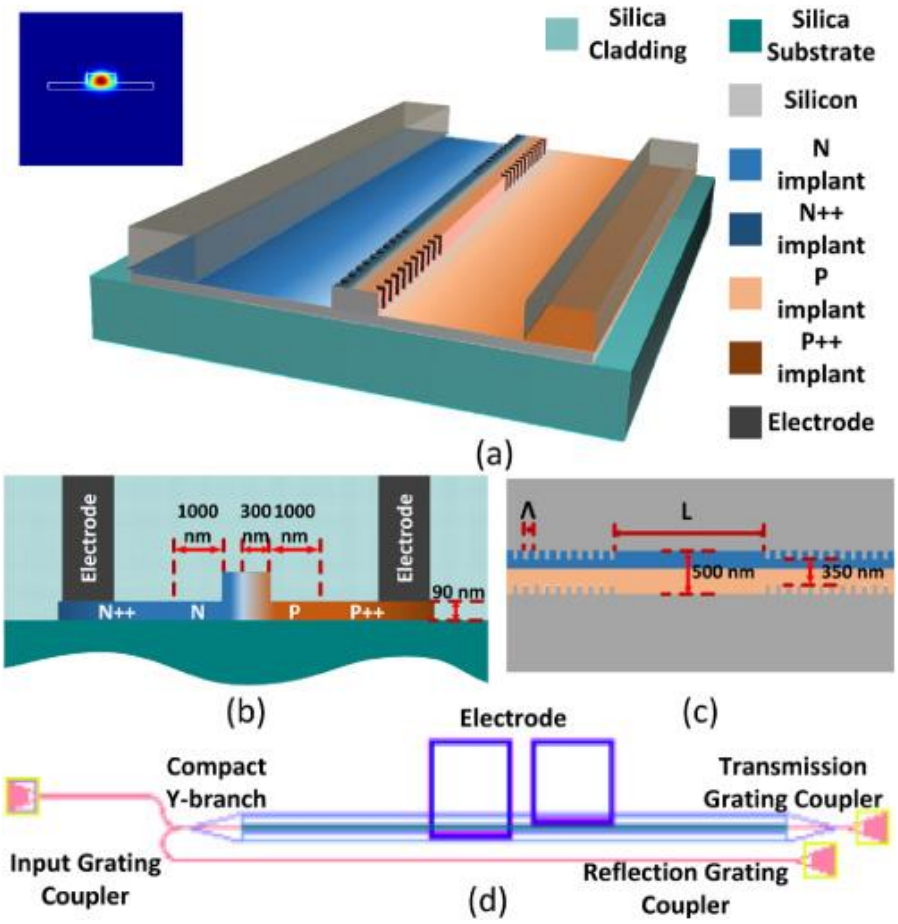

Fig. 4.1 (a) Perspective view of the proposed SBG-FPF. (Inset: Simulated fundamental TE mode profile of the rib waveguide); (b) cross-sectional view of proposed SBG-FPF; (c) top view of the FP cavity, and (d) schematic layout of the proposed SBG-FPF.

To achieve such an electrically tunable optical filter with an ultra-fast tuning speed, we propose a silicon-based on-chip electrically tunable sidewall-Bragg-grating Fabry-Perot filter (SBG-FPF). Fig. 4.1(a) illustrates the perspective view of the proposed SBG-FPF. It is fabricated on a Silicon-On-Insulator (SOI) substrate with a bottom silica layer of 2 μm in thickness and a top silicon layer of 220 nm in thickness. The cladding layer of silica is removed in Fig. 4.1(a) to clearly illustrate the internal structure of the device. The silicon rib waveguide with 500 nm in width, 220 nm in height, and 90 nm in slab thickness is employed to ensure a single fundamental TE mode operation. The inset in Fig. 4.1(a) shows a simulated mode profile of the fundamental TE mode at 1550 nm. To achieve a higher tuning efficiency, an asymmetrical lateral PN junction is adopted to enable electrical tuning of the grating based on the plasma dispersion effect. As shown in Fig. 4.1(b), the PN junction is slightly shifted to the left from the center of the waveguide by 50 nm, to increase the mode overlap with the p-type doping region, since the plasma dispersion effect is more sensitive to the change of the free-hole concentration. Additional p++ and n++ implantations, 1 μm away from the rib to minimize absorption losses, are utilized for ohmic contact formation. Fig. 4.1(c) provides the top view of the grating structure on the rib and the FP cavity. The periodic sidewall corrugations with a depth of 75 nm are introduced to the rib. The grating period Λ is 310 nm with a duty cycle of 50%, corresponding to a Bragg wavelength of 1550 nm. The total length of the grating is 1240 μm. The FP cavity, with a length L of 24.025 μm, is allocated at the center of the grating. Fig. 4.1(d) shows the schematic layout of the device. Three TE-mode grating couplers [132] are used to couple light between the chip and the input and output fibers, and a compact Y-branch [133] is used to collect the reflected light. To minimize the chip footprint and reduce the bending loss, a strip waveguide is used to guide the light signal

between the grating coupler and the filter. Since the filter is designed on a rib waveguide, a double-layer linear taper waveguide with a length of 50 μm, is used for the transition between the strip and the rib waveguides. Two contact windows are opened on the silica pads, with 2-μm-thick aluminum layer deposited to make the contacts. The entire device is 1.58 mm in length and 0.130 mm in width, giving a small footprint of 0.205 mm^2. The designed SBG-FPF is sent for fabrication using a standard CMOS compatible process with 248-nm deep ultraviolet lithography.

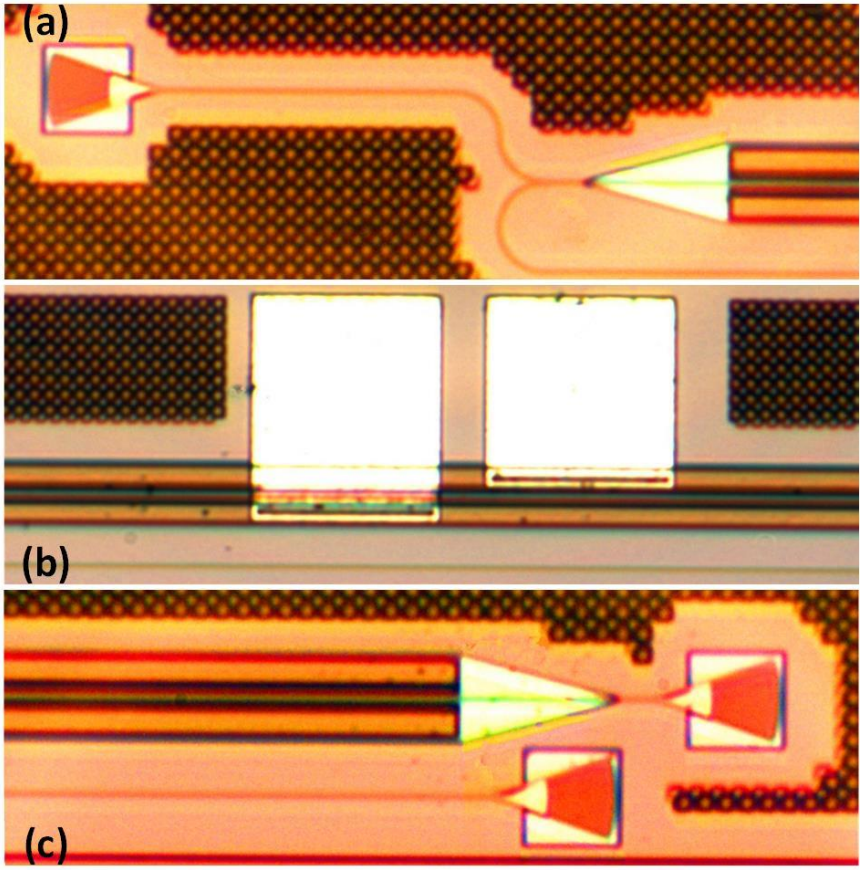

Fig. 4.2 (a) photograph of the input grating coupler; (b) photograph of the electrodes; and (c) photograph of the transmission and reflection grating coupers in the fabricated SBG-FPF.

Fig. 4.2(a) is a photograph of the input grating coupler in the fabricated SBG-FPF, captured by a microscope camera. At front end of the SBG-FPF, there is a taper waveguide to achieve the mode conversion and a compact-Y branch to split the reflected light signal to the reflection grating coupler. Fig. 4.2(b) is a photograph of the electrodes in the fabricated SBG-FPF. A bias voltage from a DC power supply is applied via an electrical probe to the PN junction to achieve spectral tuning. Fig. 4.2(c) is a photograph of the transmission and reflection grating couplers in the fabricated SBG-FPF. Again, there is a taper waveguide at the rear end of the SBG-FPF to achieve mode conversion.

4.1.2 Evaluation of an electrically tunable SBG-FPF

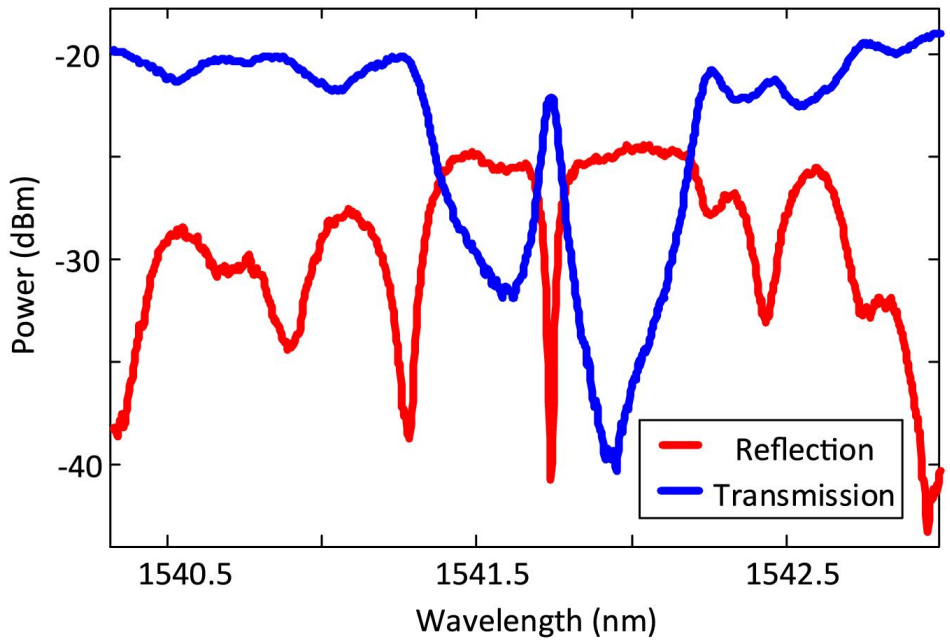

Fig. 4.3 Measured reflection and transmission spectra of the TBG-FPF with a zero bias voltage applied.

The optical performance of the SBG-FPF is first evaluated. To do so, we use an optical vector analyzer (LUNA OVA CTe) to measure the reflection and transmission spectra of the

fabricated SBG-FPF. Fig. 4.3 shows the spectra when a zero bias voltage is applied. It can be seen there is a resonant window within the stopband in the transmission spectrum. The notch in the reflection band has a 3-dB bandwidth of 46 pm with a Q-factor of 33,500, and an extinction ratio of 16.4 dB. The Bragg wavelength is shifted to 1541.75 nm due to the inevitable fabrication imperfections. Strong sidelobes in the reflection spectrum are seen, which can be suppressed by applying apodization to the grating. The insertion loss of the SBG-FPF is 19 dB, which consists of the fiber-to-fiber I/O coupling loss of 15.6 dB, the grating-induced loss of 2.1 dB and the loss due to the ion implantations of about 1.3 dB. Therefore, the optical excess propagation loss caused by ion implantation is 10.3 dB/cm. Note that the fiber-to-fiber I/O coupling loss is measured using a reference rib waveguide without a grating and without ion implantation. The grating-induced loss, which is mainly resulted from the sidewall scattering, is measured using a reference sidewall grating on a rib waveguide without ion implantation.

Then, the DC performance of the SBG-FPF is evaluated for the PN junction being forward biased. Fig. 4.4(a) shows the voltage-current (V-I) curve of the PN junction, which indicates that the junction is turned on at about -0.7 V. Fig. 4.4(b) shows the transmission spectrum, which is blue-shifted when the bias voltage is increased. Since the current is injected uniformly along the entire length of the device, the wavelengths of the stopband and the transmission window are both shifted to shorter wavelengths. The blue shifts are resulted from the decrease in the refractive index induced by the free-carrier injection. In addition, the injected free-carrier would also introduce an excess absorption loss, which would degrade the performance of the filter. To illustrate the performance degradation clearly, we show in detail the wavelength shift of the notch in the reflection band in Fig. 4.4(c). As can be seen

when the bias voltage is increasing, the Q-factor and the extinction ratio of the filter are reducing. For a current of 6.070 mA when operating at -1.0 V, the Q-factor is reduced to 25,700 and the extinction ratio is reduced to 5 dB. The blue shift of the notch wavelength is found to be 0.345 nm. The tuning of the spectral response when increasing the bias voltage is shown in Fig. 4.4(d). The wavelength shift rate is estimated to be -1.15 nm/V after the PN junction is turned on.

The DC performance of the SBG-FPF when the PN junction is reverse biased is also evaluated. As can be seen from Fig. 4.5(a), the PN junction reaches breakdown at approximately 16 V. Fig. 4.5(b) shows that the transmission spectrum is red-shifted when the bias voltage is increased. When reverse biased, if the voltage is increased, more carriers are extracted and the depletion region is widened. Thus, an increased effective refractive index would lead to a red-shifted spectrum. Fig. 4.5(c) shows the wavelength shift of the notch in reflection. When the bias voltage is increasing, the Q-factor is increasing due to the reduction in the free-carrier induced absorption loss. Meanwhile, the extinction ratio is also changed due to the change of the coupling condition. For an injection current of 53 nA when biased at 17.5 V, the Q-factor is increased to 44,000 and the extinction ratio is increased to 25 dB. The notch wavelength is red-shifted by 73.6 pm. The tuning of the spectral response is shown in Fig. 4.5(d). The wavelength shift rate is estimated to be 4.2 pm/V.

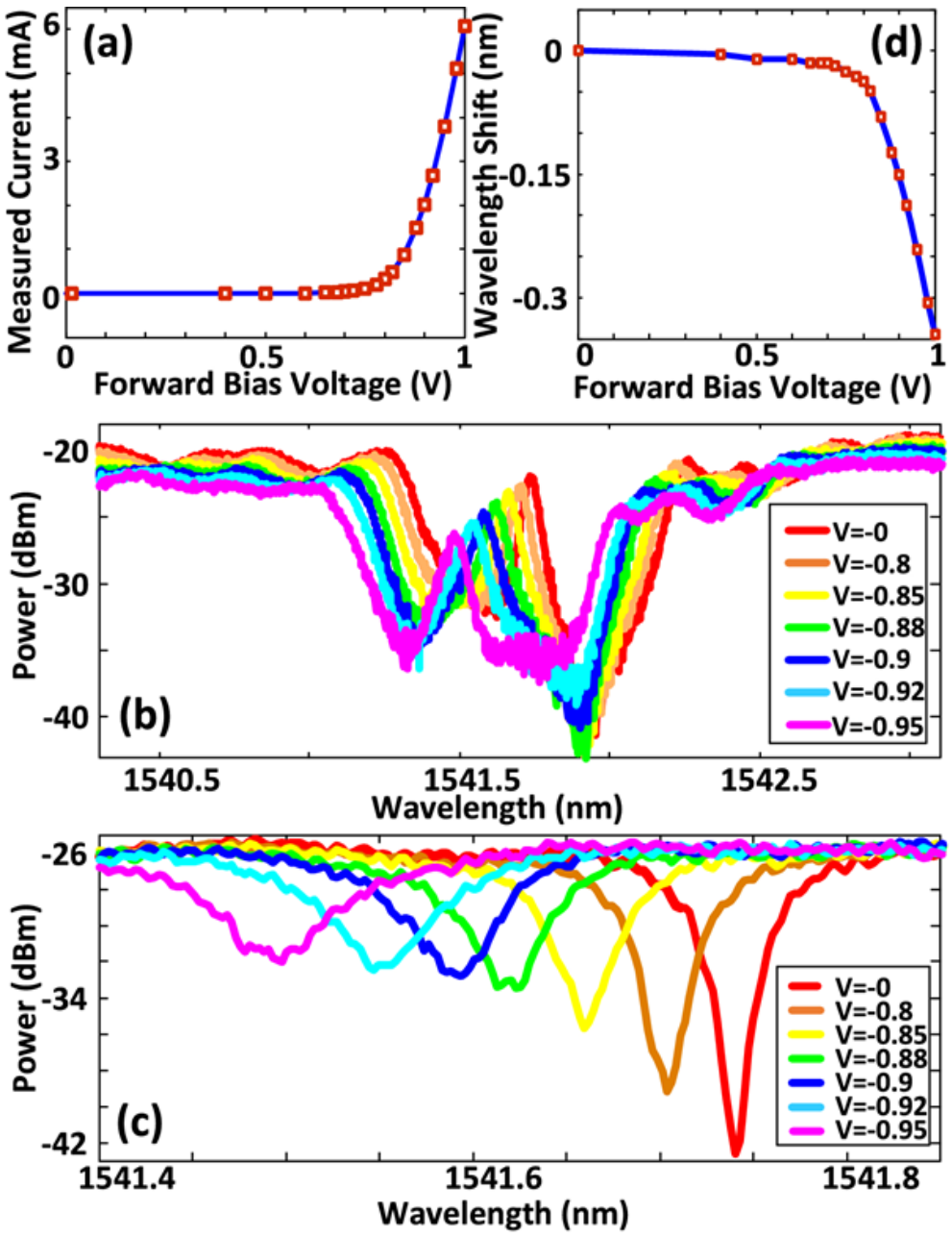

Fig. 4.4 (a) Measured V-I curves of the PN junction; (b) wavelength shift of the transmission spectrum; (c) notch wavelength shift when the PN junction is forward biased; and (d) wavelength shift when the bias voltage is increased.

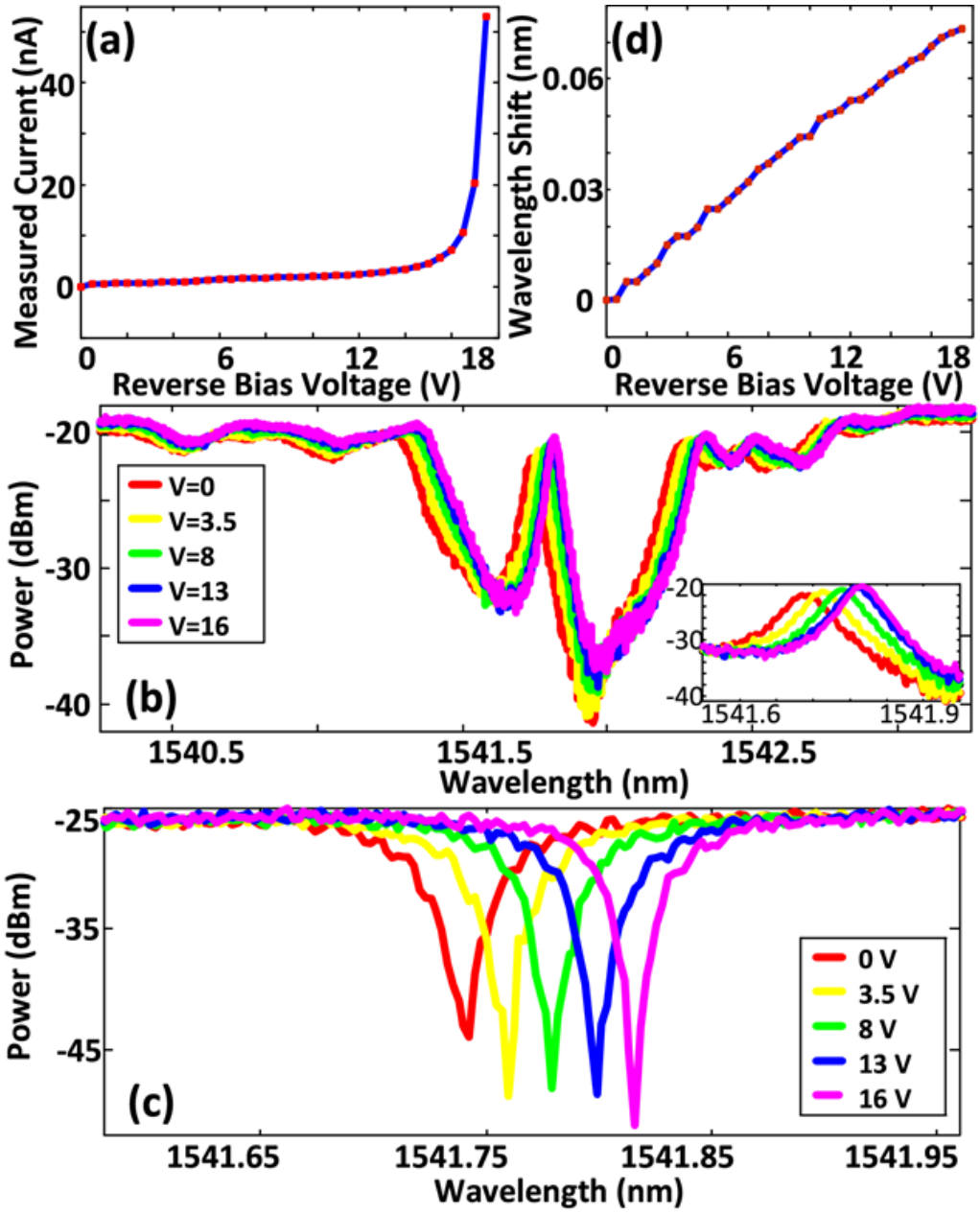

Fig. 4.5 (a) Measured V-I curves of the PN junction; (b) wavelength shift of the transmission spectrum (Inset: Zoom-in view of the wavelength shift of the transmission window); (c) notch wavelength shift when the PN junction is reverse biased, and (d) wavelength shift when the bias voltage is increasing.

4.2 Its application in microwave photonics

Thanks to its electrical tunability of the spectral response, the fabricated SBG-FPF could find microwave photonic applications such as a high-speed electro-optic modulator, a tunable fractional-order photonic temporal differentiator and a tunable optical delay line.

4.2.1 A high-speed electro-optic modulator

Since the light-confining resonating structure of the FP cavity can enhance the effect of refractive index change, we propose to use the electrically tunable SBG-FPF for the implementation of an electro-optic modulator. Similar to a silicon microring modulator [134], its 3-dB modulation bandwidth is determined by the *RC* time of the reverse-biased PN junction and the photon lifetime of the cavity. The photon lifetime is related to the Q-factor of the cavity given by $\tau = \lambda \cdot Q/2\pi c$, where c is the speed of light in vacuum. The value of the Q-factor indicates the light-confinement capability of the cavity. To evaluate the performance of the filter as an electro-optic modulator, the frequency response of the SBG-FPF is firstly measured for a given input optical wavelength. Fig. 4.6(a) and 6(b) shows the transmission window of the SBG-FPF when a reverse-bias voltage of 3.5 V and 8.0 V is applied, respectively, and three circles are used to indicate the different input wavelengths. Based on the estimated Q-factor, the photon-lifetime determined cut-off frequency is calculated to be 6.3 GHz based on $f_r = 1/2\pi\tau$. Fig. 4.6(c) shows the electro-optic frequency response for the three different input wavelengths. As can be seen, the maximum 3-dB modulation bandwidth is 5.6 GHz, which matches quite well with the calculated 3-dB bandwidth of 6.3 GHz. In addition, as can be observed, when the input wavelength is located at the peak of the transmission window, the frequency response, indicated in blue, has a 3-dB bandwidth of 1.5 GHz. When the input wavelength is away from the peak of the

transmission window, the 3-dB bandwidth is increased to 3.1 GHz, as indicated in red in Fig. 4.6(c). When the input wavelength is farther away from the peak of the transmission window, the 3-dB bandwidth is further increased to 5.6 GHz, as indicated in green. As the wavelength of the input light is away from the resonance wavelength, the corresponding confinement capability of the cavity for that wavelength is becoming weaker and its corresponding photon lifetime is becoming shorter. Therefore, the measured 3-dB modulation bandwidth is becoming larger. This photon-lifetime-dependent frequency response confirms that the modulation bandwidth of this SBG-FPF is mainly limited by the photon lifetime of the cavity. The same tendency of the electro-optic frequency response is found in Fig. 4.6(d), which shows the frequency response when the PN junction is reverse biased at 8.0 V.

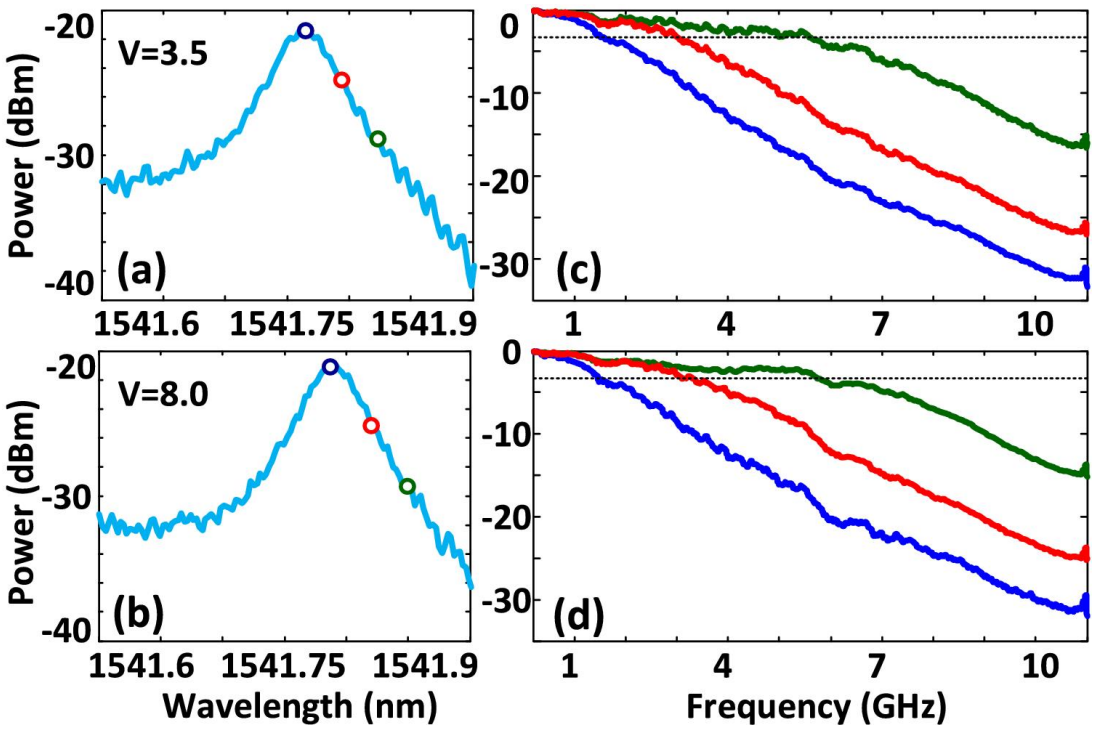

Fig. 4.6 Measured transmission window of the SBG-FPF when reverse biased with a voltage of (a) 3.5 V and (b) 8.0 V; (c) measured frequency responses for three different wavelengths when the reverse bias voltage is 3.5 V, and (d) when the reverse bias voltage is 8.0 V.

The performance of using the SBG-FPF as a modulator to achieve high-speed modulation is also evaluated. In the experiment, the SBG-FPF is driven by a 3.5-Gb/s 2^7-1 non-return-to-zero pseudorandom binary sequence with a Vpp of 1.8 V, generated by a pattern generator (Agilent N4901B). Eye diagram of the recovered electrical signal after photodetection is captured by a real-time oscilloscope (Infiniium 93204A), which is shown in Fig. 4.7. The eye diagram is quite open, which confirms that the SBG-FPF can be employed as a high-speed electro-optic modulator. Compared with a microring-based modulator, this filter has a higher fabrication tolerance and does not need a deliberately designed coupler. The performance of the filter as a modulator can also be further improved by optimizing the design of the FP cavity, the grating structure design and the PN junction design.

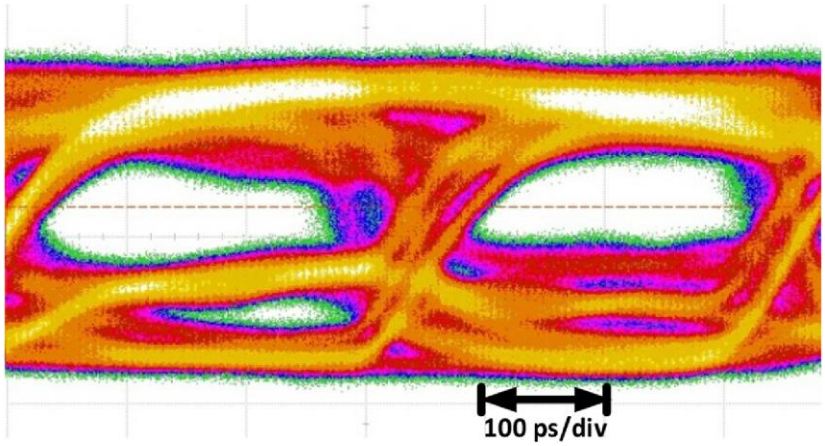

Fig. 4.7 Measured eye diagram for a non-return-to-zero pseudorandom binary sequence 2^7-1 at 3.5-Gb/s.

4.2.2 A tunable fractional-order photonic temporal differentiator

In chapter 3.3, a PS-WBG for the implementation of a first-order photonic temporal differentiator with a large operation bandwidth was demonstrated. However, the differentiation order of the temporal differentiator is always one, which is fixed and cannot

be tuned. Due to the potential applications in pulse shaping, signal processing and ultrafast optical signal coding, a photonic temporal differentiator with a tunable fractional order is highly preferred. Thanks to its tunable phase response of the reflection notch in the fabricated SBG-FPF, we propose to use the electrically tunable SBG-FPF for the implementation of a tunable fraction-order photonic temporal differentiator. For the implementation of a temporal differentiator, as demonstrated in [135], the magnitude response of an ideal temporal differentiator may not be exactly satisfied but the phase response plays a key role. Therefore, the electrically tunable SBG-FPF is a good candidate to realize a tunable fractional-order photonic temporal differentiator.

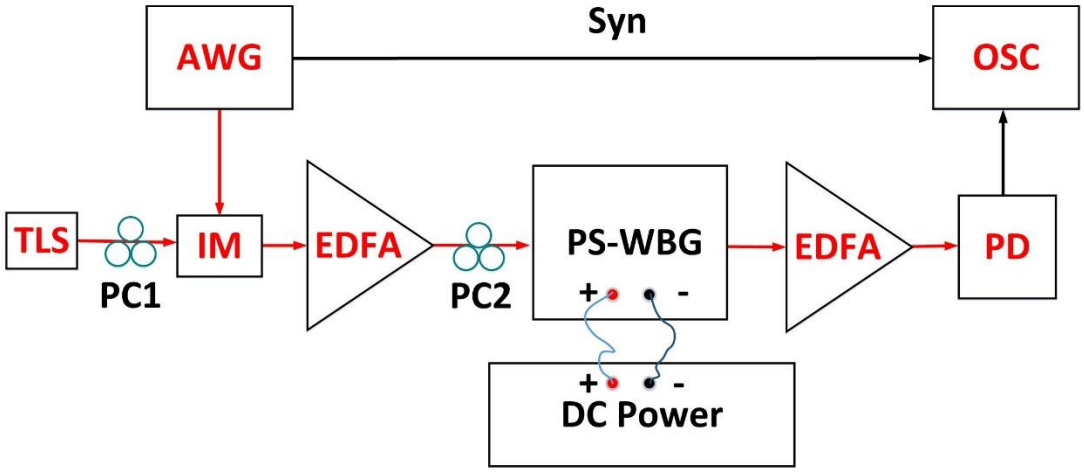

Fig. 4.8 Experimental setup. TLS: tunable laser source. IM: intensity modulator; AWG: arbitrary waveform generator. EDFA: erbium-doped fiber amplifier. PC: polarization controller. PD: photodetector. OSC: oscilloscope.

To verify that the fabricated SBG-FPF can be used to implement a temporal differentiator with a tunable differentiation order, an experiment is performed using the electrically tunable SBG-FPF with a notch in the reflection band of a linewidth as large as 90 pm. The

experimental setup is shown in Fig. 4. 8. A continuous-wave (CW) light wave from a tunable laser source (TLS) with the wavelength aligned at the notch center of the SBG-FPF is sent to an intensity modulator (IM) via a polarization controller (PC1). An electrical Gaussian pulse with a temporal full-width at half-maximum of about 110 ps, or a spectral width of about 10 GHz from an arbitrary waveform generator (AWG, Tektronix AWG7102) is applied to modulate the optical carrier at the IM. The modulated optical signal is then directed to the chip through a second polarization controller (PC2), which is used to adjust the state of polarization (SOP) of the input light wave to minimize the polarization-dependent loss. To compensate for the coupling loss, the optical signal is amplified at the input and output of the chip using two erbium-doped fiber amplifiers (EDFAs). Finally, the output optical signal is detected by a high-speed photodetector (PD) with the waveform observed by a high-speed sampling oscilloscope (OSC, Agilent 86116A). A DC voltage from a power source is applied via a probe to the PN junction. By changing the applied voltage, the phase response of the PS-WBG is changed. Thus, the differentiation order of the temporal differentiator is tuned. Note that as the bias voltage is tuned, the notch center also shifts, which requires that the carrier wavelength is also changed to re-align it to the notch center to enable an effective differentiation.

Fig. 4.9 shows the measured differentiated pulses when the SBG-FPF is biased at different voltages. Fig. 4.9(a)-9(d) show the temporally differentiated pulses (blue-solid line) with differentiation orders of 1.52, 1.34, 1.15, and 0.99, respectively. The simulated output pulses with an ideal Gaussian pulse as an input signal to an ideal differentiator with the same orders are also shown (red-dashed line) for comparison. As can be seen, the experimentally generated pulses are close to the simulated pulses, which confirms the effectiveness of the

use of a SBG-FPF to perform a tunable fractional-order differentiator. The slight mismatch in the dip is mainly caused by the limited bandwidth of the PD. In addition, the notch wavelength shifting when the bias voltage is changed could be eliminated by incorporating three independent pairs of electrodes for the two reflectors and the cavity in the SBG-FPF which could be independently controlled. Thus, a tunable fraction-order temporal differentiator with a fixed resonance wavelength could be realized, and by programming the three independent electrodes, the tuning range of the differentiation order could also be increased. The key advantage of using an electrically tunable SBG-FPF for the implementation of a tunable fractional-order photonic temporal differentiator is its flexible and ultra-fast tunability.

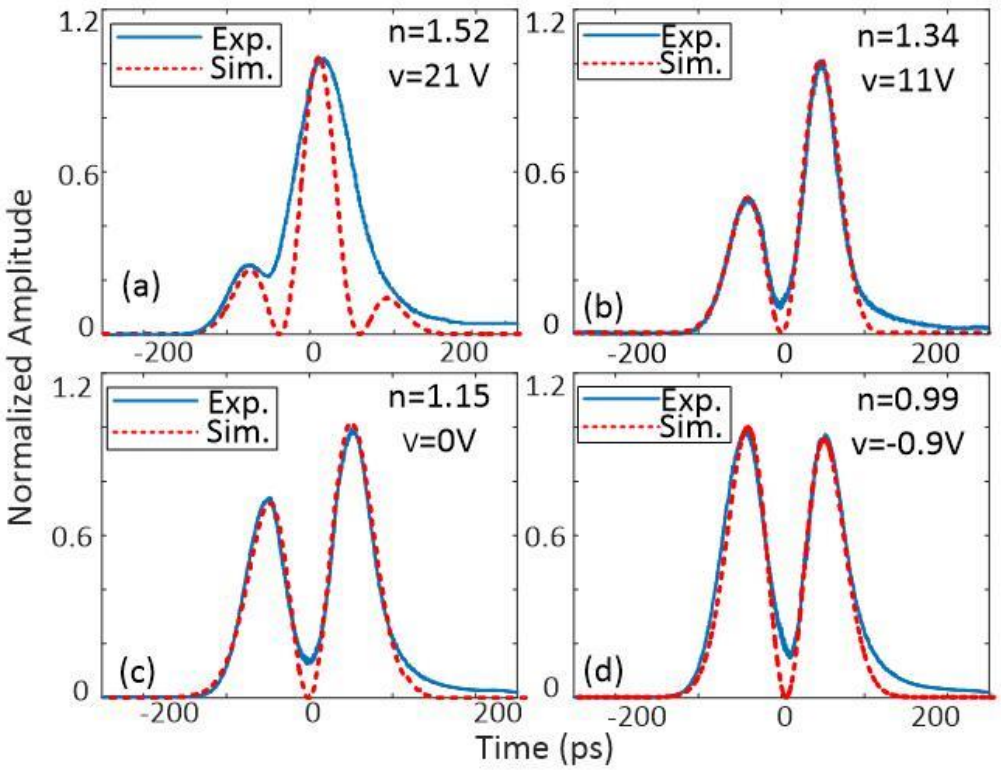

Fig. 4.9 Experimental results for differentiation-order tuning.

4.2.3 An electrically tunable optical delay line

An optical delay line, capable of controlling the time delay of an optical signal, is a basic photonic building block that enables many microwave photonic and optical processing operations such as photonic signal processing, photonic microwave filtering, and optically controlled phased array beamforming. Due to a strong light-confinement capacity of the optical cavity between the two reflectors (gratings) in the SBG-FPF, the SBG-FPF has a strong dispersion near the center of the notch and thus a large group delay. By tuning the applied bias voltage, the resonance wavelength of the SBG-FPF is shifted and thus the group delay is tuned. We propose to use the electrically tunable SBG-FPF for the implementation of a tunable optical delay line. To evaluate the performance of the fabricated SBG-FPF as a tunable optical delay line, an experiment is performed.

Fig. 4.10(a) illustrates the measured group delay response in the notch in the fabricated SBG-FPF. The SBG-FPF has a group delay as large as 110 ps at the notch center. Fig. 4.10(b) shows the electrical tunability of the group delay at three different wavelengths. As the bias voltage is increasing, the group delay is changed. For example, at 1538.012 nm, shown in the red line, as the bias voltage increases, the time delay is firstly increased to 95 ps from 32 ps at a bias voltage of 0 V and then is decreased to 35 ps when the bias voltage is 21 V. Note that for an optical delay line, a broad operation bandwidth is always preferred. The key advantage of using this tunable filter for the implementation of an optical delay line is its ultra-fast tuning speed in a scale of nano-seconds. However, the main disadvantage is a narrow operation bandwidth of this delay line.

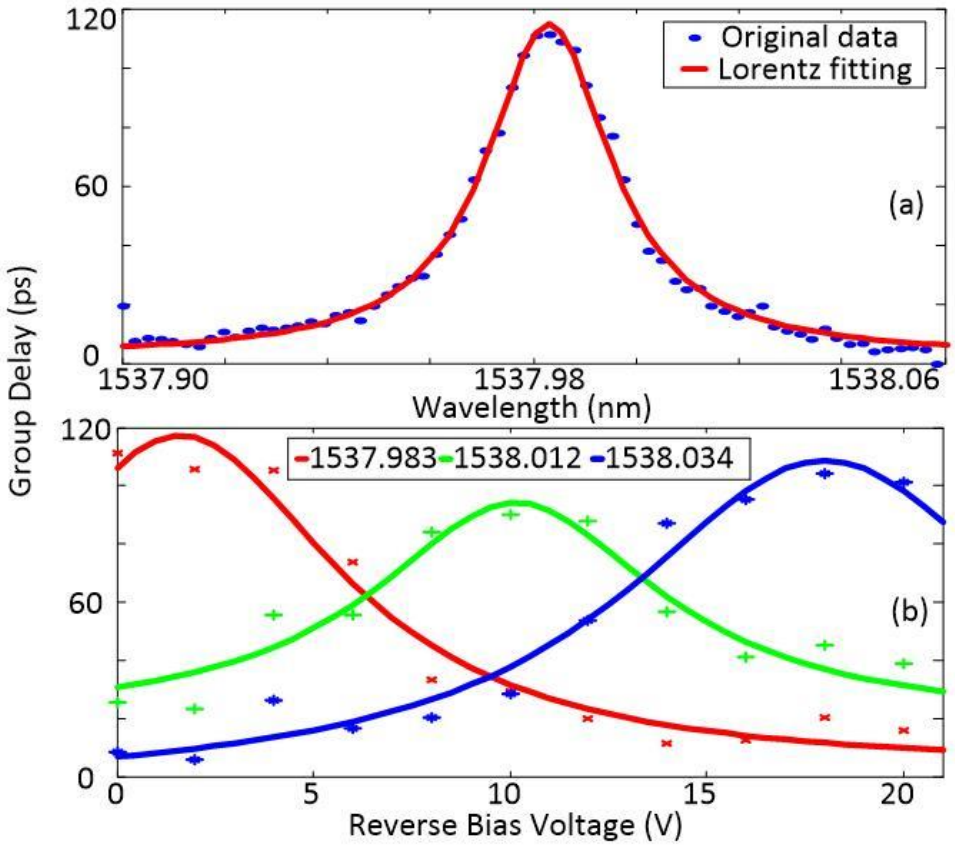

Fig. 4.10 (a) Measured group delay response in the notch of the fabricated PS-WBG and (b) electrical tunability of the group delay at three different wavelengths.

4.3 Conclusion

In conclusion, to have a waveguide grating that is wavelength tunable, we proposed to implement a tunable waveguide grating by incorporating a PN junction across the waveguide grating, to use the free-carrier plasma dispersion effect in silicon to achieve wavelength tuning. The use of a pair of wavelength-tunable waveguide gratings to form a wavelength-tunable Fabry-Perot resonator for microwave photonic signal processing was studied. Thanks to its electrical tunability, a high-speed electro-optic modulator, a tunable fractional-order photonic temporal differentiator and a tunable optical delay line were experimentally

demonstrated. The use of the tunable filter for implementation of an electro-optic modulator with a 3-dB modulation bandwidth of ~5.6 GHz was experimentally demonstrated, and the performance of using the filter to perform modulation of a 3.5 Gb/s 2^7-1 non-return-to-zero pseudorandom binary sequence was evaluated. The use of the tunable filter for the implementation of a tunable fractional-order photonic temporal differentiator with a tunable differentiation order from 0.99 to 1.53 was experimentally demonstrated. The key advantage of using an electrically tunable SBG-FPF for the implementation of a tunable fractional-order photonic temporal differentiator is its ultra-fast tunability. In addition, the use of the tunable filter for the implementation of an electrically tunable optical delay line with a tunable time delay as large as 110 ps was also experimentally demonstrated. The key advantage of using this tunable filter for the implementation of an optical delay line is its ultra-fast tuning speed in a scale of nano-seconds. However, the main disadvantage is a narrow operation bandwidth of this delay line.

CHAPTER 5 SILICON-BASED ON-CHIP LINEARLY CHIRPED WAVEGUIDE BRAGG GRATING

To increase the bandwidth of a waveguide grating, in this Chapter a linearly chirped waveguide Bragg grating (LC-WBG) is designed, fabricated and evaluated. By incorporating two LC-WBGs in two arms of a Mach-Zehnder interferometer (MZI) structure, an on-chip optical spectral shaper with a linearly-varying free spectral range (FSR) is produced. Applying the spectral shaper in a photonic microwave waveform generation system based on spectral-shaping and wavelength-to-time (SS-WTT) mapping, a linearly chirped microwave waveform (LCMW) with a large time-bandwidth product is experimentally generated.

5.1 Linearly chirped waveguide Bragg grating

To realize an optical delay line with a broad operation bandwidth, a linearly chirped waveguide Bragg grating (LC-WBG) with a linearly-varying grating period or effective index modulation along the gratings is a potential solution. However, due to the fabrication limitations, it is challenging to realize a silicon-based LC-WBG by linearly varying grating period. Therefore, it is common to achieve the chirp in a silicon-based LC-WBG by linearly varying index profile. For example, by apodizing the grating index profile, a silicon-based LC-WBG is achieved. However, the main disadvantage includes its large propagation loss and low fabrication tolerance.

5.1.1 Design of an LC-WBG

To make an LC-WBG with a smaller propagation loss and a higher fabrication tolerance, we propose an LC-WBG on the rib waveguide in which the chirp is realized by linearly varying the rib width along the gratings. The proposed LC-WBG has a single-mode rib waveguide, and the gratings are realized by introducing periodic sidewall corrugations on the slab. By keeping the grating period constant and linearly increasing the width of the rib along the grating, a linear chirp is produced since the effective refractive index is linearly increasing as the rib width linearly increases.

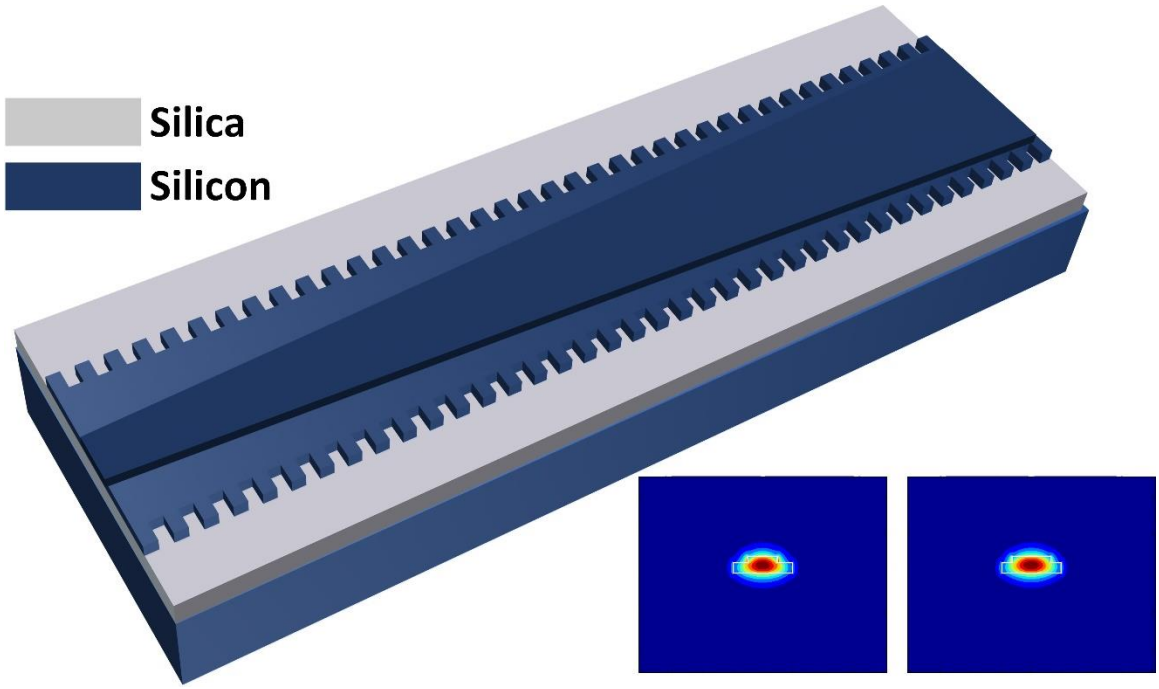

Fig. 5.1 Perspective view of the proposed LC-WBG. (Inset: Simulated fundamental TE mode profile of the rib waveguide with the rib width of 500 nm (left) and 650 nm (right)).

Fig. 5.1 shows the perspective view of the proposed LC-WBG. The grating is realized by introducing periodic sidewall corrugations on the slab. By keeping the grating period constant and linearly increasing the width of the rib along the grating, a linear chirp is

produced since the effective refractive index is linearly increasing as the rib width increases. The inset in Fig. 5.1 shows the simulated fundamental TE mode profile in the rib waveguide with a rib width of 500 nm (left) and 650 nm (right).

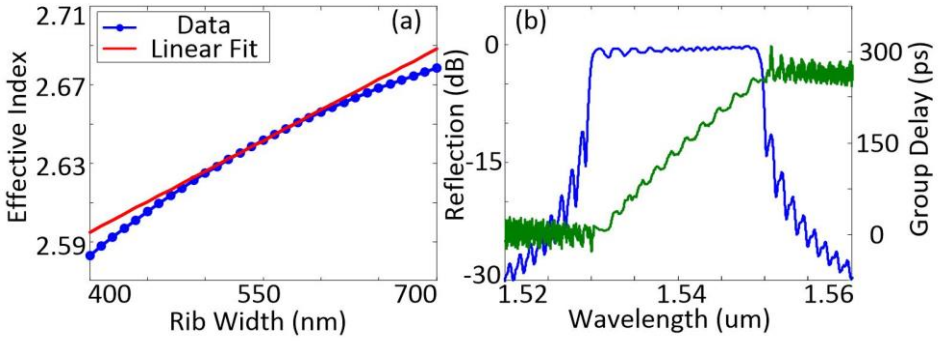

Fig. 5.2 (a) Effective refractive index for the fundamental TE mode in the rib waveguide at 1550 nm when the rib width is increasing; (b) simulated spectral and group delay responses of the LC-WBG with the rib width increasing from 500 to 550 nm.

Fig. 5.2(a) shows the effective refractive index of the fundamental TE mode in the rib waveguide at 1550 nm as the rib width increases from 400 to 700 nm, as indicated in blue line. The red curve gives the linear-fitting of the effective refractive index. As can be seen, the effective refractive index of the waveguide is linearly increasing, especially when the rib width increases from 500 to 590 nm. Thus, an LC-WBG is realized. The advantage of such an LC-WBG is that the grating period is uniform, which is more robust than varying the grating period to implement an LC-WBG [136]. To enable the LC-WBGs to work in the C band, the grating period is determined to be 300 nm with a duty cycle of 50%. The length of each of the LC-WBGs is 12.54 mm, to achieve a time delay of 223 ps. Fig. 5.2(b) shows the simulated reflection spectrum (blue) and the group delay (green) of the LC-WBG with the rib width increasing from 500 to 550 nm. The grating exhibits a time delay of 220 ps between

1530~1550 nm and thus has a dispersion value of 11 ps/nm and a chirp rate of 1.59 nm/mm. It is worth noting that the broad reflection bandwidth of the LC-WBG is due to the strong index modulation, which is much higher than that of a conventional linearly chirped fiber Bragg grating. The proposed LC-WBG is sent for fabrication using a CMOS-compatible technology with 193-nm optical projection lithography at IMEC, Belgium, accessed via ePIXfab.

5.1.2 Evaluation of an LC-WBG

The optical performance of the LC-WBGs is evaluated. The spectral and group delay responses of an LC-WBG are measured using an optical vector analyzer (LUNA OVA CTe). Fig. 5.3(a) shows the normalized reflection spectrum in blue and the group delay in green of an LC-WBG with the rib width linearly increasing from 500 to 550 nm. The grating exhibits a time delay of 228 ps between 1533~1544 nm and thus has a dispersion value of 20.7 ps/nm and a chirp rate of 0.88 nm/mm, which agree well with the simulated results in Fig. 5.2(b), except that the bandwidth becomes relatively smaller due to the inevitable fabrication imperfections. Fig. 5.3(b) shows the normalized reflection spectrum and the group delay of an LC-WBG with the rib width linearly increasing from 500 to 600 nm. The grating exhibits a time delay of 236 ps between 1534~1554 nm and thus has a dispersion value of 11.8 ps/nm and a chirp rate of 1.59 nm/mm. Fig. 5.3(c) shows the normalized reflection spectrum and the group delay of an LC-WBG with the rib width linearly increasing from 500 to 650 nm. The grating exhibits a time delay of 241 ps between 1533~1562 nm and thus has a dispersion value of 8.3 ps/nm and a chirp rate of 2.31 nm/mm. As can be seen, it is easy to control the chirp rate of an LC-WBG by varying the rib width.

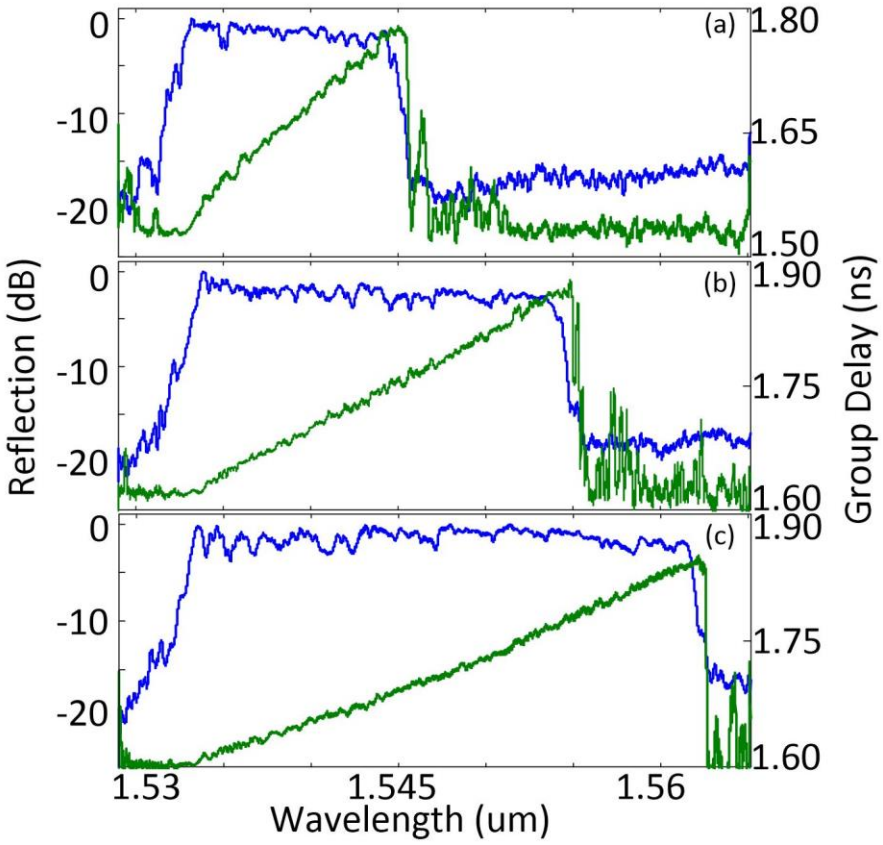

Fig. 5.3 Measured spectral and group delay responses of an LC-WBG with the rib width increasing from 500 to (a) 550 nm, (b) 600 nm, and (c) 650 nm.

The key advantage of the proposed LC-WBG is that the grating period of the LC-WBG is uniform and the chirp is achieved by varying the rib width, which is more robust than varying the grating period to achieve the chirp. In addition, thanks to the large cross section of the rib waveguide, the propagation loss is reduced and the fabrication tolerance is increased. When acting as an optical delay line, the LC-WBG could find applications such as data buffering in optical switches [137] and optical beamforming in phased-array antennas [138]. Furthermore, compared with other integrated delay lines comprising of MRRs or photonic

crystal waveguides [139], such an LC-WBG provides a broader bandwidth and a comparatively smaller optical transmission loss.

5.2 Its application in photonic generation of linearly chirped microwave waveform

In modern radar systems, microwave pulse compression has been widely used to increase the range resolution. Particularly, a linearly chirped microwave waveform (LCMW) with a large time-bandwidth product (TBWP) in the order of 10^2 or 10^3 is highly preferred for microwave pulse compression. Thanks to the broad bandwidth inherent to photonics, photonic generation of microwave waveform with a high central frequency and wide bandwidth has been extensively researched. Due to the flexibility and simplicity, spectral-shaping and wavelength-to-time (SS-WTT) mapping has been considered one of the most important photonic-assisted solutions for arbitrary microwave waveform generation. In a typical SS-WTT mapping system, the optical spectral shaper is the key device which is specifically designed to have a spectral response with a shape that is a scaled version of the microwave waveform to be generated. For LCMW generation, the spectral shaper usually has a spectral response with an increasing or decreasing free spectral range (FSR). Recently, for a better stability and lower power consumption, on-chip optical spectral shaper has been proposed and used in a photonic microwave waveform generation system based on SS-WTT mapping for LCMW generation. However, the TBWP of the generated LCMW is too small.

To generate an LCMW with a high TBWP, we propose a silicon-based on-chip optical spectral shaper for the generation of an LCMW. The on-chip optical spectral shaper has a Mach-Zehnder interferometer (MZI) structure that incorporates two identical LC-WBGs

with opposite chirp rates in the two arms. By adding an offset waveguide to one arm of the MZI and controlling the length of the offset waveguide, the spectral response of the shaper can be controlled to have a symmetrical, linearly increasing, or linearly decreasing FSR, which is needed for the generation of an LCMW based on SS-WTT mapping. The key advantage of the proposed on-chip spectral shaper is that two identical LC-WBGs with opposite chirp rates in the two arms of the MZI are used which enables the system to generate an LCMW with a high chirp rate and a large TBWP. In addition, the use of the two LC-WBGs will also balance the losses of the two arms, thus making the spectral shaper with a spectral response having a high extinction ratio. Furthermore, the grating period of the LC-WBGs is uniform and the chirp rate is changed by varying the rib width, which is more robust than varying the grating period to achieve the chirp.

5.2.1 Design of an optical spectral shaper

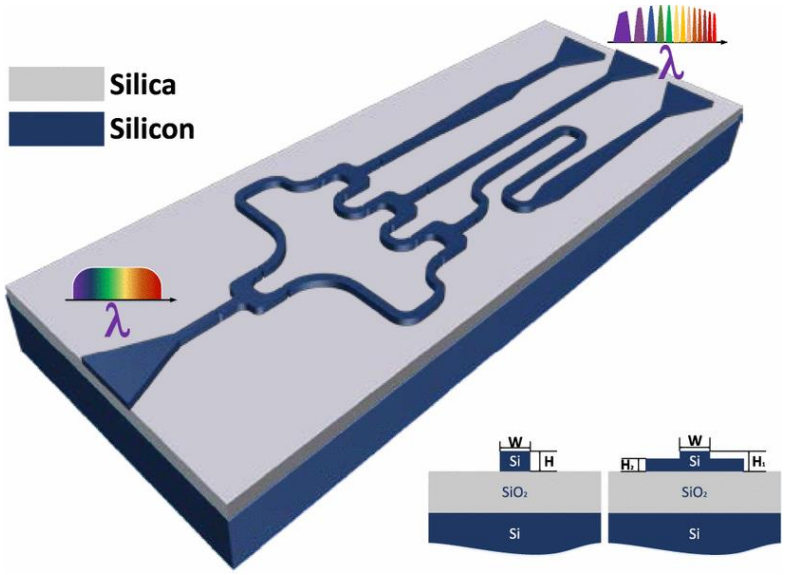

Fig. 5.4 Perspective view of the proposed on-chip silicon-based optical spectral shaper. (Inset: (Left) Wire waveguide and (Right) Rib waveguide.

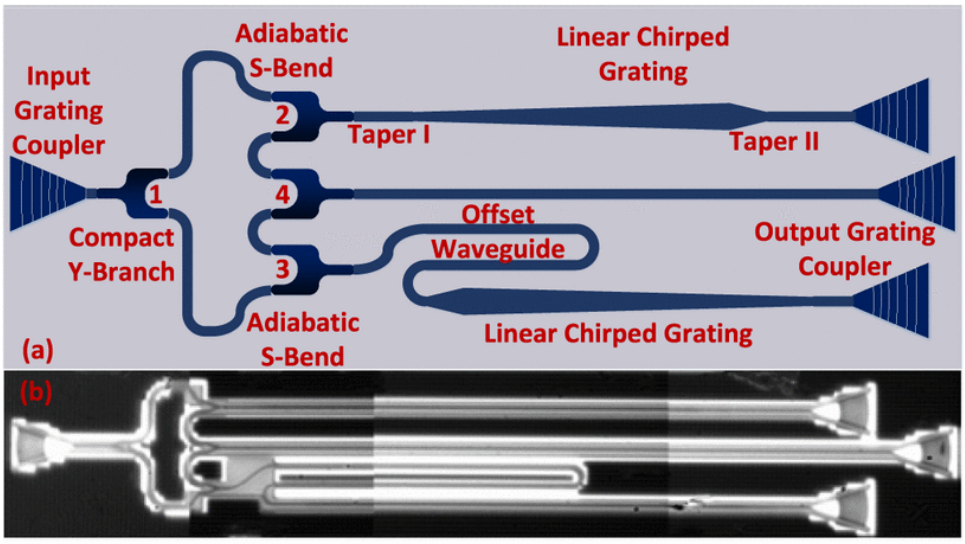

Fig. 5.5 (a) Schematic layout of the designed on-chip spectral shaper; (b) image of the fabricated spectral shaper with the length of the offset waveguide equal to the length of the LC-WBG captured by a microscope camera.

Fig. 5.4 illustrates the perspective view of the proposed on-chip spectral shaper. The inset shows the fundamental structures of the strip waveguide and rib waveguide in the chip. To ensure a single transverse-electric (TE) mode operation, the strip waveguide is designed to have a width of 500 nm and a height of 220 nm, and the rib waveguide is designed to have a width of 500 nm, a height of 220 nm, and a slab thickness of 150 nm. Both waveguides are fabricated on top of a buried oxide layer (2 μm thick) on a silicon wafer. Fig. 5.5(a) presents the schematic layout of the proposed on-chip spectral shaper, which has an MZI structure that incorporates two identical LC-WBGs with opposite chirp rates in its two arms. Two TE-mode grating couplers are employed to couple the light into or out of the chip. The input light is split by the 1st compact Y-branch into two beams to travel through the LC-WBGs in the upper and lower arms. Spectral components of the light waves of different wavelengths are reflected from different positions in the LC-WBGs. By the 2nd and 3rd Y-branches, the

reflected light waves are collected and recombined at the 4th Y-branch. The combined light wave is guided to the output grating coupler for coupling out of the chip. As a result of the optical interference at the recombination, the optical spectral shaper with a wavelength-dependent FSR is achieved. The FSR of the optical spectral shaper is defined here as the wavelength separation between two adjacent spectral peaks. To generate an LCMW based on the SS-WTT mapping technique, an increasing or decreasing FSR is usually required. In addition, an offset waveguide is added in the lower arm of the spectral shaper to control the length difference between the two arms which would lead to the change of the central frequency of the generated LCMW. By carefully designing the LC-WBGs and the length of the offset waveguide, the spectral response of the spectral shaper is controlled to have a symmetrical, a uniformly increasing or decreasing FSR. To minimize the chip footprint, the strip waveguide is mostly used to guide the light, and to reduce the bending loss, bend waveguides with a radius of 12 μm and adiabatic S-shape waveguide bends [140] are employed to direct the light. The rib waveguides are used in the implementation of the LC-WBG. Due to the different waveguide structures between the strip waveguide and the rib waveguide, a double-layer linear taper waveguide is required to achieve the mode transition. As shown in Fig. 5.5(a), there is a taper with a length of 50 μm at each of the two ends of the LC-WBGs. Note that at the right end of each of the LC-WBGs, a grating coupler is used as a waveguide terminator by irradiating the transmitted light to avoid reflection. The proposed spectral shaper is sent for fabrication using a using a CMOS compatible process with 193-nm deep ultraviolet lithography at IMEC, Belgium, accessed via ePIXfab. Fig. 5.5(b) shows the image of the fabricated spectral shaper with the length of the offset waveguide equal to the length of the LC-WBG captured by a microscope camera. The length of an LC-WBG is

12.54 mm and the entire on-chip spectral shaper incorporating two LC-WBGs has a size of 12.70 mm in length and 0.081 mm in width, giving a small footprint of 1.03 mm^2.

5.2.2 Evaluation of an optical spectral shaper

The optical performance of the fabricated on-chip spectral shaper is evaluated. In the fabricated spectral shaper, the rib width of two LC-WBGs is varied from 500 to 550 nm. Fig. 5.6(a) shows the simulated spectral response of the on-chip spectral shaper with the length of the offset waveguide equal to zero. Since the length of the offset waveguide is zero, the spectral response presents a symmetrical FSR, and away from the center the FSR is linearly increasing. Fig. 5.6(b) shows the measured spectral response of the fabricated spectral shaper with the length of the offset waveguide equal to zero, and the inset shows the zoom-in view of part of the spectral response. As can be seen, the spectral response agrees well that shown in Fig. 5.6(a) except the different bandwidths caused by the fabrication imperfections. Fig. 5.6(c) shows the simulated spectral response of the on-chip spectral shaper, in which the length of the offset waveguide is set to be equal to the length of the LC-WBG. Note that due to the waveguide structure difference between the offset waveguide and the LC-WBG waveguide, the lengths are the effective lengths. The spectral response presents a linearly decreasing FSR. Fig. 5.6(d) shows the measured spectral response of the fabricated spectral shaper with the length of the offset waveguide equal to the length of the LC-WBG and the inset shows the zoom-in view of part of spectral response. Again, the spectral response agrees well with that shown in Fig. 5.6(c) except the different bandwidth caused by the fabrication imperfections. It is worth noting that the measured spectral responses show a reduced modulation depth, which is mainly caused by the limited resolution of the optical vector analyzer. In addition, the insertion loss of the fabricated spectral shaper is measured to be

around 30 dB, which is mainly resulted from the fiber-to-fiber coupling loss and the splitting loss at the Y-branch. To ensure a full view of the spectrums, the different wavelength ranges on the x-axis are used in Fig. 5.6.

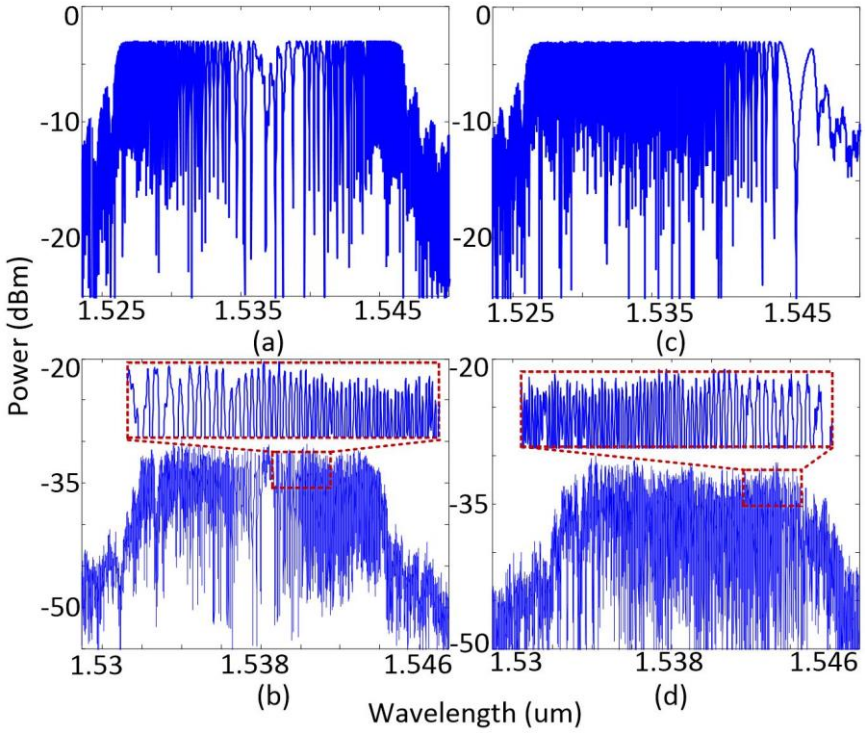

Fig. 5.6 Simulated spectral response of an on-chip spectral shaper when the length of the offset waveguide is equal to (a) zero, and (c) the length of the LC-WBG. Measured spectral response of a fabricated spectral shaper when the length of the offset waveguide is equal to (b) zero, and (d) the length of the LC-WBG.

5.2.3 Theoretical principle of photonic generation of an LCMW based on SS-WTT mapping

The fundamental principle of the SS-WTT mapping technique is illustrated in Fig. 5.7. An ultrashort optical pulse emitted from a mode-locked laser is first spectrally shaped by the on-chip optical spectral shaper. Then, the spectrum-shaped optical pulse is sent to a dispersive

element to perform linear wavelength-to-time mapping. At the output of a high-speed PD, a microwave waveform with the shape identical to that of the shaped optical spectrum is generated.

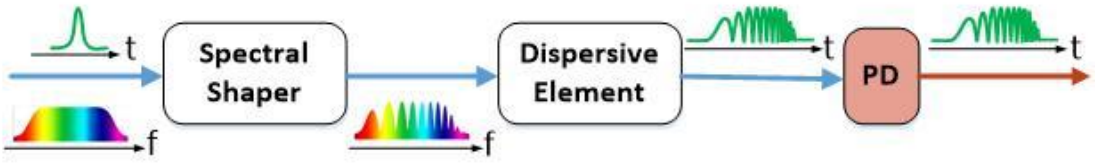

Fig. 5.7 Schematic of a microwave waveform generation system based on SS-WTT mapping technique.

Mathematically, the on-chip spectral shaper incorporating two identical LC-WBGs with the opposite chirp rates can be modeled as a two-tap delay-line filter. The transfer function of the spectral shaper is given by

$$T(\lambda)=\frac{1}{2}W(\lambda)\left[1+\cos\left(\frac{2\pi n_{eff}}{\lambda}2\Delta L\right)\right],\quad \left(\left|\lambda-\lambda_0\right|\le\frac{B_\lambda}{2}\right) \tag{5-1}$$

where $W(\lambda)$ is the intensity reflection spectrum of the LC-WBG, B_λ is the bandwidth of the spectral shaper where we assume that the input ultra-short pulse has a spectral width that is wider than the bandwidth of the spectral shaper, n_{eff} is the effective refractive index of the waveguide, and ΔL is the length difference between the two arms of the MZI in the spectral shaper, which includes the wavelength-independent path difference ΔL_0 caused by the offset waveguide (since the length of the offset waveguide is small, the dispersion can be ignored), and the wavelength-dependent length difference introduced by the chirp of the LC-WBG $\Delta L_1(\lambda)$. ΔL_0 can be controlled by selecting the length of the offset waveguide, and $\Delta L_1(\lambda)$

is determined by the bandwidth and the chirp rate of the LC-WBG, which can be calculated using $\Delta L_1(\lambda) = \delta\lambda / C$, where $\delta\lambda$ (nm) is the wavelength detuning from the center wavelength λ_0, and C (nm/mm) is the chirp rate of the LC-WBG. Note that $\delta\lambda$ is positive when the reflection position is at shorter wavelength than λ_0, and $\delta\lambda$ is negative when the reflection position is at longer wavelength than λ_0. Then, the transfer function $T(\lambda)$ can be rewritten as

$$T(\lambda) = \frac{1}{2} W(\lambda) \left\{ 1 + \cos\left[\frac{2\pi}{\lambda} \left(2 n_{eff\,0} \Delta L_0 + 2 \cdot 2 n_{eff\,1} \Delta L_1 \right) \right] \right\} \tag{5-2}$$

where $n_{eff\,0}$ is the effective refractive index of the strip waveguide and $n_{eff\,1}$ is the average effective refractive index of the rib waveguide along the grating. At 1550 nm, the effective refractive index of the strip waveguide for the fundamental TE mode is calculated to be 2.379, and the effective refractive index of the rib waveguide is calculated to be 2.627. It is worth noting that since a pair of LC-WBGs with opposite chirp rates are incorporated in the two arms of the MZI, the wavelength-dependent length difference introduced by ΔL_1 is doubled, which also leads to the doubling in the chirp rate, and thus the TBWP of the generated microwave waveform.

The spectral response presents a varying FSR due to the chirp of the LC-WBGs. The FSR of the optical spectral shaper response is a function of wavelength and can be expressed as

$$FSR = \frac{\lambda^2}{2 n_{eff} \Delta L} \cong \frac{\lambda_0^2}{2\left(n_{eff\,0} \Delta L_0 + 2 n_{eff\,1} \dfrac{\delta\lambda}{C} \right)} \tag{5-3}$$

According to (5-3), by properly selecting the parameters of the LC-WBGs and controlling the length of the offset waveguide, the FSR of the optical spectral shaper can be specifically controlled to be symmetrical, linearly increasing or decreasing.

The spectrum-shaped optical pulse is then sent to the dispersive element and the shaped spectrum is mapped to a temporal microwave waveform thanks to the dispersion-induced linear WTT mapping, and then detected by the high-seed PD. According to the mapping relationship, the converted time-domain microwave waveform is given by

$$y(t) \propto \frac{1}{2} W\left(\frac{t}{\ddot{\Phi}_\lambda}\right)\left\{1+\cos\left[\frac{4\pi}{\lambda_0^2}\times\frac{t}{\ddot{\Phi}_\lambda}\left(n_{eff\,0}\Delta L_0 + 2n_{eff\,1}\frac{\delta t}{C\ddot{\Phi}_\lambda}\right)\right]\right\} \tag{5-4}$$

where δt is the time detuning from the center of the temporal waveform, which is given by the mapping relationship $\delta\lambda \rightarrow \delta t/\ddot{\Phi}_\lambda$, and $\ddot{\Phi}_\lambda$ is the group velocity dispersion (GVD) of the dispersive element. The time-domain duration of the generated microwave waveform is determined by the window function $W\left(t/\ddot{\Phi}_\lambda\right)$ and is calculated by $\Delta T = B_\lambda \ddot{\Phi}_\lambda$.

The instantaneous microwave frequency of the generated waveform can be obtained from the phase term of (5-4), which is given by

$$f_{RF}(\delta t) = \frac{1}{2\pi}\times\frac{d\Psi}{dt} = \frac{2}{\lambda_0^2}\times\frac{n_{eff\,0}\Delta L_0}{\ddot{\Phi}_\lambda} \pm \frac{4}{\lambda_0^2}\times\frac{n_{eff\,1}\delta t}{C\ddot{\Phi}_\lambda^2} \tag{5-5}$$

As can be seen the generated microwave waveform is linearly chirped. For a given dispersive element, the central frequency of the generated chirped microwave waveform is given by

$$f_{RF}(\delta t = 0) = \frac{1}{2\pi} \times \frac{d\Psi}{dt} = \frac{2}{\lambda_0^2} \times \frac{n_{eff\,0} \Delta L_0}{\ddot{\Phi}_\lambda} \tag{5-6}$$

which is only determined by the length of the offset waveguide. Thus, LCMWs with different chirp profiles (symmetrical and uniform) can be generated by simply tuning ΔL_0.

The chirp rate of the generated microwave waveform, given by

$$CR = \frac{df_{RF}(\delta t)}{dt} = \pm \frac{4}{\lambda_0^2} \times \frac{n_{eff\,1}}{C\ddot{\Phi}_\lambda^2} \tag{5-7}$$

which is dependent on the chirp rate of the LC-WBG and the GVD of the dispersive element. A positive or negative chirp rate corresponds to a positive and negative value of ΔL_0, respectively. By carefully designing the length of the offset waveguide and choosing the chirp rate of the LC-WBG, an LCMW with required chirp profile can be generated.

The pulse compression ratio is determined by the TBWP of the transmitted microwave waveform. In our system, the TBWP of the generated LCMW is givens by

$$TBWP = CR \times \Delta T^2 = \frac{4}{\lambda_0^2} \times \frac{n_{eff\,1}}{C} B_\lambda^2 \tag{5-8}$$

It is shown that the TBWP is independent of the GVD of the dispersive element in the system but is determined by the chirp rate and the bandwidth of the LC-WBGs.

5.2.4 Experimental results of LCWM generation

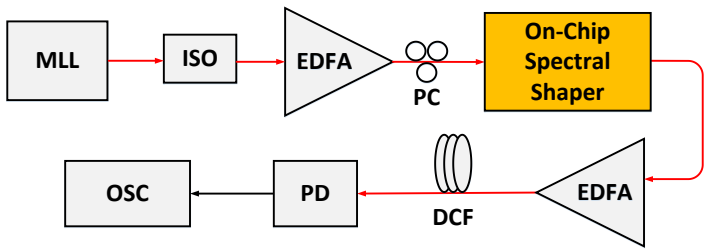

Fig. 5.8 Experimental setup. MML: mode lock laser. ISO: isolator; EDFA: erbium-doped fiber amplifier. PC: polarization controller. DCF: dispersion compensating fiber. PD: photodetector. OSC: oscilloscope.

Fig. 5.8 shows the experimental setup. An optical Gaussian pulse train generated by a mode-lock laser (MLL) (Pritel 1550-nm Picosecond and Femtosecond Fiber Lasers) with a pulse duration of approximately 600 fs and a repetition rate of 40 MHz is sent to the on-chip spectral shaper via an isolator and after amplification by an EDFA. The spectral width of an optical pulse in the pulse train is 12 nm, which is wider than the bandwidth of the spectral shaper. The EDFA is used to increase the power of the optical pulse. A polarization controller (PC) is connected between the EDFA and the spectral shaper to adjust the state of polarization (SOP) of the input signal to minimize the polarization-dependent loss. After spectral shaping by the spectral shaper, a spectrally-shaped optical pulse is obtained which is first amplified by a second EDFA and then sent to a dispersion compensating fiber (DCF) serving as a dispersive element to perform WTT mapping. The optical intensity envelope is then converted to a microwave signal at a PD with a bandwidth of 45 GHz (NewFocus Model 1014), and the generated time-domain microwave signal is monitored using a sampling oscilloscope with a bandwidth of 63 GHz (OSC, Agilent 86116A).

First, an on-chip spectral shaper with the length of the offset waveguide equal to zero is incorporated into the SS-WTT mapping system to generate an LCMW with a symmetrical

chirp profile. An ultra-short optical pulse is spectrum shaped by the spectral shaper, and is then sent to the DCF (with a GVD of -1020 ps/nm) to perform WTT mapping to generate a chirped microwave waveform. As shown in Fig. 5.9(a), an LCMW with a symmetrical chirp profile is generated. The pulse duration is around 10.90 ns. The spectrogram of the generated LCMW is calculated and is shown in Fig. 5.9(b). As can be seen, the waveform is chirped with a symmetrical chirp profile. To further confirm the chirp of the waveform, the instantaneous microwave frequency based on Hilbert transform is also calculated [141] and given by the red-dotted line in Fig. 5.9(b), which agrees well with the spectrogram. The central frequency of the generated symmetrically chirped microwave waveform is 1.2 GHz, which is different from the theoretical prediction of 0 GHz according to (5-5). Such a difference is due to a small asymmetry between the two arms of the MZI in the spectral shaper, which is caused by fabrication imperfections. On the right side of the center, the instantaneous frequency is linearly increasing with a positive chirp rate of 5.4 GHz/ns, which agrees quite well with the theoretical predictions of 4.8 GHz/ns by (5-7). On the left side of the center, the instantaneous frequency is linearly decreasing with a negative chirp rate of -4.9 GHz/ns. The small difference in the chirp rates is resulted from a small asymmetry of the two LC-WBGs in the two arms of the MZI, which is also caused by fabrication imperfections. According to the time-domain waveform and its carrier frequency distribution, the TBWP of the generated LCMW is estimated to be around 359.7. Fig. 5.9(c) shows the compressed pulse with a pulse width of 24 ps, which is obtained by calculating the autocorrelation of the generated microwave waveform. Note that before calculating the autocorrelation, the direct-current component in the generated LCMW is filtered out. By comparing the pulse width of the waveforms in Fig. 5.9(a) and 9(c), a pulse compression ratio as large as 454.2 is obtained.

Then, a second on-chip spectral shaper with the length of the offset waveguide equal to the length of the LC-WBG is incorporated into the SS-WTT mapping system to generate an LCMW with a linearly increasing chirp. Note that the input optical pulse is the same as the one in the first experiment. The spectrum-shaped optical pulse is then sent to the DCF (with a GVD of -1700 ps/nm) where the spectrum is mapped to the time domain to generate a chirped microwave waveform. As shown in Fig. 5.10(a), an LCMW with a linearly increasing chirp is generated. The pulse duration is around 20.5 ns. Fig. 5.10(b) shows the spectrogram plot of the generated LCMW. To further confirm the linear chirp, the instantaneous microwave frequency is given by the red-dotted line. Again, the results agree well with the spectrogram. The center frequency of the generated LCMW is 15.8 GHz, which agrees well with the theoretical prediction of 16.4 GHz according to (5-6). The LCMW has a positive chirp rate of 1.54 GHz/ns, which also agrees well with the theoretical prediction of 1.42 GHz/ns by (5-7). According to the time-domain waveform and its carrier frequency distribution, the TBWP of the generated LCMW is estimated to be around 615, which also agrees well with the theoretically predicted TBWP of 612.5 by (5-8). Fig. 5.10(c) shows the compressed pulse with a pulse width of 32.9 ps, which is obtained by calculating the autocorrelation of the generated microwave waveform. By comparing the pulse width of the waveforms in Fig. 5.10(a) and 10(c), a pulse compression ratio as large as 623.1 is obtained.

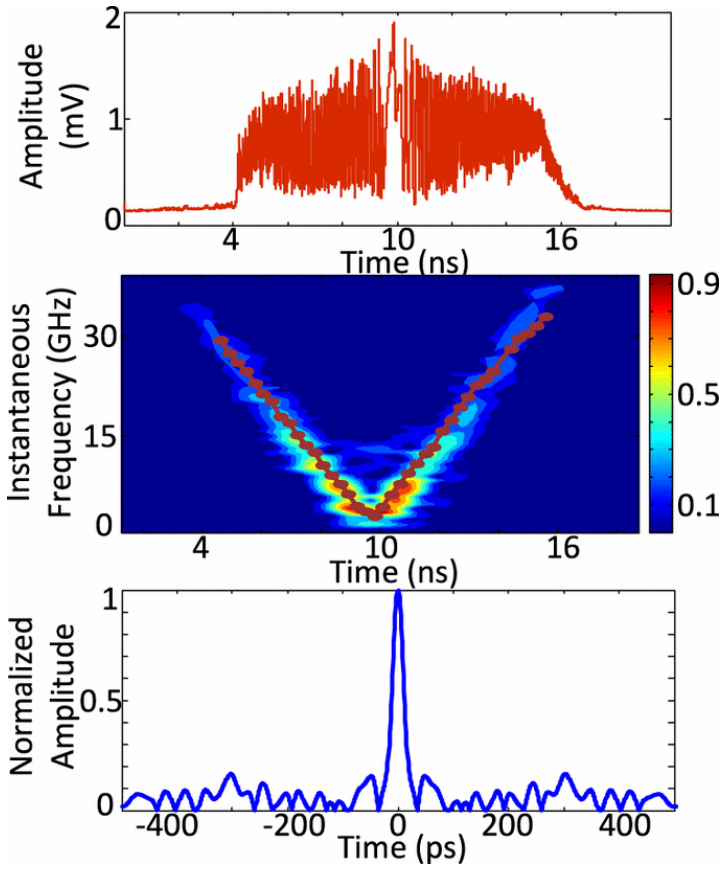

Fig. 5.9 Experimental results: (a) the generated LCMW; (b) the spectrogram and instantaneous frequency of the generated LCMW; and (c) the compressed pulse by autocorrelation.

The two generated LCMWs shown in Fig. 5.9 and Fig. 5.10 have different chirp rates, since the dispersive element (DCF) for WTT mapping has different GVD. In addition, to further increase the TBWP, we may increase the rib widths along the gratings to increase the reflection bandwidths of the LC-WBGs. Thus, the spectral shaper could have a wider bandwidth. However, it is worth noting that in the theoretical analysis we assume that the input ultra-short pulse has a wider spectral width than the bandwidth of the spectral shaper, and B_λ is determined to be the bandwidths of the LC-WBGs. In fact, when the bandwidth of the spectral shaper is wider than the spectral bandwidth of the input ultra-short pulse, B_λ is

determined by the spectral bandwidth of the input ultra-short pulse. Furthermore, the proposed LC-WBG is capable of functioning as a dispersive element in a SS-WTT mapping system. Therefore, it is feasible to integrate an optical spectral shaper and a dispersive element on a single chip. However, the central frequency and the chirp rate of the generated LCMW are dependent on the GVD of the dispersive element. In the experiments, the DCFs with GVDs of -1020 and -1700 ps/nm were used to ensure that the frequencies of the generated LCMWs are within the bandwidth of the PD. Although an LC-WBG can be used as the dispersive element, its comparatively small GVD hinders. By increasing the length of an LC-WBG, the GVD could be increased, and so are the insertion loss and the footprint. There is a trade-off between the achieved GVD of the LC-WBG and its footprint and insertion loss, which should be taken into consideration in the design.

The key feature of the spectral shaper is that an LCMW with a large chirp rate and a large TBWP can be generated, which is achieved by incorporating a pair of LC-WBGs with large and opposite chirp rates in the spectral shaper. In addition, it is interesting to observe from the experimental results in Fig. 5.9 and Fig. 5.10 that as the length of the offset waveguide in the spectral shaper is varied from zero to the length of the LC-WBG, the central frequency of the generated LCMWs is changed from 1.2 to 15.8 GHz. The offset waveguide with different lengths leads to a different central frequency of the generated LCMW, which will bring benefit to the generation of an LCMW with a tunable central frequency, chirp rate and TBWP.

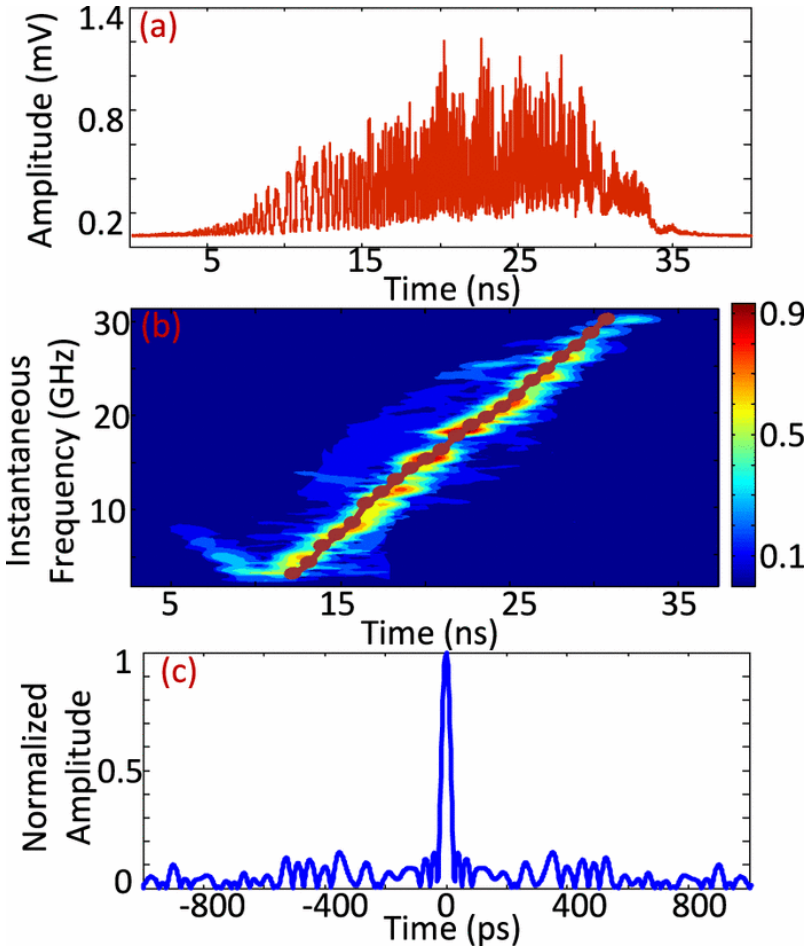

Fig. 5.10 Experimental results: (a) the generated LCMW; (b) the spectrogram and instantaneous frequency of the generated LCMW; and (c) the compressed pulse.

5.2.5 Experimental results of central frequency tunability of the LCMW

We also evaluate the generation of an LCMW with a tunable central frequency by changing the center wavelength of the input ultra-short pulse. In the experiment, a spectral shaper incorporating a pair of LC-WBGs with the rib waveguide width linearly increasing from 500 to 600 nm is incorporated into the SS-WTT mapping system. Fig. 5.11 shows the measured spectral response of the spectral shaper with the length of the offset waveguide equal to zero, and the dashed line presents the input optical pulse spectrum with the different center

wavelength from a tunable MLL. As can be seen, the spectral response presents a symmetrical FSR, and the FSR is linearly increasing on both sides. Due to the strong index modulation in the waveguide gratings, the reflection bandwidths of the LC-WBGs are very broad, which leads to a broader working bandwidth of the spectral shaper than the input optical pulse spectra width. Thus, by locating the center wavelength of the input pulse at different positions along the gratings, the path difference between the two arms of the MZI is different, which is equivalent to varying the length of the offset waveguide. Therefore, by tuning the central wavelength of the input optical pulse, the central frequency of the generated LCMW is tuned

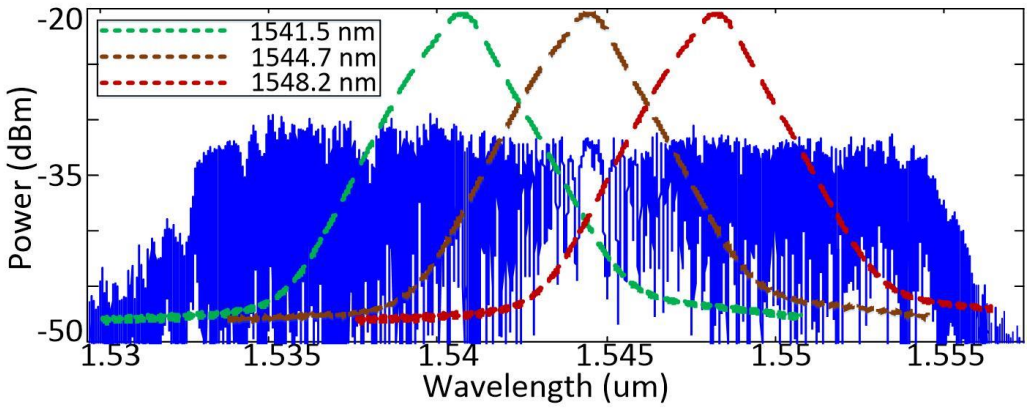

Fig. 5.11 Measured spectral response of a fabricated spectral shaper with the rib waveguide width in the LC-WBGs linearly increasing from 500 to 600 nm when the length of the offset waveguide is equal to zero. (The dashed line is the input optical pulse spectrum with the different center wavelength from a tunable MLL.)

Fig. 5.12 illustrates the experimentally generated LCMWs when the center wavelength of the input optical pulse is tuned at 1541.5 nm, 1544.7 nm, and 1548.2 nm. It is clear to see that as the center wavelength of the input optical pulse is changed, the central frequency of the generated LCMWs is changed. In addition, the chirp profile of the generated LCMW is

varied from a linearly increasing chirp profile, to a symmetrical chirp profile, to a linearly decreasing chirp profile. Table 5.1 lists the chirp rates, TBWPs and compression ratios of the generated LCMWs.

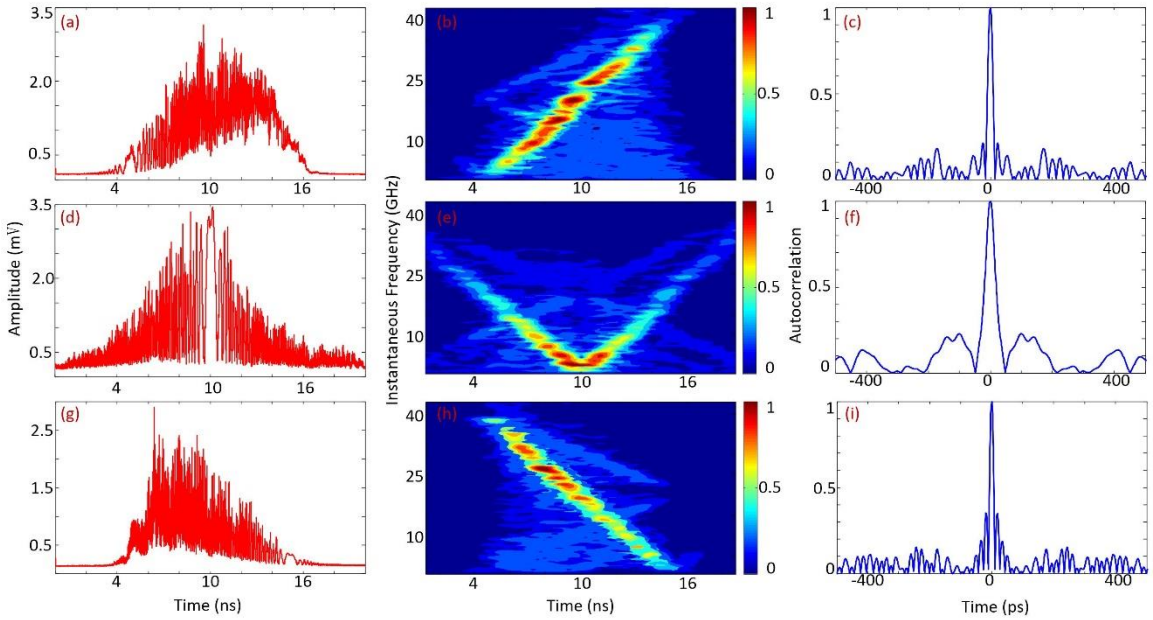

Fig. 5.12 Experimental results using an on-chip spectral shaper with the length of the offset waveguide equal to zero when the center wavelength of the input optical pulse is 1541.5 nm, 1544.7 nm, and 1548.2 nm, respectively: (a) the generated LCMW, (b) the spectrogram, and (c) the compressed pulse; (d) the generated LCMW, (e) the spectrogram, and (f) the compressed; (g) the generated LCMW, (h) the spectrogram, and (i) the compressed pulse.

Thanks to the strong index modulation in the waveguide gratings, the broad bandwidth of the LC-WBGs enables the spectral shaper to have a broader spectral width than the input optical pulse. Thus, by varying the center wavelength of the input optical pulse, the central frequency of the generated LCMW could be tuned. In addition, by taking advantage of plasma dispersion effect in silicon, it is appealing to realize an electrically tunable LC-WBG

and thus an electrically tunable spectral shaper. Then, it is feasible to integrate an electrically tunable optical spectral shaper and an electrically tunable dispersive element on a single chip, which offers full reconfigurability of the system in terms of central frequency and chirp rate tuning of the generated LCMW.

Table 5.1 Properties of the generated LCMWs

Generated LCMWs	Chirp Rate (GHz/ns)*	TBWP	Compression Ratio
Fig. 5. 11(a)	+ 4.9	238	250
Fig.5. 11(d)	-4.4, +4.8	107	132
Fig.5. 11(g)	-4.9	229	260

*The plus sign represents a linearly increasing chirp profile, while the minus sign represents a linearly decreasing chirp profile.

5.3 Conclusion

In conclusion, to increase the bandwidth of a waveguide grating, a silicon-based on-chip LC-WBG was designed, fabricated and evaluated. The fabricated LC-WBG was measured to have a time delay of 228 ps and a bandwidth of 11 nm. By incorporating two LC-WBGs in two arms of an MZI structure, an on-chip optical spectral shaper with a linearly-varying FSR was produced. Applying the spectral shaper in a photonic microwave waveform generation system based on SS-WTT mapping, an LCMW with a large TBWP was experimentally generated. By using a spectral shaper with the length of the offset waveguide equal to zero, an LCMW having a symmetrical chirp profile was generated. The positive and negative chirp rates were, respectively, 5.4 GHz/ns and -4.9 GHz/ns, and the TBWP is 359.7. By using a spectral shaper with the length of the offset waveguide equal to the length of the LC-WBG, an LCMW having a uniform chirp profile was generated. The chirp rate was 1.54 GHz/ns and the TBWP was 615. This is the largest TBWP ever reported based on SS-WTT mapping

technique, to the best of our knowledge. In addition, by varying the center wavelength of the input optical pulse, the central frequency of the generated LCMW was tuned. However, the main disadvantage of the LC-WBG and the spectral shaper is the untunable optical properties. Once the devices are fabricated, the optical properties are fixed, which heavily hinders from a wide application.

CHAPTER 6 SILICON-BASED ON-CHIP ELECTRICALLY TUNABLE LINEARLY CHIRPED WAVEGUIDE BRAGG GRATING

In this chapter, to enable a linearly chirped waveguide Bragg grating (LC-WBG) could be electrically tuned, a lateral PN junction is introduced in the grating and thus an electrically tunable LC-WBG is realized. By incorporating two tunable LC-WBGs in a Michelson interferometer structure, an electrically tunable optical spectral shaper is made. By applying the fabricated spectral shaper in a photonic microwave arbitrary waveform generation system based on spectral shaping and wavelength-to-time mapping, a continuously tunable linearly chirped microwave waveform (LCMW) is experimentally generated.

6.1 Electrically tunable linearly chirped waveguide Bragg grating

Since a tunable optical delay line is highly preferred for practical applications, to overcome the problem of untunable optical properties in the passive LC-WBG discussed in Chapter 5.1, we proposed a silicon-based on-chip electrically-tunable LC-WBG. In the passive LC-WBG, the grating was formed on a rib waveguide in which periodic corrugations were introduced to the sidewalls of the slab waveguide and the chirp was achieved by linearly increasing the rib width along the gratings. To use the plasma dispersion effect in silicon to realize electrical tunability, however, the corrugations have to be moved to the sidewalls of the rib waveguide.

6.1.1 Design of an electrically tunable LC-WBG

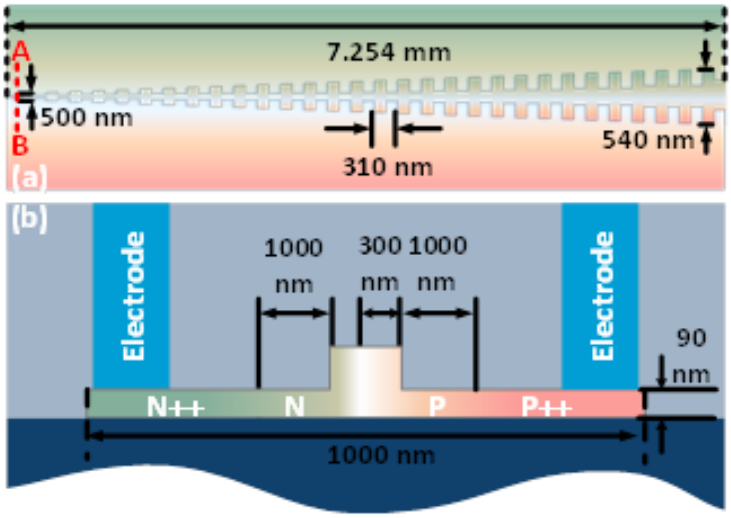

Fig. 6.1 (a) Top-view of the electrically-tunable LC-WBG and (b) cross-sectional view of the electrically-tunable LC-WBG along the line AB.

Fig. 6.1(a) presents the top view of the proposed electrically-tunable LC-WBG. To effectively suppress the sidelobes in the reflection spectral response, Gaussian apodization, a technique to tailor the grating spectral response to reduce the ripples, is applied to the grating, which is done by varying the corrugation depths in a raised Gaussian profile along the rib waveguide. To enable the grating to work in C band, the grating period is designed to be 310 nm with a duty cycle is 50%, corresponding to a Bragg wavelength of 1550 nm, and the rib width is increasing linearly from 500 to 540 nm. The total length of the grating is 7.254 mm with an expected time delay of 170 ps. Fig. 6.1(b) presents the cross-sectional view of the electrically-tunable LC-WBG along the line AB in Fig. 6.1(a). An asymmetrical lateral PN junction is employed, which is slightly shifted to the left from the center of the waveguide by 50 nm. Such a shift could increase the mode overlap with the p-type doping region to achieve a higher tuning efficiency, since the plasma dispersion effect is more sensitive to the change of the free-hole concentration. Additional p++ and n++ implantations,

1 μm away from the rib to minimize absorption losses, are utilized for ohmic contact formation. Two contact windows are opened on the silica pads, with a 2-μm-thick aluminum layer deposited to make the ohmic contacts. The proposed electrically-tunable LC-WBG is sent for fabrication using the CMOS-compatible process with 248-nm deep ultraviolet lithography at IME, Singapore.

6.1.2 Evaluation of an electrically tunable LC-WBG

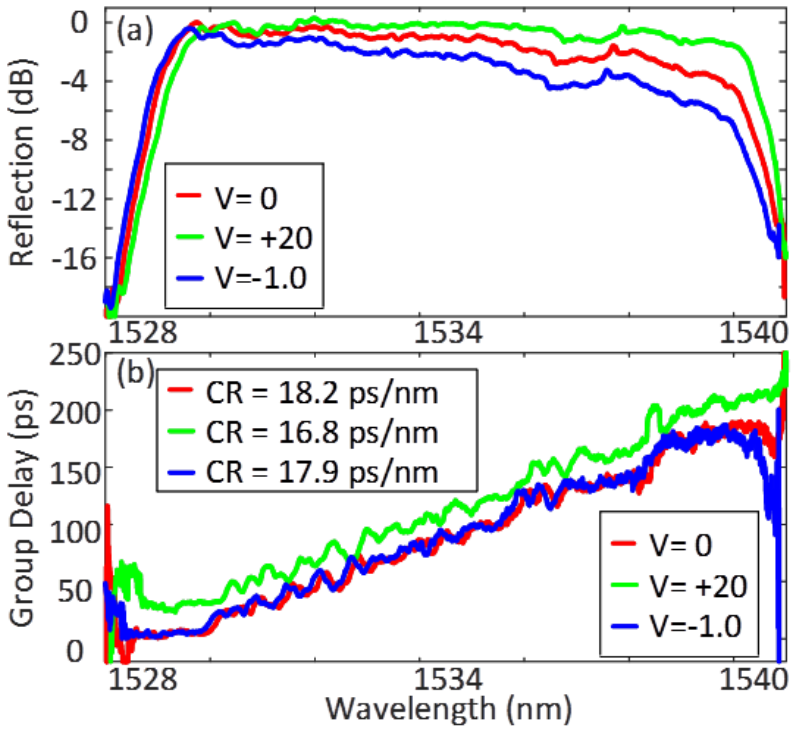

Fig. 6.2 (a) Measured spectral and (b) group delay responses of a fabricated electrically-tunable LC-WBG under the different bias voltages.

The optical performance of the fabricated electrically-tunable LC-WBG is evaluated using an optical vector analyzer (LUNA OVA CTe). Fig. 6.2(a) and (b) shows, respectively, the normalized reflection spectral and the group delay responses of the LC-WBG when biased

at 0 V, +20 V and -1.0 V. When the bias voltage is zero, as shown in Fig. 6.2(b) in red, the grating exhibits a time delay of 174.9 ps between 1529.14 and 1538.77 nm and thus has a dispersion value of 18.2 ps/nm and a chirp rate of 1.328 nm/mm. It is apparent to see from Fig. 6.2(a) that the grating has a comparatively large insertion loss at the longer wavelength. This is because the light wave with a longer wavelength needs to travel a longer distance in the LC-WBG until it is reflected at the right location of the LC-WBG, since the rib width is linearly increasing along the grating. The loss includes the grating-induced loss and the doping-induced loss. When the grating is forward biased at -1.0 V, as shown in Fig. 6.2(b) in blue, the grating exhibits a time delay of 124.10 ps between 1529.10 and 1536.00 nm and thus has a dispersion value of 17.9 ps/nm and a chirp rate of 0.951 nm/mm. It is worth noting that the spectrum is slightly blue-shifted compared to the spectrum when no bias voltage is applied. For forward biasing, when the bias voltage is increasing, the free-carrier injection would decrease the refractive index due to the plasma dispersion effect, which leads to a blue shift in the spectrum. In the meanwhile, the increased free-carrier density would also introduce an excess absorption loss. Therefore, the blue line exhibits a clearly changing insertion loss for different wavelengths. When the grating is reversed biased at +20 V, as shown in Fig. 6.2(b) in green, the grating exhibits a time delay of 182.27 ps between 1529.36 and 1540.24 nm and thus has a dispersion value of 16.8 ps/nm and a chirp rate of 1.500 nm/mm. Again a red-shift in the spectrum is observed. For reverse biasing, when the bias voltage is increasing, the free-carrier extraction would increase the refractive index via plasma dispersion effect, which leads to a red shift in the spectrum. Furthermore, since the free-carrier density is decreased, the doping-induced loss is decreased, which would alleviate the insertion loss difference for the light wave at different wavelengths. As can be found in

Fig. 6.2, the magnitude and group delay responses of the LC-WBG could be tuned by controlling the bias voltage, which is a potential solution to act as an electrically tunable optical delay line. Note that the ripples in the magnitude and the group delay responses are high, which are mainly caused by the fabrication limitations since the line width of the corrugations is smaller than the feature size. To reduce the ripples, advanced fabrication process should be used, in which the feature size should be smaller than the minimum line width of the LC-WBG. In addition, by applying an optimized apodization to the grating profile, the ripples could also be reduced. By incorporating the electrically tunable LC-WBGs in a Michelson interferometer structure, it is promising to realize an electrically-tunable optical spectral shaper, which could be applied in a photonic microwave arbitrary waveform generation system based on spectral shaping and wavelength-to-time (SS-WTT) mapping for tunable linearly chirped microwave waveform (LCMW) generation.

6.2 Its application in photonic generation of tunable linearly chirped microwave waveform

An LCMW with a large time bandwidth product (TBWP) is widely used in modern radar systems to enhance the range resolution. To provide a better resolution, an LCMW with a central frequency up to tens or even hundreds of gigahertz and a bandwidth of a few gigahertzes is required. In addition, with the development of multifunctional radar systems, more stringent requirements are imposed on the microwave waveforms. For example, it is desired that the central frequency or the chirp rate of an LCMW can be tuned to maximize the performance of a radar system. Therefore, the tuning of an LCMW is practically needed. Among the numerous techniques for photonic-assisted microwave waveform generation, SS-

WTT mapping is considered a technique with good simplicity and flexibility, and has been extensively researched. In an SS-WTT system, the tuning of the generated microwave waveform is done by changing the spectral response of the spectral shaper, which can be implemented by using a tunable optical filter serving as the spectral shaper.

A fiber interferometer is an optical filter which was employed as a spectral shaper in [142] to demonstrate the tuning in the central frequency and chirp rate of an LCMW. By tuning the dispersion unbalance or the relative delay between the two arms of the interferometer, the spectral response with tunable free-spectral range (FSR) was achieved, which led to the generation of an LCMW with a tunable chirp rate or a tunable central frequency. An LCMW with a central frequency ranging from 100 MHz to 25 GHz and a chirp rate ranging from -160 MHz/ns to +160 MHz/ns was experimentally generated. However, the TBWP of the generated microwave pulse is quite small, which is ~12. This small TBWP is due to the narrow bandwidth of the linearly chirped fiber Bragg grating (LC-FBG) used to perform WTT mapping, which limits the entire bandwidth of the SS-WTT system. In addition, the tuning of the central frequency was done by changing the length difference between the two arms in the interferometer using a tunable delay line. To simplify the frequency tuning, we proposed to use an optically pumped LC-FBG written in an erbium–ytterbium co-doped fiber. By incorporating such an LC-FBG in one arm of the interferometer, the central frequency of the generated LCMW can be tuned through optical pumping [143]. Again, the TBWP of the generated LCMW is small, which is ~24.5. The small TBWP is again due to the small bandwidth of the optically pumped LC-FBG. In [144], instead of using an optically pumped LC-FBG, a reconfigurable pulse shaper with a much wider bandwidth was incorporated in one arm of a fiber interferometer, an LCMW with a large TBWP of 589 was experimentally

generated. However, all the approaches reported in [142-144] were implemented based on fiber optics, which makes the system a large size and a poor stability. To overcome the inherent disadvantages of a fiber-optics based system, it is desirable that a waveform generation system is implemented based on photonic integrated circuits. For example, a chip-level optical spectral shaper was proposed and demonstrated for LCMW generation [87]. The spectral shaper was implemented based on a silicon chip consisting of multiple cascaded microring resonators. By thermally tuning the microring resonators, the spectral response of the spectral shaper was changed, which led to the change in the generated LCMW. In the experimental demonstration, an LCMW with a central frequency of 8 GHz and a TBWP of ~12 was demonstrated. Due to the limited thermal-tuning range, the generated LCMW has a small chirp rate, which led to a small bandwidth as well as a small TBWP.

6.2.1 Design of an optical spectral shaper

To generate a tunable LCMW with a high TBWP, we study the incorporation of the electrically tunable LC-WBGs in a Michelson interferometer structure to produce an electrically tunable spectral shaper. Fig. 6.3 illustrates the perspective view of the proposed electrically-tunable spectral shaper, and the inset shows the fundamental waveguide structures of a strip waveguide and a rib waveguide used in the spectral shaper. To minimize the chip footprint, the strip waveguide is used to guide the light, while the rib waveguide is employed for the LC-WBG where a lateral PN junction is made to achieve electrical tunability. To ensure a single transverse-electric (TE) mode operation, the strip waveguide is designed to have a width of 500 nm and a height of 220 nm, and the rib waveguide is designed to have a width of 500 nm, a height of 220 nm, and a slab thickness of 90 nm. Since the

structures of the two waveguides are different, a double-layer linear taper waveguide is required to achieve the mode transition between the two waveguides.

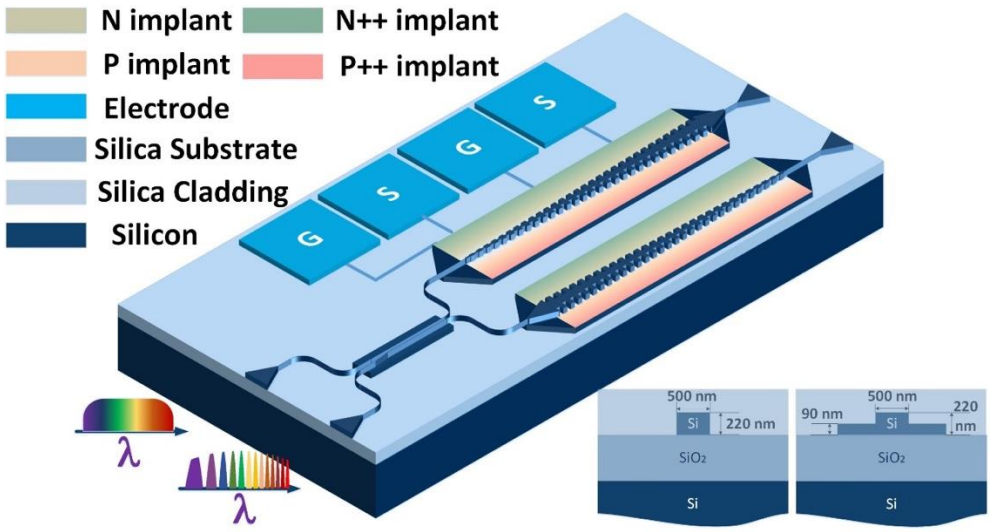

Fig. 6.3 Perspective view of the proposed silicon-based on-chip electrically-tunable optical spectral shaper.

Fig. 6.4(a) presents the schematic layout of an electrically-tunable spectral shaper, which has a Michelson interferometer structure consisting of a directional coupler and a pair of electrically-tunable LC-WBGs with independent bias contacts. A TE-mode grating coupler is used to couple the light into the chip through port 1 of the directional coupler. After the directional coupler, the input light is equally split and the split light waves are sent to the LC-WBGs with complementary chirp rates. The spectral components of the light waves at different wavelengths are reflected from different positions along the LC-WBGs and are recombined at directional coupler. Using another grating coupler, the combined light wave is coupled out of the chip. Thanks to the wavelength-dependent length difference between the two arms of the interferometer, the spectral shaper exhibits a wavelength-dependent FSR, which is required for the generation of an LCMW based on the SS-WTT mapping. In order

to realize independently electrical tuning of each of the LC-WBGs, two pairs of the bias contacts are designed and implemented. Note that at the right end of each of the LC-WBGs, a grating coupler is used as a waveguide terminator to avoid unwanted reflections. To achieve the mode transition between a strip waveguide and a rib waveguide, a taper with a length of 50 μm is added before and after the LC-WBGs.

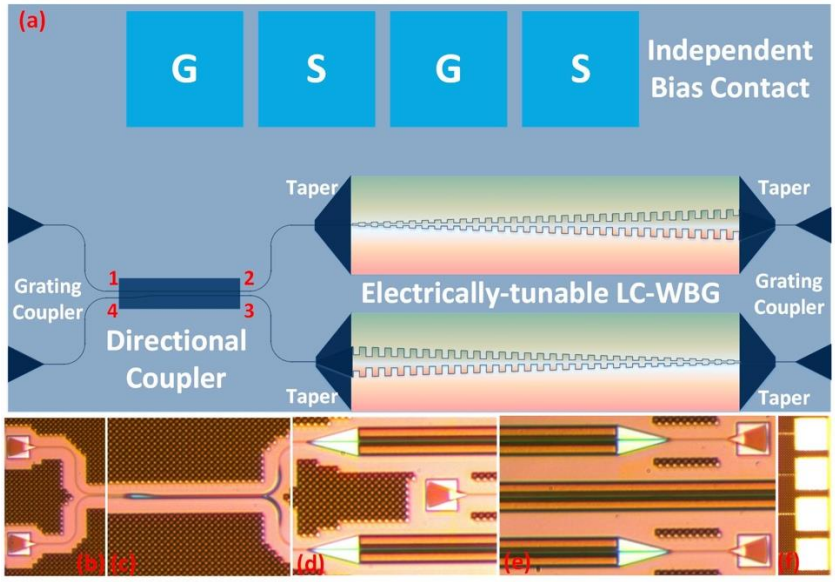

Fig. 6.4 (a) Schematic layout of the designed electrically-tunable spectral shaper; (b) photograph of the input and output grating couplers; (c) photograph of the 2×2 adiabatic 3-dB directional coupler; (d) photograph of the front of the LC-WBGs; (e) photograph of the end of the LC-WBGs; (f) photograph of the two pairs of the bias contacts in the fabricated electrically-tunable spectral shaper.

The proposed electrically-tunable spectral shaper is sent for fabrication using the CMOS-compatible process with 248-nm deep ultraviolet lithography at IME, Singapore. Fig. 6.4(b) is a photograph of the input and output grating couplers for light coupling between the fiber and the chip in the fabricated spectral shaper, captured by a microscope camera. Their center-to-center spacing is 127 μm, which matches the spacing of the fiber array used for the

experiment. Fig. 6.4(c) is a photograph of the 2×2 adiabatic 3-dB directional coupler. Fig. 6.4(d) is a photograph of the front the LC-WBGs, and Fig. 6.4(e) is a photograph of the end of the LC-WBGs. Note that the tapers are also shown in the two photographs in Fig. 6.4(d) and 4(e), and the grating coupler as a terminator is shown in Fig. 6.4(e). Fig. 6.4(f) shows a photograph of the two pairs of the bias contacts. A contact has a dimension of 80×80 (μm×μm) and the center-to-center spacing between two contacts is 100 μm.

6.2.2 Evaluation of an optical spectral shaper

The optical performance of the fabricated electrically-tunable spectral shaper is evaluated. In the fabricated spectral shaper, two identical electrically-tunable LC-WBGs with complementary chirp rates are incorporated in the two arms of an interferometer. The total length of the LC-WBG is designed to be 7.0 mm. In the LC-WBG, the rib width is linearly increasing from 500 to 540 nm and Gaussian apodization is employed by varying the corrugation depth in a raised Gaussian profile along the grating. The entire electrically-tunable spectral shaper has a size of 7.10 mm in length and 0.016 mm in width, giving a small footprint of 0.114 mm^2. Fig. 6.5(a) shows the measured spectral response of the fabricated spectral shaper when no bias voltage is applied. Since the spectral shaper has a symmetric configuration, the spectral response presents a symmetrically varying FSR. Note that the measured spectral response in Fig. 6.5(a) is slightly asymmetrical, which is caused by the Gaussian apodization applied to the grating.

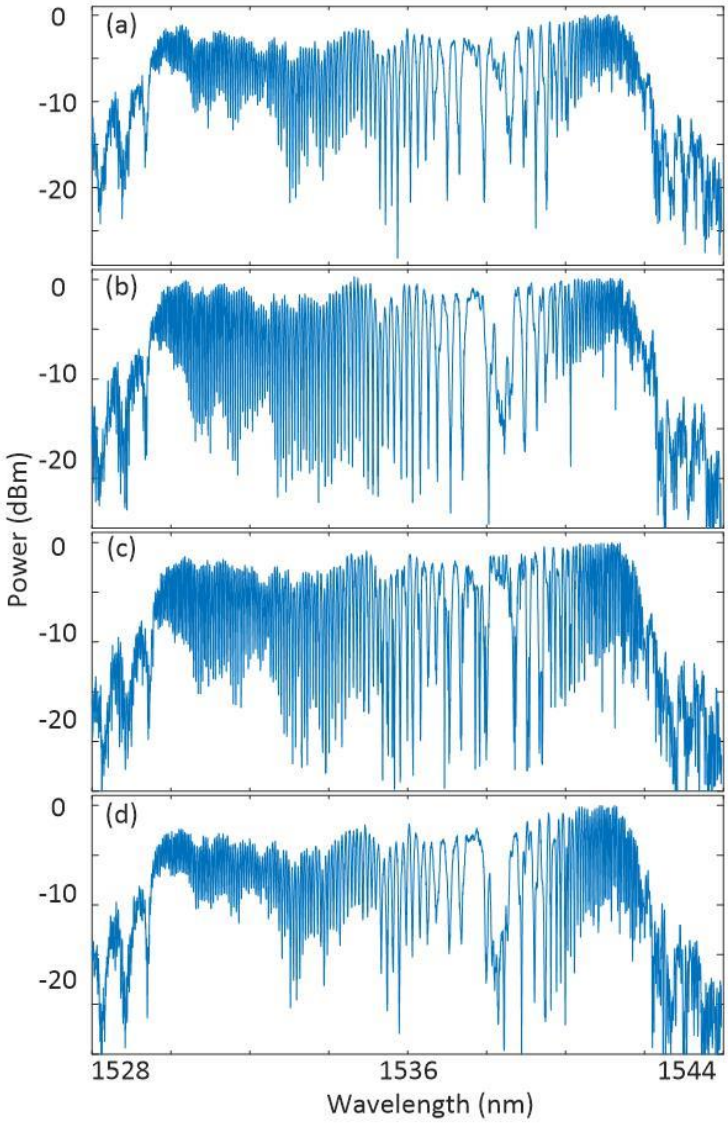

Fig. 6.5 Measured spectral responses of the fabricated spectral shaper when (a) no bias voltage is applied; (b) a reverse-biased voltage of +20 V is applied to the LC-WBG in the upper arm; (c) two identical reverse-biased voltages of +20 V are applied to the LC-WBGs in both arms; (d) a reverse-biased voltage of +20 V is applied to the LC-WBG in the upper arm while a forward-biased voltage of -1.0 V is applied to the LC-WBG in the lower arm.

Fig. 6.5(b) shows a measured spectral response of the fabricated spectral shaper when a reverse-biased voltage of +20 V is applied to the LC-WBG in the upper arm. Since there is

no bias voltage applied to the LC-WBG in the lower arm, its reflection spectrum is kept unchanged, while the spectrum of the LC-WBG in the upper arm when reverse biased would be red-shifted, which would finally lead to a change in the spectral response of the spectral shaper.

Fig. 6.5(c) shows the measured spectral response of the fabricated spectral shaper when two identical reverse-biased voltages of +20 V are applied to the LC-WBGs in both arms. Since the spectrums of the two LC-WBGs are both red-shifted, there would be a double change in the spectral response of the spectral shaper.

Fig. 6.5(d) shows the spectrum of the spectral shaper when a reverse-biased voltage of +20V is applied to the LC-WBG in the upper arm and a forward-biased voltage of -1.0 V is applied to the LC-WBG in the lower arm. The spectrum of the LC-WBG in the upper arm is red-shifted, and that of the LC-WBG in the lower arm is blue-shifted, which would cause a change in the spectral response of the spectral shaper. As can be seen in Fig. 6.5, by independently tuning bias voltages applied to the two LC-WBGs, the spectral shaper would exhibit tunable spectral response, which would lead to the generation of a tunable LCMW. Note that the insertion loss of the fabricated spectral shaper is measured to be around 24 dB, which is mainly resulted from the fiber-to-fiber coupling loss and the splitting loss of the directional coupler.

6.2.3 Theoretical principle of photonic generation of tunable LCMW based on SS-WTT mapping

The fundamental principle is identical to the one discussed in 5.3.3 except the chirp rates of the two LC-WBGs in our proposed spectral shaper could be independently tuned by applying a bias voltage, which enables the system to have a largely flexible tunability.

Based on the analysis discussed in 5.3.3, the instantaneous microwave carrier frequency of the generated microwave waveform can be expressed as:

$$f_{RF}(\delta t) = \frac{2}{\lambda_0^2}\frac{n_{eff\,0}\Delta L_0}{\ddot{\Phi}_\lambda} + \frac{2}{\lambda_0^2}\frac{n_{eff\,1}\delta t}{C_1\ddot{\Phi}_\lambda^2} - \frac{2}{\lambda_0^2}\frac{n_{eff\,2}\delta t}{C_2\ddot{\Phi}_\lambda^2} \tag{6-1}$$

where λ_0 is the center wavelength of the input optical pulse, δt (nm) is the time detuning from the center of the temporal waveform, C_1 (nm/mm) and C_2 (nm/mm) are the chirp rates of the LC-WBGs in the upper and lower arms, respectively, $n_{eff\,1}$ and $n_{eff\,2}$ are the average effective refractive indices of the LC-WBGs in the upper and lower arms, respectively, $\ddot{\Phi}_\lambda$ is the group velocity dispersion (GVD) of the dispersive element, and ΔL_0 is the length difference between the two arms of the spectral shaper. Since the proposed spectral shaper has a symmetrical configuration, ΔL_0 is equal to zero. For the two LC-FBGs have complementary chirp rates, C_1 is positive and C_2 is negative. Then, the equation could be rewritten as:

$$f_{RF}(\delta t) = \frac{2}{\lambda_0^2}\frac{n_{eff\,1}\delta t}{C_1\ddot{\Phi}_\lambda^2} - \frac{2}{\lambda_0^2}\frac{n_{eff\,2}\delta t}{C_2\ddot{\Phi}_\lambda^2} \tag{6-2}$$

which shows that the instantaneous microwave frequency of the generated microwave waveform is linear with time and dependent on the chirp rates of the two LC-WBGs for a given dispersive element for WTT mapping. Thanks to the electrical tunability of the LC-

WBGs in the spectral shaper, the instantaneous microwave frequency of the generated microwave waveform could be tuned by tuning the bias voltages to the LC-WBGs.

In addition, according to (6-2), for a dispersive element with a given dispersion, the central frequency of the generated chirped microwave waveform is zero when $\delta t = 0$ and is independent of the chirp rates of the LC-WBGs. When the chirp rate of an LC-WBG or the chirp rates of the two LC-WBGs are varied by changing the applied bias voltages, the central frequency of the generated chirped microwave waveform is still kept zero. To have a non-zero central frequency, an offset waveguide can be added in one arm to introduce a length difference between the two arms. With the different length difference between the two arms, the central frequency of the generated chirped microwave waveform could be different.

The chirp rate of the generated microwave waveform is given by:

$$CR = \frac{df_{RF}(\delta t)}{dt} = \frac{2}{\lambda_0^2}\frac{n_{eff\,1}}{C_1\ddot{\Phi}_\lambda^2} - \frac{2}{\lambda_0^2}\frac{n_{eff\,2}}{C_2\ddot{\Phi}_\lambda^2} \tag{6-3}$$

which is determined by the chirp rates of the two LC-WBGs for a dispersive element with a given dispersion. Again, the chirp rate of the generated microwave waveform could be tuned by tuning the applied bias voltages to the LC-WBGs.

The pulse compression ratio is determined by the TBWP of the generated microwave waveform. In our system, the TBWP of the generated chirped microwave pulse is calculated by:

$$TBWP = CR \cdot \Delta T^2 = (\frac{2}{\lambda_0^2}\frac{n_{eff\,1}}{C_1} - \frac{2}{\lambda_0^2}\frac{n_{eff\,2}}{C_2})B_\lambda^2 \tag{6-4}$$

where B_λ is the spectral width of the input optical pulse since the bandwidth of the spectral shaper is broader than the spectral width of the optical pulse. It can be found that the TBWP is independent of the dispersion of the dispersive element but determined by the chirp rates of the LC-WBGs and the spectral width of the input optical pulse. For a given input optical pulse with the spectral width of B_λ, by varying the bias voltages to the LC-WBGs, the chirp rates are changed, which leads to a change in the TBWP. Compared with a fiber-based spectral shaper, our proposed spectral shaper has a comparatively large spectral bandwidth, thanks to the strong index modulation in the LC-WBGs, which enables the system to generate an LCMW generation with a comparatively large TBWP.

6.2.4 Experimental results

An experiment is performed. Fig. 6.6(a) shows the experimental setup. An optical Gaussian pulse train from a mode-lock laser (MLL) (Pritel 1550-nm Picosecond and Femtosecond Fiber Lasers) with a pulse duration of approximately 600 fs, a spectral width of 8 nm, and a repetition rate of 40 MHz, is launched into the on-chip spectral shaper via a polarization controller (PC). The PC is used to adjust the state of polarization (SOP) of the input optical pulse to minimize the polarization-dependent loss. At the output of the spectral shaper, a spectrally-shaped optical pulse is generated, which is amplified by an EDFA and then sent to a DCF with a GVD of -1020 ps/nm serving as a dispersive element to perform WTT mapping. The optical waveform at the output of the DCF is applied to a PD (NewFocus Model 1014, 45 GHz bandwidth). An LCMW is generated at the output of the PD, which is monitored using a sampling oscilloscope (OSC, Agilent 86116A, 63 GHz bandwidth). Two independent bias voltages from a power supply are applied to the two LC-WBGs to achieve

waveform tuning. Fig. 6.6(b) is a photograph captured by a camera which presents a fiber array for the light coupling into and out of the chip and a pair of electrical probes for the bias voltages.

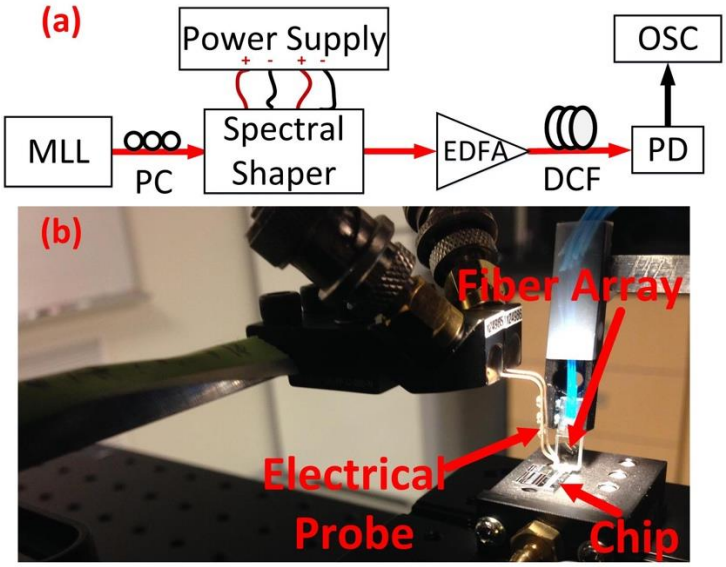

Fig. 6.6 (a). Experimental setup. MML: mode lock laser. PC: polarization controller. EDFA: erbium-doped fiber amplifier. DCF: dispersion compensating fiber. PD: photodetector. OSC: oscilloscope. (b) Image of the fiber array and electrical probe applied on the chip captured by a camera.

An experiment is performed to generate a tunable LCMW using the fabricated electrically-tunable spectral shaper. First, two bias voltages are kept zero. Fig. 6.7(a) shows the temporal waveform of the generated LCMW. As can be seen, the generated LCMW has a temporal duration of around 7.95 ns. Fig. 6.7(b) presents its spectrogram that exhibits a symmetrical chirp profile, which matches the spectral response of the fabricated spectral shaper. Its central frequency is 0.80 GHz, which is slightly different from the theoretical value of 0 GHz. This non-zero value is resulted from a small asymmetry between the two arms of the spectral shaper induced by fabrication imperfections. On the right side of the center, the instantaneous

frequency is linearly increasing with a positive chirp rate of 2.96 GHz/ns, which agrees well with a theoretical value of 3.21GHz/ns by (6-2). On the left side of the center, the instantaneous frequency is linearly decreasing with a negative chirp rate of -6.25 GHz/ns. The difference in the chirp rate is due to the asymmetry of the two LC-WBGs in the two arms of the MZI, which is caused by Gaussian apodization. From the time-domain waveform and its carrier frequency distribution, the TBWP of the generated LCMW is estimated to be around 133.8. Fig. 6.7(c) shows a compressed pulse with a pulse width of 40 ps, which is obtained by calculating the autocorrelation of the generated microwave waveform. Note that the direct-current component in the generated LCMW is removed before calculating the autocorrelation. By comparing the pulse width of the waveforms in Fig. 6.7(a) and 7(c), a pulse compression ratio as large as 198.8 is obtained.

Second, a bias voltage of +20V is applied to the LC-WBG in the upper arm only. Fig. 6.8(a) shows the temporal waveform of the generated LCMW. As can be seen, the generated LCMW has a temporal duration of around 9.15 ns. Fig. 6.8(b) presents its spectrogram which exhibits a symmetrical chirp profile. Its central frequency is 0.14 GHz, closer to a theoretical value of 0 GHz. On the right side of the center, the instantaneous frequency is linearly increasing with a positive chirp rate of 2.68 GHz/ns. On the left side of the center, the instantaneous frequency is linearly decreasing with a negative chirp rate of -6.10 GHz/ns. Smaller chirp rates are expected based on (6-3). A larger chirp rate of a LC-WBG, a smaller chirp rate of a generated LCMW. Since the LC-WBG is reverse biased, its chirp rate is increased, which leads to the decrease in the chirp rate of the generated LCMW. Based on Fig. 6.8(b), the TBWP of the generated LCMW is estimated to be around 125.0. According to (6-4), a smaller chirp rate of the LC-WBG results in a greater TBWP of the generated

LCMW. Fig. 6.8(c) shows the compressed pulse with a pulse width of 42 ps. By comparing the temporal widths of the waveforms in Fig. 6.8(a) and (c), a pulse compression ratio as large as 181.9 is obtained.

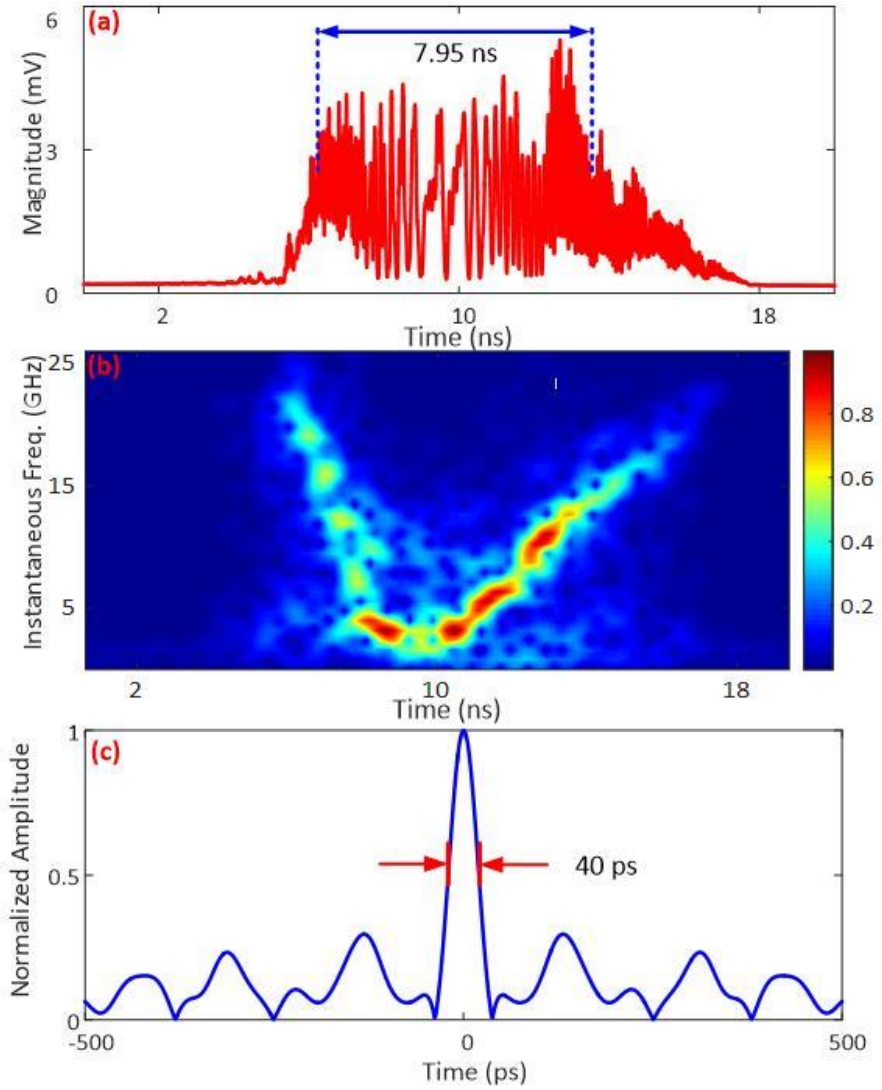

Fig. 6.7 Experimental results: (a) the generated LCMW; (b) the spectrogram and instantaneous frequency of the generated LCMW, and (c) the compressed pulse by autocorrelation.

Then, two identical biased voltages of +20 V are applied to the LC-WBGs in both arms. Fig. 6. 9(a) shows the temporal waveform of the generated LCMW. As can be seen, the generated

LCMW has a temporal duration of around 8.57 ns. Fig. 6.9(b) presents its spectrogram which exhibits a symmetrical chirp profile and a central frequency of 0.73 GHz. On the right side of the center, the instantaneous frequency is linearly increasing with a positive chirp rate of 2.51 GHz/ns, and on the left side of the center, the instantaneous frequency is linearly decreasing with a negative chirp rate of -5.84 GHz/ns. The TBWP of the generated LCMW is estimated to be around 95.54. Fig. 6.9(c) shows the compressed pulse with a pulse width of 48 ps, and a pulse compression ratio as large as 141.8 is obtained. Since the both LC-WBGs are reverse biased, their chirp rates are both increased, which leads to a smallest chirp rate of the generated LCMW and a smallest TBWP.

Finally, a reverse biased voltage of +20V is applied to the LC-WBG in the upper arm and a forward biased voltage of -1.0 V is applied to the LC-WBG in the lower arm. Fig. 6.10(a) shows the temporal waveform of the generated LCMW. As can be seen, the generated LCMW has a temporal duration of around 9.05 ns. Fig. 6.10(b) presents its spectrogram which exhibits a symmetrical chirp profile and a central frequency of 0.79 GHz. On the right side of the center, the instantaneous frequency is linearly increasing with a positive chirp rate of 2.82 GHz/ns. On the left side of the center, the instantaneous frequency is linearly decreasing with a negative chirp rate of -6.05 GHz/ns. The TBWP of the generated LCMW is estimated to be around 142.6. Fig. 6.10(c) shows the compressed pulse with a pulse width of 45 ps, and a pulse compression ratio as large as 191.0 is obtained. The LC-WBG with a forward biased voltage has a smaller chirp rate, which counteracts the result caused by the LC-WBG with a reverse biased voltage.

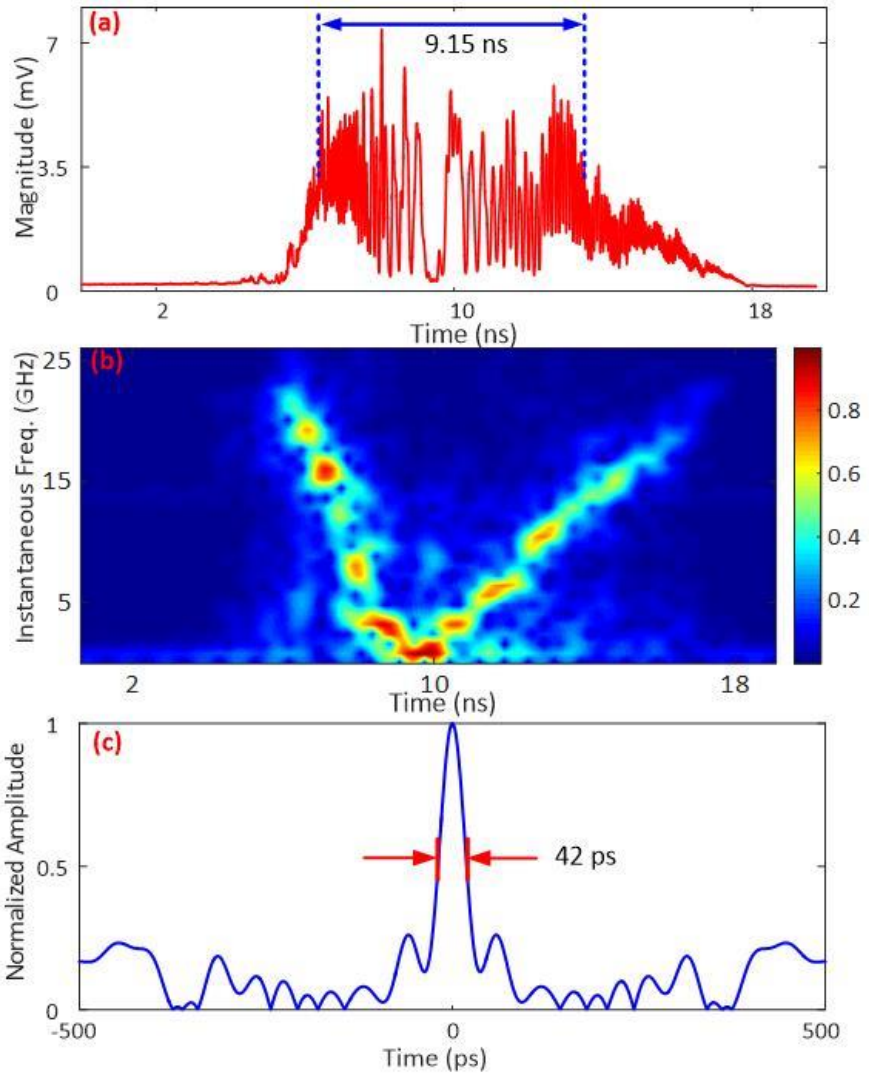

Fig. 6.8 Experimental results: (a) the generated LCMW; (b) the spectrogram and instantaneous frequency of the generated LCMW, and (c) the compressed pulse by autocorrelation.

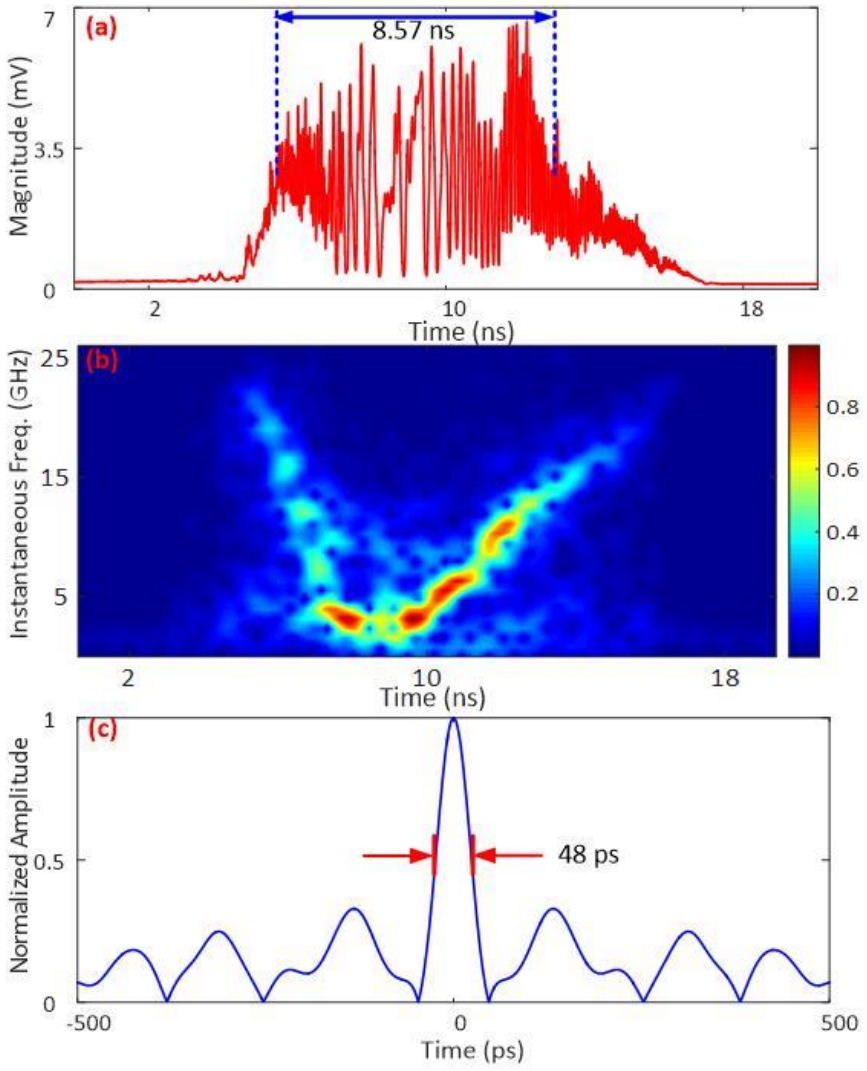

Fig. 6.9 Experimental results: (a) the generated LCMW; (b) the spectrogram and instantaneous frequency of the generated LCMW, and (c) the compressed pulse by autocorrelation.

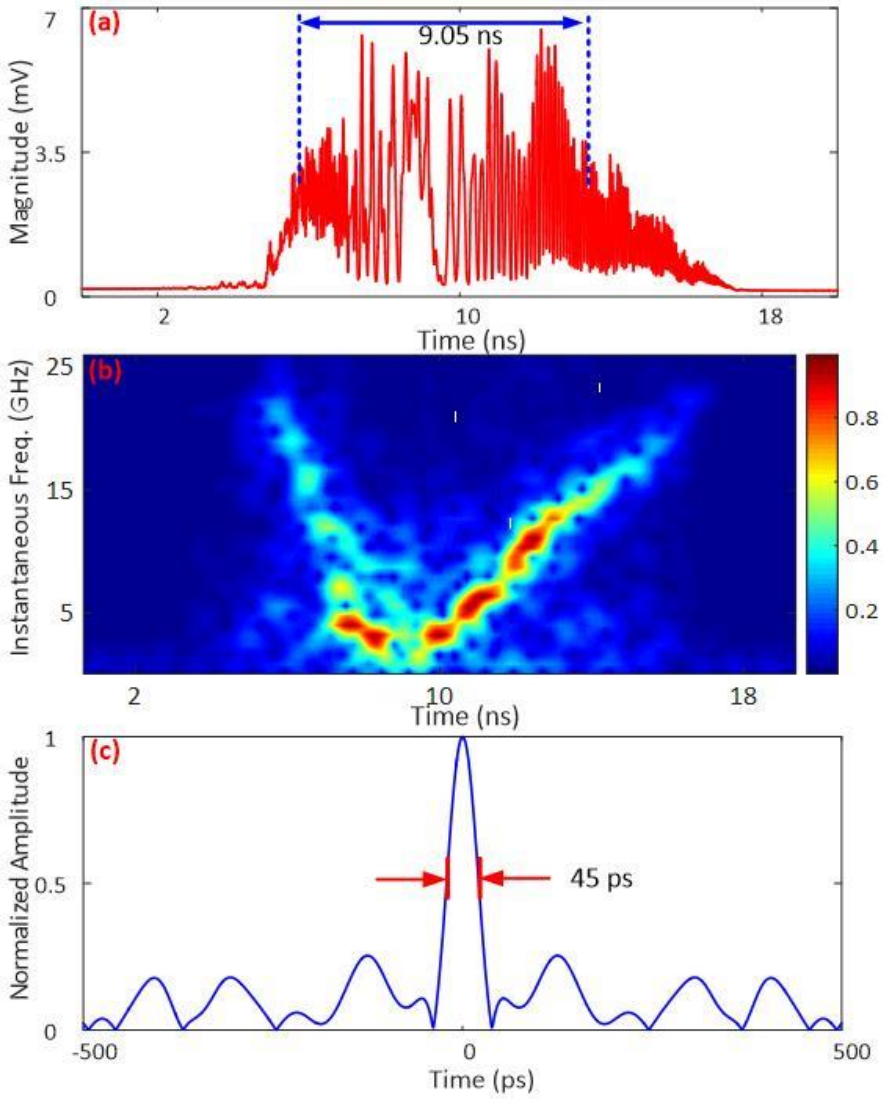

Fig. 6.10 Experimental results: (a) the generated LCMW; (b) the spectrogram and instantaneous frequency of the generated LCMW, and (c) the compressed pulse by autocorrelation.

If two identical bias voltages of -1.0 V are applied to the two LC-WBGs, due to an increase in the insertion losses induced by the increased free-carrier density, the optical performance of the spectral shaper is heavily degraded. Although only four bias voltage pairs are selected in the experiment to generate four chirped microwave waveforms, the results can be extended to generate any chirped microwave waveform when the bias voltages are continuously tuned.

In addition, in the proposed electrically-tunable spectral shaper, a symmetrical interferometer structure is employed, which leads to the generated LCMW to have a symmetrical chirp profile in its spectral response and a zero frequency in the center of the generated LCMW. It is convenient to add an offset waveguide in one of the arms to introduce a non-zero length difference between the two arms, which could result in a monotonous chirp profile and a nonzero frequency in the generated LCMW. Furthermore, significant sidelobes are observed in the compressed pulses. In theory, a linearly chirped microwave pulse with a rectangular spectral profile would lead to a Sinc-type compressed pulse [145]. For our generated linearly chirped microwave pulses, they have an approximately rectangular spectral profile. This is the reason why the sidelobes are large after compression. By modifying the spectrum of an LCMW to have a bell-shaped profile, the sidelobes could be reduced. This can be done by optimizing the apodization profile in the grating.

6.3 Conclusion

In conclusion, to enable an LC-WBG could be electrically tuned, a lateral PN junction was introduced in the grating and thus an electrically tunable LC-WBG was realized. By incorporating two tunable LC-WBGs in a Michelson interferometer structure, an electrically tunable optical spectral shaper was made. By applying the fabricated spectral shaper in a photonic microwave arbitrary waveform generation system based on SS-WTT mapping, a continuously tunable LCMW was experimentally generated. The chirp rate of the generated LCMW could be continuously tuned by tuning the bias voltages on the two LC-WBGs. The key advantage of using the spectral shaper for LCMW generation is the ultra-fast electrical

tunability of the generated LCMW due to the ultra-fast free-carrier plasma dispersion effect in a scale of nanoseconds.

CHAPTER 7 SILICON-BASED ON-CHIP MICRORING RESONATOR

Compared with a waveguide Bragg grating device, an on-chip optical micro-cavity resonator usually has a much smaller dimension, which is of help to increase integration density and reduce the power consumption. As the most common class of optical micro-cavity resonator, microring resonators (MRRs) have been extensively researched. In this chapter, we propose an on-chip symmetric Mach-Zehnder interferometer (MZI) structure incorporating multiple cascaded MRRs. By specifically designing the radii of the rings, the interferometer could be designed to have a spectral response with a linearly-varying free spectral range (FSR), which could be used in photonic chirped microwave waveform generation based on spectral shaping and wavelength-to-time (SS-WTT) mapping, and to have a multi-channel spectral response with identical channel spacing, which could be used in the implementation of an independently tunable multi-channel fractional-order temporal differentiator.

7.1 Its application in photonic generation of chirped microwave waveform

Recently, a silicon-based optical spectral shaper consisting of multiple cascaded MRRs was proposed [87]. By thermally tuning the rings, a spectral shaper with an increasing or decreasing free spectral range (FSR) could be obtained. By applying the spectral shaper in an SS-WTT mapping system, the generation of a chirped microwave waveform with a central frequency of 8 GHz was experimentally demonstrated. However, due to the limited thermal-

tuning range, the time-bandwidth product (TBWP) and the chirp rate of the generated chirped microwave waveform are limited.

7.1.1 Design of an optical spectral shaper

To generate a chirped microwave waveform with a large chirp rate, we propose a silicon-based on-chip optical spectral shaper, which has an MZI structure in which multiple MRRs are cascaded. By controlling the radii of the micro-rings, the spectral response of the spectral shaper can be controlled to have a largely increasing or decreasing FSR.

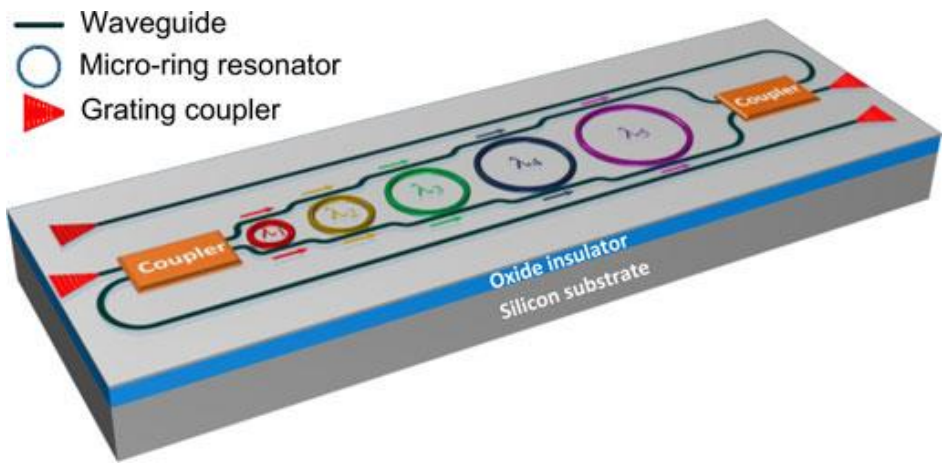

Fig. 7.1 Perspective view of the proposed on-chip spectral shaper.

Fig. 7.1 shows the perspective view of the spectral shaper. It has an MZI structure incorporating multiple cascaded MRRs. The MZI comprises two adiabatic 3-dB couplers [146]. To minimize the chip footprint and to reduce the bending loss, a strip waveguide is used to guide the light. A grating coupler is employed to couple the light into and out of the chip. Fig. 7.2 illustrates the layout of the proposed silicon-based on-chip spectral shaper. The input light is split by the first adiabatic 3-dB coupler into two beams that travel through the

upper and lower arms. Each ring will selectively transfer the optical power at its resonance wavelength from the through-port waveguide to its drop-port waveguide. The rings are shown in different colors, to indicate that each ring is designed to have a different radius and therefore a different resonant wavelength. The spacing between the neighbour rings is large enough to avoid mutual interferences. In the upper and lower waveguides, S-shape waveguide bends, which are designed using Bezier curves to minimize the mode mismatch and thus reduce the waveguide bending loss, are added to adapt to the change of the rings. The resonant wavelengths from the both waveguides will be recombined at the first adiabatic 3-dB coupler and constructively interfere as reflected signals. The non-resonant wavelengths are recombined at the second adiabatic 3-dB coupler at the transmission port. In order to achieve a maximum reflection power, each ring is designed to work in the critical coupling condition. By carefully designing the ring radii, at the reflection port, the reflection peaks with a linearly increasing spacing can be achieved. Thus, the spectral shaper can be used in an SS-WTT mapping system for microwave waveform generation. Note that in Fig. 1, for measurement convenience, the reflection port has its independent grating coupler. The proposed optical spectral shaper is sent for fabrication using a CMOS compatible process with 193-nm deep ultraviolet lithography at IMEC, Belgium, accessed via ePIXfab.

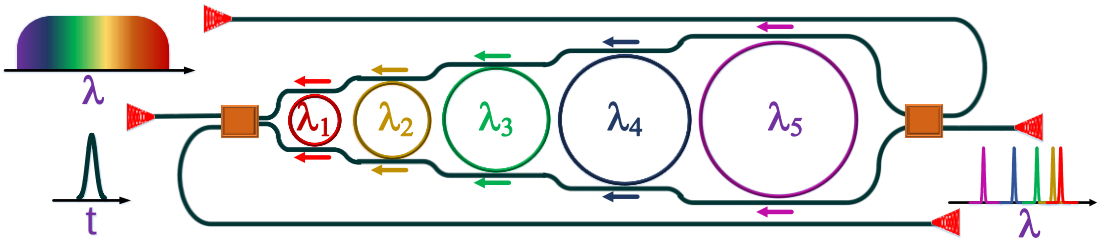

Fig. 7.2 Schematic layout of the designed on-chip spectral shaper.

7.1.2 Evaluation of an optical spectral shaper

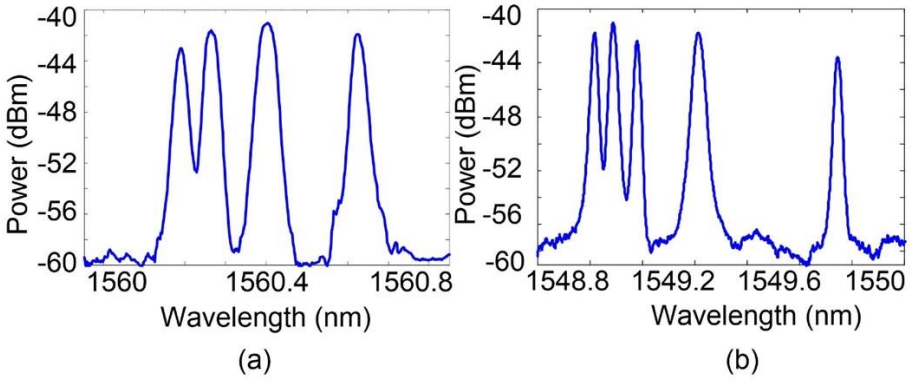

Fig. 7.3 (a) Measured spectral response of an on-chip spectral shaper consisting four cascaded MRRs; (b) measured spectral response of an on-chip spectral shaper consisting five cascaded MRRs.

The optical performance of the fabricated spectral shaper is evaluated. The spectral responses are measured using an optical vector analyzer (LUNA OVA CTe). Fig. 7.3(a) shows the spectral response at the reflection port of an on-chip spectral shaper consisting of four ring resonators with the radii of 20.172, 20.684, 21.196, and 21.710 μm. To simplify the design, the coupling gaps are kept identical of 200 nm. Fig. 7.3(b) shows the spectral response of an on-chip spectral shaper consisting of five ring resonators with the radii of 20.132, 20.644, 21.156, 21.670 and 22.186 μm. Again, to simplify the design, the coupling gaps are kept identical of 200 nm. As can be seen, the spacing between the neighbouring peaks is linearly increasing.

7.1.3 Experimental results of chirped microwave waveform generation

Fig. 7.4 shows the experimental setup incorporating the two fabricated spectral shapers for chirped microwave waveform generation. An optical pulse is generated by a tunable mode

lock laser (Pritel 1550-nm Picosecond and Femtosecond Fiber Lasers) which has approximately a pulse duration of 600 fs and a repetition rate of 40 MHz. The optical pulse is sent to an EDFA through an isolator to increase the power. A polarization controller (PC) is connected between the EDFA and the spectral shaper to adjust the state of polarization (SOP) of the input signal to minimize the polarization-dependent loss. After spectral shaping by a spectral shaper, a spectral-shaped optical pulse is obtained which is first amplified using a second EDFA and then sent to a dispersion compensating fiber (DCF) to perform WTT mapping. The DCF has a first-order dispersion coefficient of -948 ps/nm. The WTT mapping can be explained as follows: the linear chromatic dispersion would cause different frequency components to propagate at the different velocities. The ultrashort pulse envelope is therefore broadened, resulting in a time-domain profile that is a scaled version of the shaped spectrum. This is the process called WTT mapping. The optical intensity envelope is then converted to a microwave signal at a photodetector (PD, NewFocus Model 1414). The time-domain microwave signal is measured using a sampling oscilloscope (Infiniium 86100C).

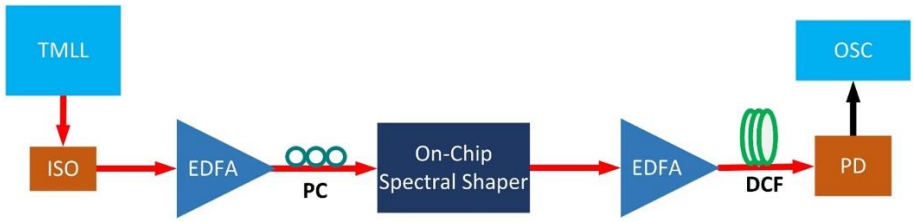

Fig. 7.4 Experimental setup. TMML: tunable mode lock laser. ISO: Isolator; EDFA: erbium-doped fiber amplifier. PC: polarization controller. DCF: dispersion compensation fiber. PD: photodetector. OSC: oscilloscope.

Fig. 7.5 shows the chirped microwave waveform generated based on the four-ring spectral shaper shown in Fig. 7.3(a). Fig. 7.5(b) shows the spectrogram, which illustrates the time

distribution of the microwave frequency components. The colors indicate the relative spectral intensity of the frequency components. Low-frequency contents below 5 GHz are not shown in the spectrogram. As can be seen, the frequency of the generated microwave waveform has a bandwidth of 8.5 GHz and a chirp rate of 12.2 GHz/ns. Fig. 7.6 shows microwave waveform generated based on the five-ring pulse shaper shown in Fig. 7.3(b), and the spectrogram is shown in Fig. 7.6(b). As can be seen the frequency of the generated microwave waveform has a bandwidth of 15.5 GHz and a chirp rate of 17.2 GHz/ns. Small differences between the spectral response and its corresponding generated microwave waveform are observed, which are resulted mainly from the limited bandwidth of the PD. Due to the limited bandwidth of the PD, the high frequency components are attenuated. Note that the generated waveforms have a limited number of cycles. For practical applications, a chirped microwave waveform with a large number of cycles is needed. This can be done by simply adding more ring resonators in the MZI structure.

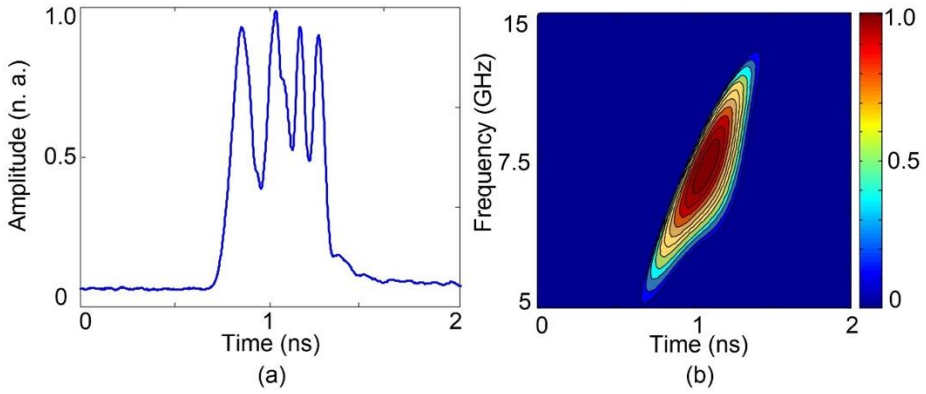

Fig. 7.5 (a) Generated chirped microwave waveform using a spectral shaper with four cascaded MRRs in the MZI structure; (b) the spectrogram of the chirped signal.

The key advantage of the proposed optical spectral shaper is the flexibility of the design and the configuration. In order to meet the requirement of a high chirped rate, the rings are designed to have largely different radii that are adapted by the two specially designed MZI arms, which also gives the convenience to expand to incorporate more rings. The spectral shaper based on this design has smaller size with better compactness. In addition, the spectral shaper works in the reflection mode. Thus, the reflection port and the input port can share a common grating coupler, which would further reduce the footprint. Furthermore, all the micro-ring resonators are embedded in the MZI, which makes the system more stable.

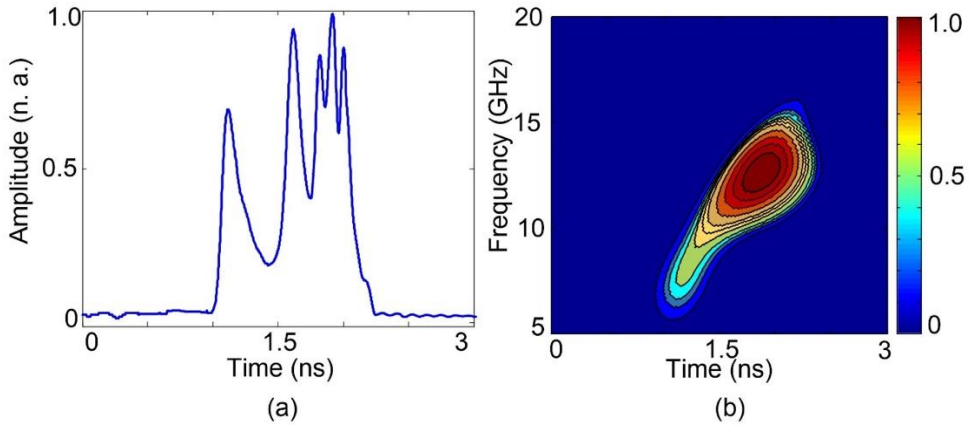

Fig. 7.6 (a) Generated chirped microwave waveform using a spectral shaper with five cascaded MRRs in the MZI structure; (b) the spectrogram of the chirped signal.

7.2 Its application in a multi-channel photonic temporal differentiator

With the fast growth of information exchange all over the world, wavelength-division multiplexing (WDM), as a promising technology for expanding the capacity for optical communications, has been widely used in the present optical communications networks [147]. For ultrafast signal processing and characterization in a WDM network, an all-optical temporal differentiator that is capable of performing temporal differentiation of multichannel

signals carried by multiple wavelengths is required. Different approaches have been demonstrated a multi-channel photonic temporal differentiator. For example, an optical interferometer is used to realize a multi-channel photonic temporal differentiator. The response of an interferometer is intrinsically periodic in frequency. This fact has been exploited for the measurement and characterization of multi-wavelength high-speed signals in a WDM communications system [148]. The main limitation of this solution is the poor stability due to the high sensitivity of an interferometer to environmental fluctuations. Another solution is to use a single multi-channel fiber Bragg grating (MC-FBG) [149]. A MC-FBG can be designed using the discrete layer peeling (DLP) algorithm together with the spatial sampling technique. However, in the both techniques, once the device is fabricated, the differentiation order is fixed.

7.2.1 Design of a multi-channel fractional-order photonic temporal differentiator

To make a multi-channel fractional-order temporal differentiator with independently tunable differentiation orders, we propose a symmetric MZI structure, in which multiple MRRs are cascaded. The proposed tunable multi-channel fractional-order temporal differentiator has the same configuration as the one discussed in Chapter 7.1.1 except that the radii of the rings are different. By carefully designing the radii of the multiple MRRs and the couplers, a multi-channel spectral response with identical channel spacing is obtained, which is used to implement a multi-channel fractional-order temporal differentiator. When a pump light is fed into an MRR, the phase response of the MRR is changed by tuning the power of the pump light thanks to the two-photon absorption (TPA) induced nonlinear effect in the MRR. Thus, the order of the temporal differentiator is tuned. A designed fiver-channel fractional-order

temporal differentiator is sent for fabrication using a CMOS-compatible technology with 193-nm optical projection lithography at IMEC, Belgium, accessed via ePIXfab. The waveguide consists of a thin silicon layer (220 nm thick) on top of a buried oxide layer (2 μm thick) on a silicon wafer. The strip waveguide is employed as the fundamental waveguide structure. In order to support single transverse-electric (TE) mode propagation, the strip waveguide width is chosen to be 500 nm. The radii of the five micro-ring resonator are designed to be 20.452, 20.964, 21.476, 21.990 and 22.506 μm so that the multi-channel response with identical channel spacing within the expected bandwidth is achieved. The coupling gaps between the MRRs and the two arms of the MZI are kept identical. Due to the propagation loss in the MRRs, the five add-drop MRRs would operate in the undercoupling regime. The entire device is 1.175 mm in length and 0.063 mm in width, giving a small footprint of 0.074 mm^2. The footprint of the device can still be greatly decreased if a compact Y-branch [150] is used to replace the adiabatic 3-dB coupler.

7.2.2 Evaluation of a multi-channel fractional-order photonic temporal differentiator

The optical performance of the fabricated multi-channel fractional-order temporal differentiator is evaluated. The spectral and phase responses are measured using an optical vector analyzer (LUNA OVA CTe). Fig. 7.7(a) shows the spectral response of the five-channel fractional-order temporal differentiator with a channel spacing of 0.49 nm measured at the transmission port. The phase response for each of the five channels is also shown in Fig. 7.7 as an insert. The FSRs of the MRRs are 4.383, 4.275, 4.154, 4.094 and 4.060 nm. Fig. 7.8 shows the zoom-in view of the spectral response for the third channel, which shows that the channel has a bandwidth of 0.032 nm or 4 GHz. Such a channel can be used for the

implementation of an optical differentiator with an operation bandwidth of 4 GHz. Based on the spectral response in Fig. 7.8, we can estimate the Q-factor of the MRR, which is about $4x10^5$. A high Q-factor ensures an MRR to have strong capacity in light confinement, which enables relatively low power pumping of the MRR to introduce the required phase response change. On the other hand, a high Q-factor makes an MRR to have a relatively small bandwidth. Thus, there is a trade-off between the operation bandwidth and the required pumping power.

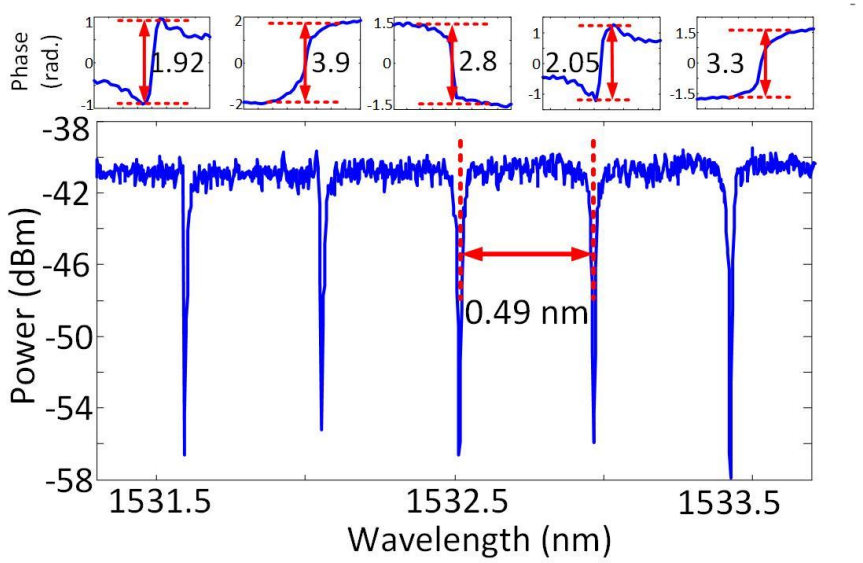

Fig. 7.7 Measured spectral response of the five-channel fractional-order temporal differentiator. Inset: measured phase response of the five-channel fractional-order temporal differentiator.

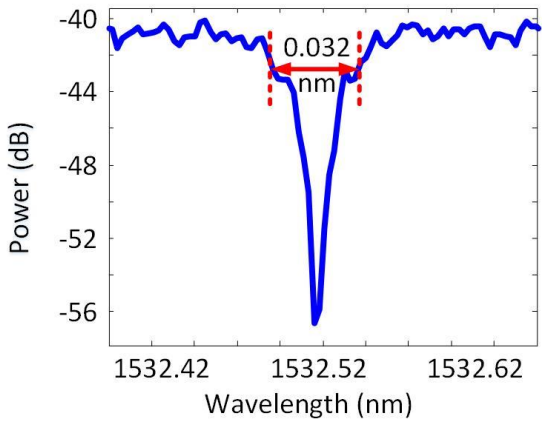

Fig. 7.8 Zoom-in view of spectral response of the third channel of the five-channel fractional-order temporal differentiator.

7.2.3 Experimental results of an optically tunable fractional-order differentiator

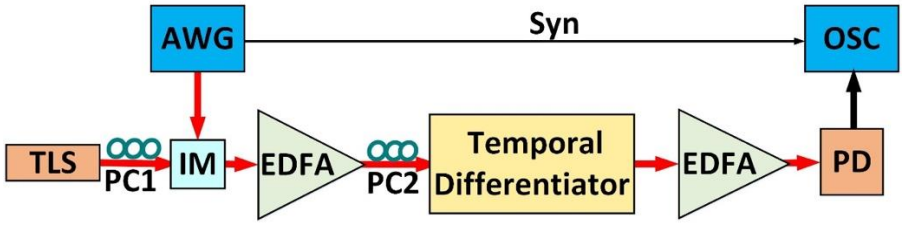

Fig. 7.9 Experimental setup. TLS: tunable laser source. IM: Intensity modulator; AWG: arbitrary waveform generator. EDFA: erbium-doped fiber amplifier. PC: polarization controller. PD: photodetector. OSC: oscilloscope.

To verify that the fabricated device can be used to implement a multi-channel temporal differentiator with independently tunable differentiation order, an experiment is carried out. The experimental setup is shown in Fig. 7.9. A continuous-wave (CW) light wave from a tunable laser source (TLS) is directed to an intensity modulator (IM) via a polarization

controller (PC1). An electrical pulse from an arbitrary waveform generator (AWG, Tektronix AWG7102) is applied to modulate the optical carrier at the IM. The pulse from the AWG has a shape close to a Gaussian with a temporal full-width at half-maximum of about 360 ps, or a spectral width of about 4 GHz, as shown in Fig. 7.10(a). The optical signal is then sent to the chip through a second polarization controller (PC2) which adjusts the state of polarization (SOP) of the input light wave to minimize the polarization-dependent loss. Since the central portion of the input signal spectrum is filtered out in the differentiator, the temporal differentiation is an operation with an inherently low energetic efficiency. To compensate for the loss, the optical signal is amplified before and after the temporal differentiator using two erbium-doped fiber amplifiers (EDFAs). Finally, the output optical pulse is detected by a high-speed photodetector (PD) with the waveform observed by a high-speed sampling oscilloscope (OSC, Agilent 86116A).

Fig. 7.10 shows the measured temporally differentiated pulses at the output of the five-channel fractional-order temporal differentiator for five optical wavelengths of 1531.564, 1532.006, 1532.460, 1532.948 and 1533.438 nm, for an input Gaussian pulse from the AWG, shown in Fig. 7.10(a) (blue-solid line). A simulated Gaussian pulse (red-dashed line) is also shown in Fig. 7.10(a) for comparison. Fig. 7.10(b) shows the corresponding temporally differentiated pulse (blue-solid line) by the first channel with a differentiation fraction order of 0.61. Again, a simulated temporally differentiated pulse (red-dashed line) is also shown for comparison. As can be seen the experimentally generated pulse is close to the simulated pulse, which confirms the effectiveness of the use of the device to perform fractional-order differentiation. Fig. 7.10(c)-(f) shows the temporally differentiated pulses by the other four channels, with differentiation orders of 1.24, 0.89, 0.65 and 1.05. Again, good agreement is

achieved, which confirms again the effectiveness of the use of the device to perform a fractional-order differentiation. Thus, the multi-channel operation of the fractional-order temporal differentiator has been demonstrated. The root mean square errors (RMSEs) of the five differentiators with fractional orders of 0.61, 1.24, 0.89, 0.65 and 1.05 are calculated, which are 2.0%, 3.4%, 3.2%, 2.2% and 3.2%, respectively

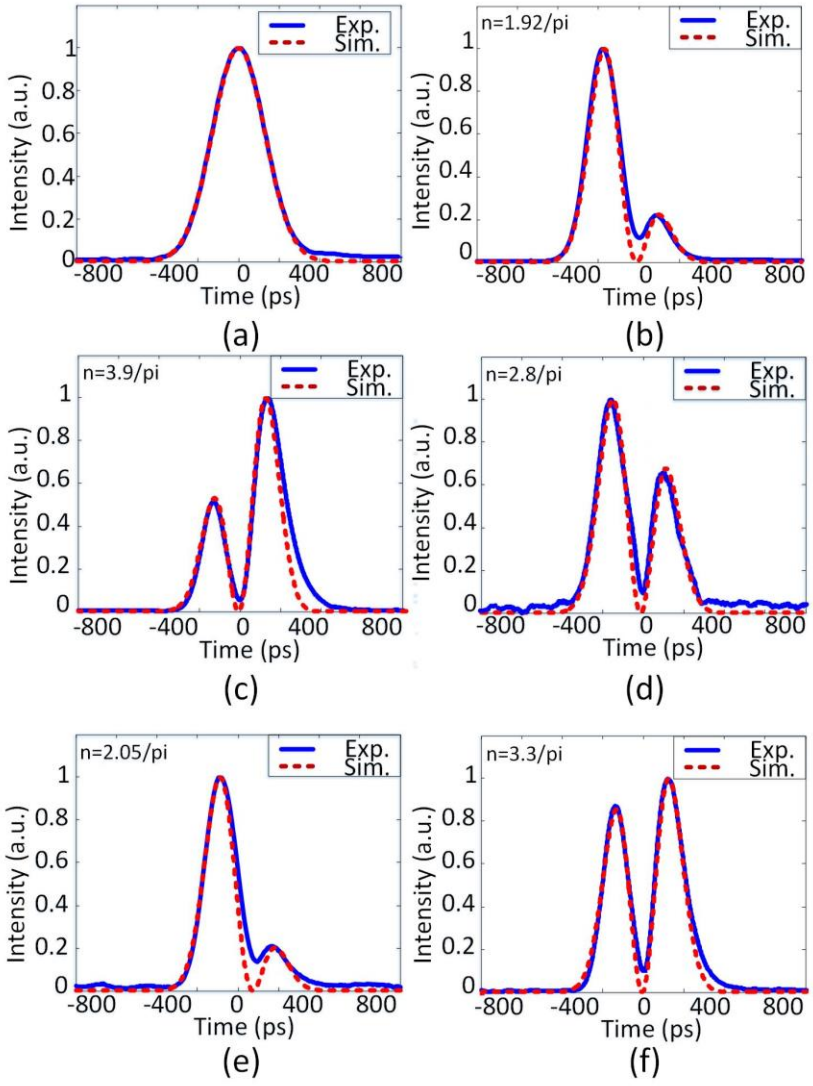

Fig. 7.10 Experimental results: (a) the measured Gaussian pulse from AWG (the blue solid line) and the simulated Gaussian pulse (the red dotted line); and measured differentiated output pulses from the photonic fractional differentiator at the (b) 1st, (c) 2nd, (d) 3rd, (e) 4th, and (f) 5th channel.

7.2.4 Experimental results of independent tunability of a multi-channel differentiator

We then demonstrate the independent differentiation order tunability. The experimental setup is shown in Fig. 7.11. The difference between the setup in Fig. 7.11 and that in Fig. 7.9 is that a wavelength-tunable light source is used as a pumping light to perform the differentiation order tuning.

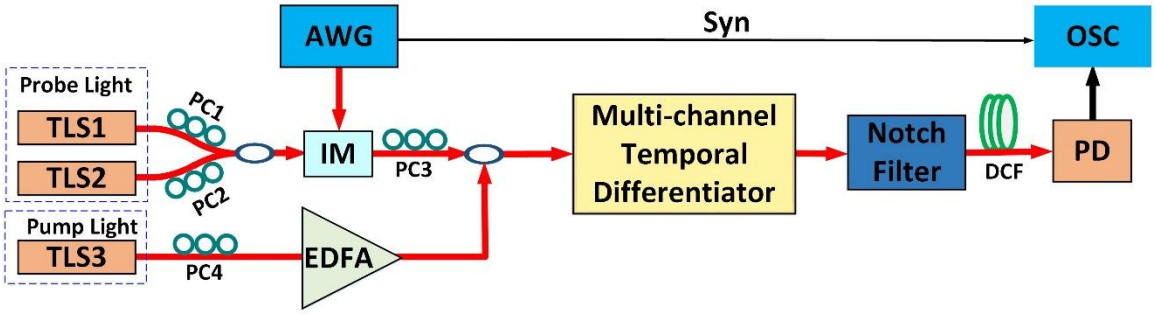

Fig. 7.11 Experimental setup. TLS: tunable laser source. IM: Intensity modulator; AWG: arbitrary waveform generator. EDFA: erbium-doped fiber amplifier. PC: polarization controller. PD: photodetector. OSC: oscilloscope. DCF: dispersion compensating fiber.

We first demonstrate the differentiation order tuning. In this case, only a single probe signal is applied to the chip. A pumping light is amplified by a high power EDFA (Amonics, AEDFA-33-B-FA) and sent to the chip together with the probe light via a coupler. The wavelength of the pumping light is selected different from the wavelength of the probe light, but is located at one resonant wavelength of the MRR to increase the light confinement, thus with increased nonlinear optical effect. At the output of the chip, a notch filter is used to remove the pumping light to avoid possible damage to the PD. The differentiated pulse is detected by the PD and the waveform is observed by the OSC. Thanks to the nonlinear

thermo-optic effect in the silicon-based MRR, when the pumping light at a different power level is fed into the MRR, the phase response of the MRR is changed [151, 152, 153]. The strong light-confinement nature of the MRR makes the MRR have a strong response to the nonlinear optical effect. Thus, the tuning is achieved at a low pumping power level. As it was demonstrated in [116], for the implementation of a temporal differentiator, the phase response is more important than the magnitude response. The magnitude response of an ideal temporal differentiator may not be exactly satisfied by using an MRR. The phase jump provided by an MRR is critical for the implementation of a temporal differentiator. When the phase jump is tuned by tuning the power of the pump light, a temporal differentiator with a tunable differentiation order is achieved.

Fig. 7.12 shows the measured differentiated pulses at the output of the second channel for a probe light at 1532.006 nm and a pumping light at 1536.280 nm. The pump light wavelength is selected at one resonance wavelength of the second MRR. Fig. 7.12(a) shows the measured phase response of the second channel with the pumping power increased from 0 to 31 dBm. As can be seen, with the increase of the pump light power, the phase jump becomes smaller, which is resulted from the increase in the internal loss in the MRR due to the TPA-induced nonlinear effect. Fig. 7.12(b)-12(f) show the corresponding temporally differentiated pulse (blue-solid line). Differentiated pulses with differentiation orders of 1.24, 1.13, 1.07, 1.00, and 0.97 are generated. The simulated pulses with an ideal input Gaussian pulse and an ideal differentiator with the same orders are also shown (red-dashed line) for comparison. As can be seen the experimentally generated pulses are close to the simulated pulses, which confirms the effectiveness of the use of the device to perform a tunable fractional-order differentiator.

The RMSEs of the differentiators with fractional orders of 1.24, 1.13, 1.07, 1.00 and 0.97 are also calculated, which are 3.4%, 3.6%, 3.8%, 3.0% and 2.4%, respectively.

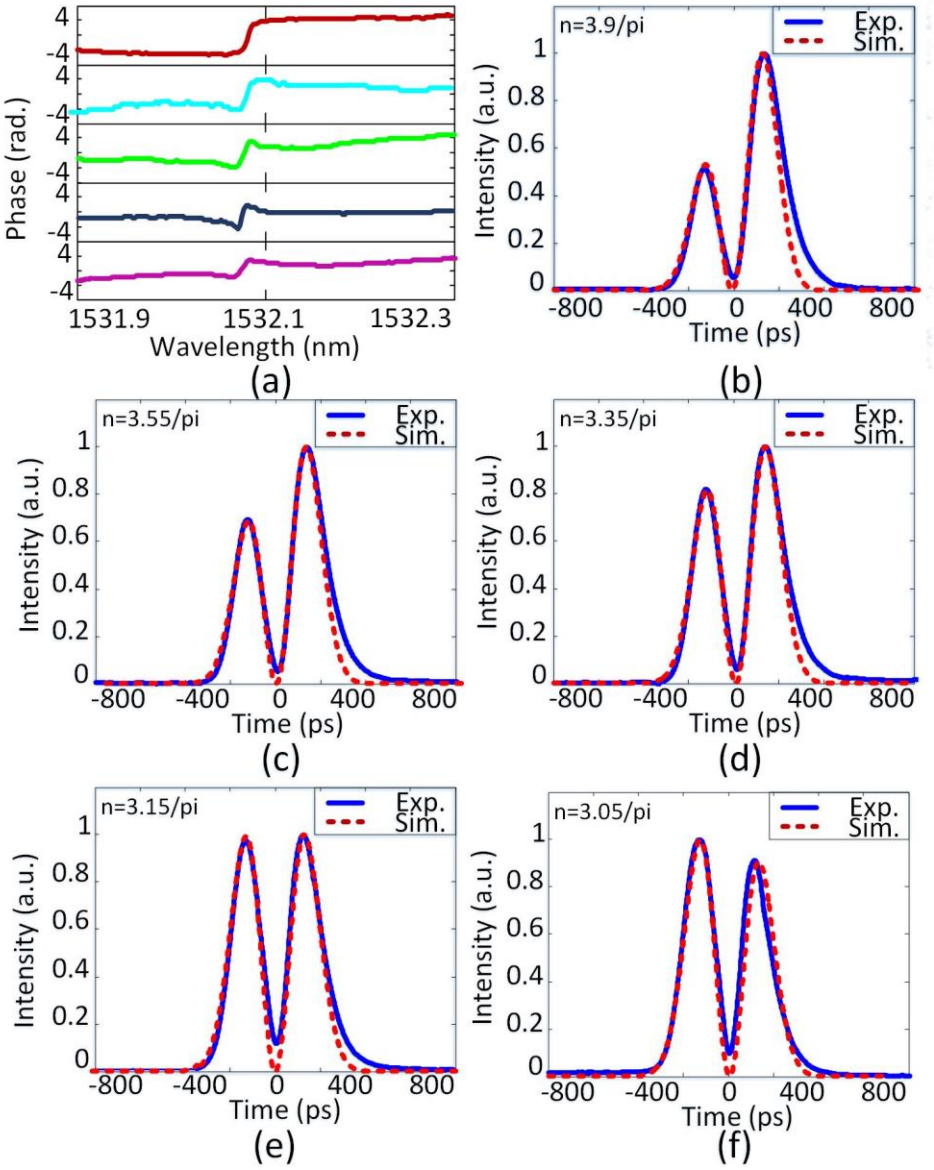

Fig. 7.12 Experimental results for differentiation order tuning: (a) measured phase response of the second channel with the power of the pump light increased, and measured differentiated output pulses from the photonic fractional differentiator at the second channel with the pump light wave power of (b) 0 dBm, (c) 21.7 dBm, (d) 25 dBm, (e) 28.7 dBm, and (f) 31 dBm.

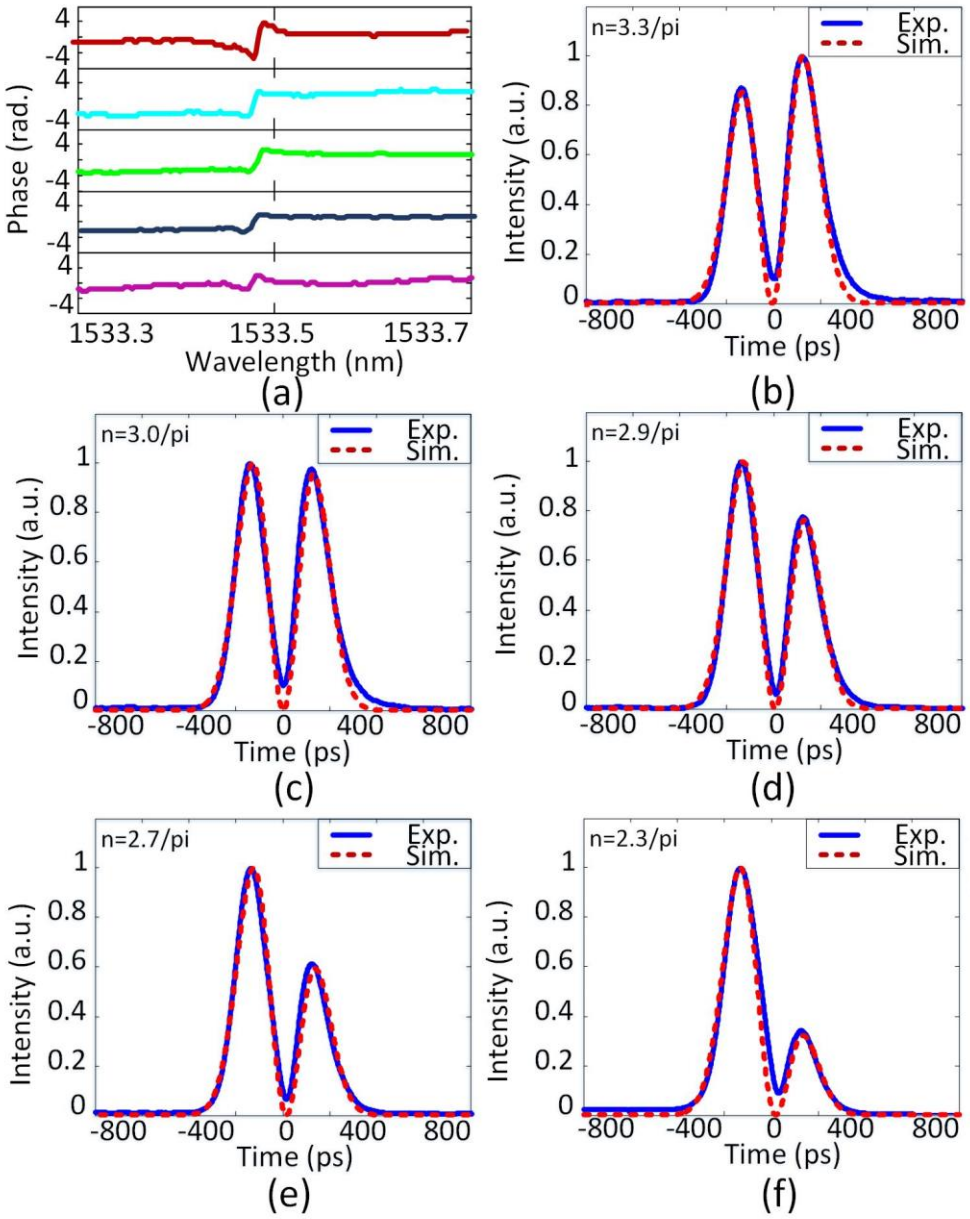

Fig. 7.13 Experimental results for differentiation order tuning: (a) Measured phase response of the second channel with the power of the pumping light increased, and the measured differentiated output pulses from the differentiator at the fifth channel with the pumping power at (b) 0 dBm, (c) 21.7 dBm, (d) 25 dBm, (e) 28.7 dBm, and (f) 31 dBm.

Fig. 7.13 shows the measured differentiated pulses at the output of the fifth channel for a probe light wavelength at 1533.438 nm and a pumping light wavelength at 1537.498 nm. The pumping light wavelength is selected at one resonance wavelength of the fifth MRR. Fig. 7.13(a) shows the measured phase response of the second channel with the pumping power increased from 0 to 31 dBm. Fig. 7.13(b)-13(f) show the corresponding temporally differentiated pulse (blue-solid line). Differentiated pulses with differentiation orders of 1.05, 0.96, 0.92, 0.86, and 0.73 are generated. The RMSEs of the differentiators with fractional orders of 1.05, 0.96, 0.92, 0.86 and 0.73 are again calculated, which are 3.2%, 3.2%, 2.6%, 2.2% and 2.1%, respectively. The experimental results in Fig. 7.12 and 13 confirm that the tuning of a sub-differentiator can be done by selecting the pumping wavelength.

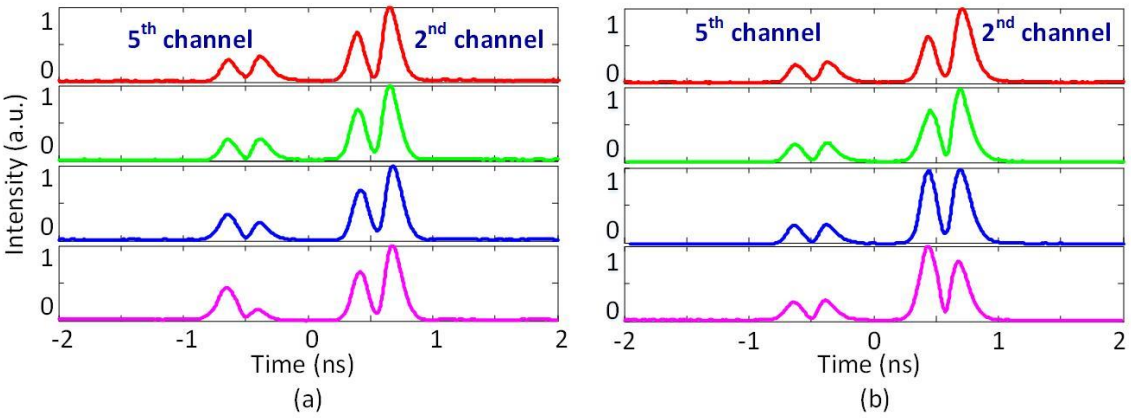

Fig. 7.14 Experimental results for independent tunability. Measured differentiated output pulses from the differentiator at the second and the fifth channels with the pumping light wavelength at (a) 1537.498 nm corresponding a resonant wavelength of the fifth channel, and (b) 1535.920 nm corresponding a resonant wavelength of the second channel.

Then, we verify that when one channel is pumped, the other channel is not affected. To do so, we send two probe light waves at two wavelengths at 1532.006 nm and 1533.438 nm

corresponding to two resonant wavelengths of the second and the fifth channels. A dispersion compensating fiber (DCF) is added to the setup in Fig. 7.11 to temporally separate the outputs from the two channels due to the dispersion-induced time delay between the two probe lights, for the purpose of waveform observation.

First, the wavelength of the pumping light is selected at one resonance wavelength of the fifth MRR. Fig. 7.14(a) shows the measured differentiated pulses at the output of the differentiator. The pulses on the left correspond to the output from the fifth channel and on the right correspond to the output from the second channel. The magnitude difference between the differentiated pulses from the two channels is resulted from the different amplitude resonance of the two channels. When the pumping wavelength is selected at 1537.498 nm corresponding a resonant wavelength of the fifth channel and the pumping power is increased from 0 to 31 dBm, the order of the differentiated pulse at the output fifth channel is changed while the order of the differentiated pulse at the second channel is maintained unchanged. Second, the wavelength of the pumping light is selected at one resonance wavelength of the second MRR. When the pumping wavelength is selected at 1535.920 nm corresponding a resonant wavelength of the second channel and the pumping power is increased from 0 to 31 dBm, the order of the differentiated pulse at the output of the second channel is changed while the order of the differentiated pulse at the fifth channel is maintained unchanged, shown in Fig. 7.14 (b). The experimental results in Fig. 7.14 confirm that the differentiation order of each sub-differentiator in the proposed integrated on-chip multi-channel differentiator is independently tuned.

The key feature of the proposed temporal differentiator is that a WDM signal at multiple wavelengths can be simultaneously differentiated and the fractional order of each individual

channel can be independently tuned, which gives much more flexibility in WDM signal processing.

7.3 Conclusion

In conclusion, a silicon-based on-chip symmetric MZI incorporating multiple cascaded MRRs was proposed, fabricated and evaluated. By controlling the radii of the rings, the interferometer could be designed to have a spectral response with a largely increasing or decreasing FSR. By using the interferometer as an optical spectral shaper in an SS-WTT mapping system, a largely chirped microwave waveform with a bandwidth of 15.55 GHz and a chirp rate of 17.2 GHz/ns was experimentally demonstrated. By controlling the radii of the rings, the interferometer was designed to have a multi-channel response with identical wavelength spacing, which was employed in the implementation of a multichannel fractional-order temporal differentiator. Thanks to the nonlinear thermo-optic effect induced by two-photon absorption, the phase response of the MRR could be changed by tuning the power of the pumping light at one resonant wavelength of the MRR. The use of the fabricated interferometer in the implementation of a five-channel temporal differentiator with independently tunable differentiation order was experimentally demonstrated.

CHAPTER 8 SILICON-BASED ON-CHIP MICRODISK RESONATOR

To further reduce the dimension of an on-chip micro-cavity resonator, a microdisk resonator (MDR) is a potential solution. Compared with a microring resonator (MRR) with two etched sidewalls, an MDR with a single sidewall exhibits attractive advantages of a more compact footprint and stronger light-confining capacity. However, in sharp contrast to widespread applications of the MRRs in microwave photonics, much less demonstrations have been reported to the use of MDRs in microwave photonic applications. In this chapter, we propose a silicon-based on-chip ultra-compact MDR with a single-mode operation and an ultra-high Q-factor, and the use of the fabricated MDR for the implementations of a microwave photonic filter and an optical delay line is experimentally demonstrated.

8.1 Ultra-compact microdisk resonator with a single-mode operation

Although an MDR exhibits better performance in terms of footprint and light-confining capacity over an MRR, compared with the widespread applications of an MRR, an MDR is much less used due to some inherent limitations. First, an MDR supports multiple whispering gallery modes (WGMs), which are not desired especially for filtering applications where the free spectral range (FSR) should be large to have a large finesse. Second, resonance-splitting exists in an MDR, which is resulted from the Rayleigh scattering induced by the sidewall roughness. Due to the resonance-splitting, the spectral response of an MDR with an ideal Lorentzian-shape is distorted, which is unwanted for filtering applications. Third, the

structure of an MDR is not compatible with that of a lateral PN junction. Therefore, it is challenging to achieve an electrically tunable MDR in which a lateral PN junction is essential. Although an electrically tunable MDR by incorporating an unusual vertical PN junction [154] or using a complicated disk configuration [155] has been reported, the structures are very complicated which would heavily increase the fabrication cost.

8.1.1 Design of an ultra-compact MDR

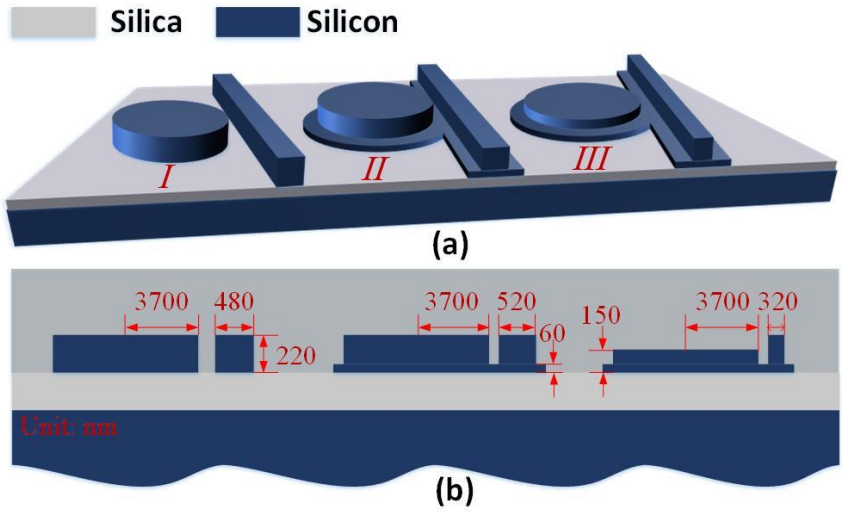

Fig. 8.1 (a) Perspective view of the three MDRs; (b) cross-sectional view of the three MDRs.

To overcome the problems of multi-WGMs operation and resonance-splitting, we propose a novel silicon-based on-chip ultra-compact MDR with a single-mode operation and ultra-high Q-factor. Fig. 8.1(a) illustrates the perspective view of the three MDRs, in which the Type-I disk is a conventional MDR, Type-II and Type-III disks are our proposed MDRs. In order to clearly illustrate the internal structure of the devices, the silica cladding layer is removed. Compared with the Type-I MDR, the distinct feature of our proposed Type-II MDR and Type-III MDR is that an additional slab waveguide is employed to wrap the disk and the

lateral sides of the bus waveguide, which aims to weaken the disk sidewall roughness impact on the confined optical field and strengthen the optical coupling between the disk and the bus waveguide. To ease the design, the widths of the slab waveguide around the disk and the bus waveguide keep identical, and in the coupling region the two slab waveguides fully overlap. Fig. 8.1(b) illustrates the cross-sectional view of the three MDRs. The three disks are designed to have an identical ultra-small radius of 3.7 μm, and the coupling gap is chosen to be 180 nm. The widths of the slab waveguides are kept identical to the width of the coupling gap. For the Type-I MDR, the height of the disk is 220 nm; for the Type-II MDR the disk has a height of 220 nm and the slab waveguide has a height of 60 nm; for the Type-III MDR the disk has a height of 150 nm and the slab waveguide has a height of 60 nm. It is worth noting that the bus waveguides in the three MDRs have an identical height of 220 nm but different widths which are specifically designed for each MDR to meet its phase-matching condition. Due to the multi-WGMs operation supported by an MDR, to effectively excite a specified WGM, the bus waveguide is designed to have a specific width to ensure that the effective index of the TE mode supported by the bus waveguide is equal to the effective index of the wanted WGM supported by the MDR. In the MDR, the effective index of the individual mode supported by the MDR can be calculated by

$$n_{eff} = \frac{m \cdot \lambda_0}{2\pi R} \tag{8-1}$$

where λ_0 is the resonance wavelength, m is azimuth harmonic number of the WGM, and R is the mode radius along the disk. After simulation using the finite difference time domain method, to effectively excite the fundamental WGM in each MDR, the widths of the three

bus waveguides for the Type-I, Type-II and Type-III MDRs are determined to be 480, 520, and 320 nm, respectively.

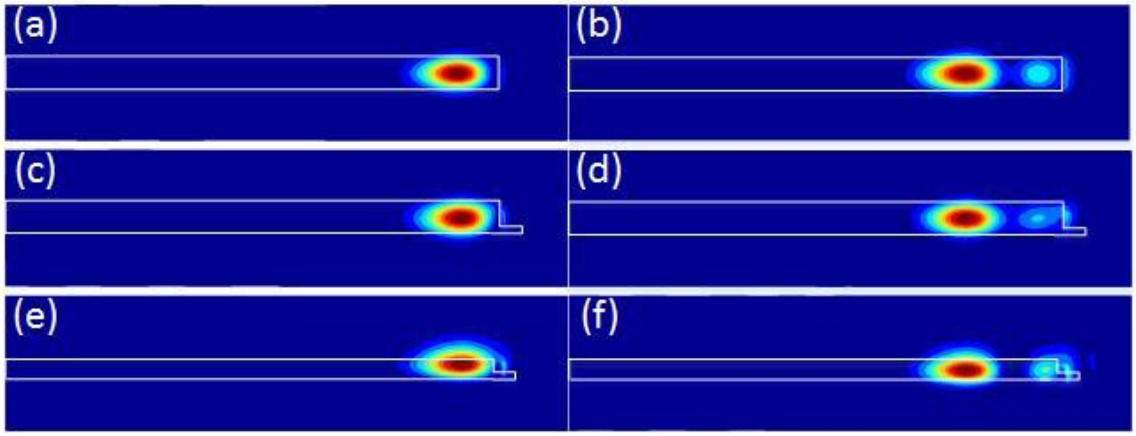

Fig. 8.2 Energy profiles of the fundamental (a) and first-order (b) radial TE mode in the Type-I MDR; of the fundamental (c) and first-order (d) radial TE mode in the Type-II MDR; and of the fundamental (e) and first-order (f) radial TE mode in the Type-III MDR

Fig. 8.2 shows the energy profiles of the fundamental and first-order radial TE modes supported by the MDRs with an identical radius of 3.7 μm. As can be seen, Fig. 8.2(a) shows the energy profile of the fundamental radial TE mode supported by Type-I conventional MDR. This mode energy decays rapidly in the radial direction and outside the disk region, which indicates a weak optical coupling of the disk to a laterally adjacent bus waveguide. In order to make the MDR work in critical coupling condition, such weak coupling often requires a very narrow coupling gap to increase the coupling strength, while the very narrow coupling gap would definitely increase the fabrication cost. In addition, compared with the first-order radial TE mode shown in Fig. 8.2(b), the fundamental radial TE mode has a comparatively smaller mode volume and a strong electric field next to the sidewall, and hence exhibits a higher sensitivity to the disk sidewall roughness, which finally results in a

high scattering loss and high occurrence possibility of resonance-splitting. Fig. 8.2(c) and 2(d) shows the first two orders of radial TE modes supported by the Type-II MDR. Compared with the ones in the Type-I conventional MDR, the energy profiles of fundamental and first-order TE modes supported by Type-II MDR exhibit a strong energy tail outside the disk, which is of great benefit to a strong optical coupling between the disk and the bus waveguide and hence a critical coupling. By carefully designing the bus waveguide width to make the fundamental TE mode support by the bus waveguide exactly meet the phase-matching condition with the fundamental WGM supported by the MDR, the fundamental WGM could be effectively excited in the disk thanks to the strong coupling, and the first-order WGM could be effectively suppressed since this mode has a tendency to couple into leaky modes. Thus, a single-mode operation of the MDR is enabled. In addition, owing to the slab waveguide wrapping the disk, part of the sidewall is further away from the confined mode, which could weaken the sidewall roughness impact on the optical field in terms of optical scattering. Fig. 8.2(e) and (f) shows the first two orders of radial TE modes supported by the Type-III MDR. It is clear to see that a lower height of the disk enables the supported TE modes to have a much stronger energy around the top surface of the disk. Since the spectral positions of the resonances are strongly dependent on the refractive index contrast between the resonator and its surrounding environment, such a strong energy distribution around the top surface makes this MDR to have a high potential for refractive index sensing such as label-free bio-sensing [156]. Again, a much stronger energy tail of the first-order mode shown in Fig. 8.2(f) would have a tendency to couple into a leaky mode to ensure a single-mode operation.

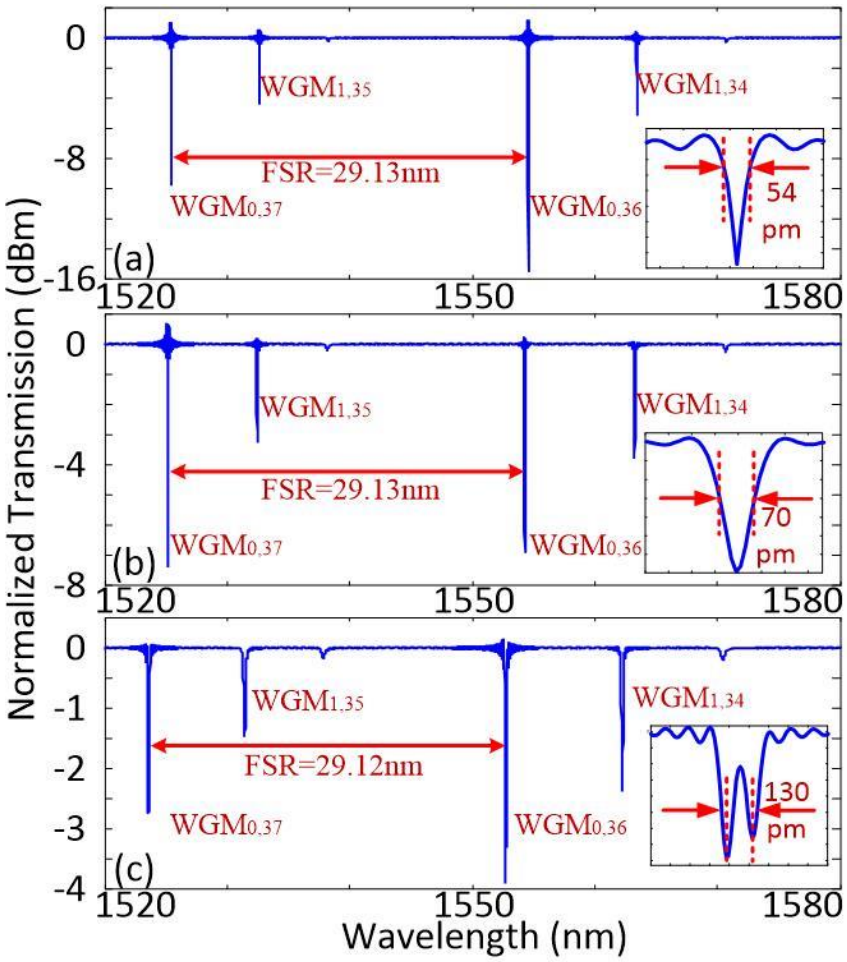

Fig. 8.3 Simulated transmission spectrums of the Type-I MDR with the magnitude of the sidewall roughness equal to (a) 0, (b) 10 and (c) 30 nm. The insets show the zoom-in view of the $WGM_{0,36}$ mode resonance.

Due to fabrication imperfections, sidewall roughness is always created, which has a negative impact on the optical performance of MDRs by scattering the confined optical waves. Firstly, a scattering loss is resulted, which would largely increase the propagation loss of the confined light circulating in the disk and then degrade the light-confining capacity of the disk. Secondly, the sidewall roughness scattering would also result in an optical coupling between the degenerate clockwise and counter-clockwise traveling modes, which would cause unwanted resonance-splitting [157, 158]. To verify the sidewall roughness impact on the

optical performance, a simulation is made in the conventional MDR. In the simulation set-up, the MDR has the same disk radius of 3.7 μm, bus waveguide width of 480 nm and coupling gap of 180 nm. Fig. 8.3 shows the simulated transmission spectrums of a conventional MDR when the disk sidewall roughness is gradually increased. The sidewall roughness is characterized statistically by the root-mean-square amplitude σ_r and the correlation length L_r. In the simulation, the correlation length L_r is set to be 20 nm while the amplitude of the roughness σ_r is gradually increased from 0 to 30 nm.

Fig. 8.3(a) shows the simulated transmission spectrum of the conventional MDR with zero roughness amplitude. Each notch in the spectrum represents a specific $WGM_{p,q}$ mode resonance in which p and q are the number of radial and azimuthal harmonic order, respectively. As can be seen, the first two orders of the WGMs are excited in the disk. The inset illustrates the zoom-in view of the $WGM_{0,36}$ mode resonance which has a 3-dB bandwidth of 54 pm. Note that the transmission magnitude at the resonance wavelength is higher than 0 dBm, which is due to the limited simulation time that causes the nonconvergence of the field at the resonance. When the roughness magnitude is increased to 10 nm, as shown in Fig. 8.3(b), again the first two orders of the WGMs are excited, while the 3-dB bandwidth of the $WGM_{0,36}$ mode resonance is increased into 70 pm, which indicates a decreased Q-factor of the disk. This is because the larger sidewall roughness would lead to a larger scattering loss suffered by the confined optical field. When the roughness magnitude continues to be increased to 30 nm, the first two orders of the WGMs are still excited, and the 3-dB bandwidth of the $WGM_{0,36}$ mode resonance is increased into 130 pm, which confirms again that the larger sidewall roughness, the larger scattering loss. More importantly, resonance-splitting happens, which is induced by an optical coupling between the degenerate

clockwise and counter-clockwise traveling modes as a result of a strong sidewall roughness scattering. The resonance-splitting distorts an ideal Lorentzian-shaped spectrum of the resonance, which is unwanted for most applications and especially does harm to the filtering applications. As the simulation results illustrated, the large sidewall roughness results in a high scattering loss which heavily degrades the optical-confining capacity of the MDR, and a high occurrence possibility of resonance-splitting which hinders from a widespread application. However, owing to the fabrication imperfections, sidewall roughness is inevitable.

To mitigate the impact of the sidewall roughness on the confined optical field, an additional slab waveguide is employed to wrap the disk and bus waveguide in the proposed Type-II and Type-III MDRs. The devices are designed to have an all-pass configuration and fabricated using a CMOS-compatible technology with 193-nm deep ultra-violet lithography in IMEC, Belgium. Note that three-level etchings are realized directly using the standard process and no other additional process is needed, which is of importance to a mass production.

8.1.2 Evaluation of an ultra-compact MDR

Fig. 8.4(a) illustrates the SEM micrographs of the top-view of three fabricated MDRs which have an identical radius of 3.7 μm, much smaller than the radius of the MRRs allowed by the fabrication using the same process. Such ultra-compact footprint of the MDRs offers the compelling advantage in large-scale and high-density integration. Fig. 8.4(b) shows the sidewalls of the three MDRs captured at a sample tilt angle of 45^{o}. The slab waveguide in Type-II and Type-III MDRs has a height of 60 nm, and the disk in Type-III MDR has a height of 150 nm. Fig. 8.4(c) shows a closer view of the coupling region of the three MDRs.

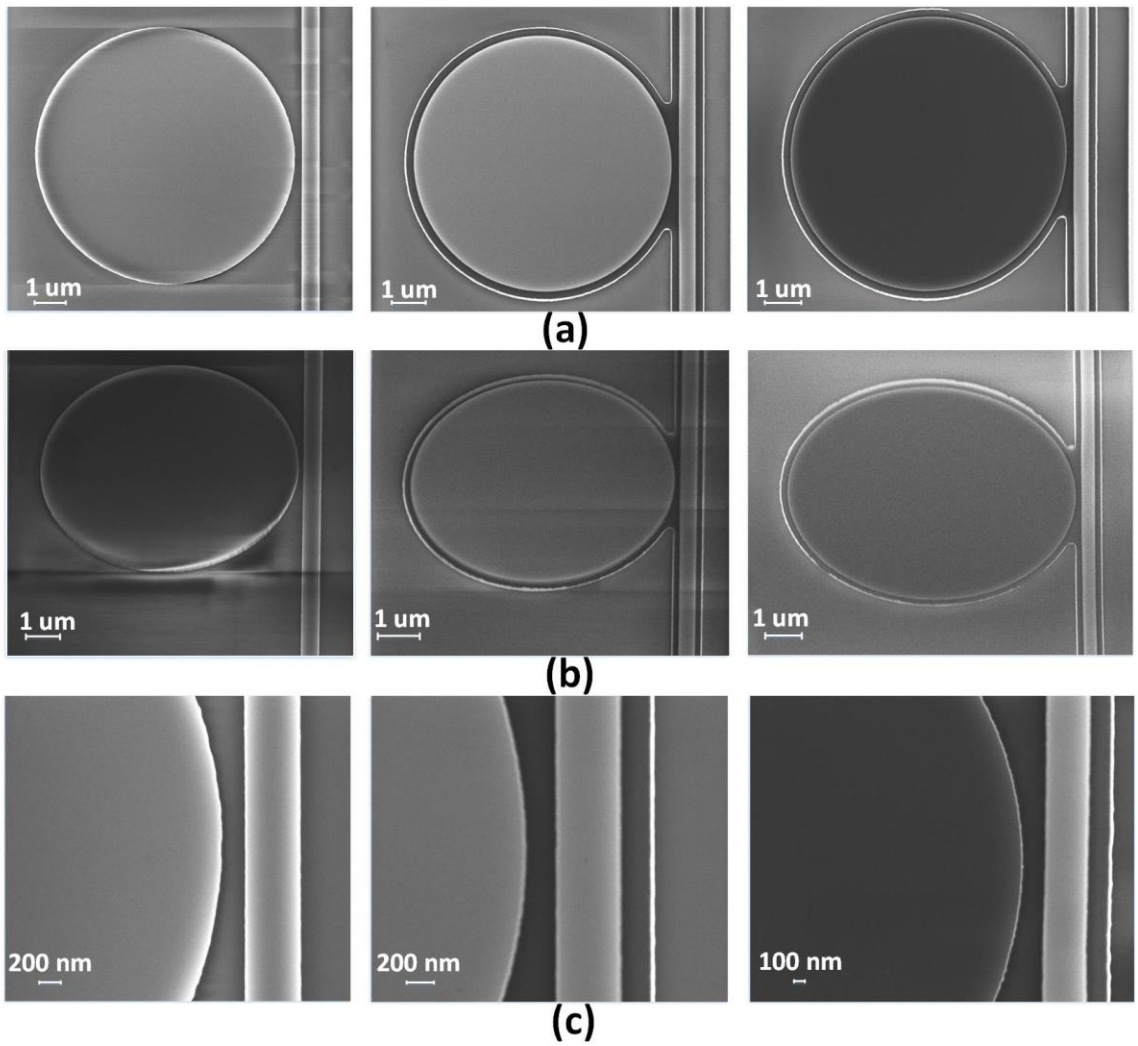

Fig. 8.4 (a) SEM micrographs of the fabricated three MDRs; (b) sidewalls of the three disks captured at a sample tilt angle of 45^{o}; (c) a closer view of the structures at the coupling region.

The optical performances of the three MDRs are evaluated, which is done by measuring the transmission spectrums of the three fabricated MDRs using an optical vector analyzer (LUNA OVA CTe).

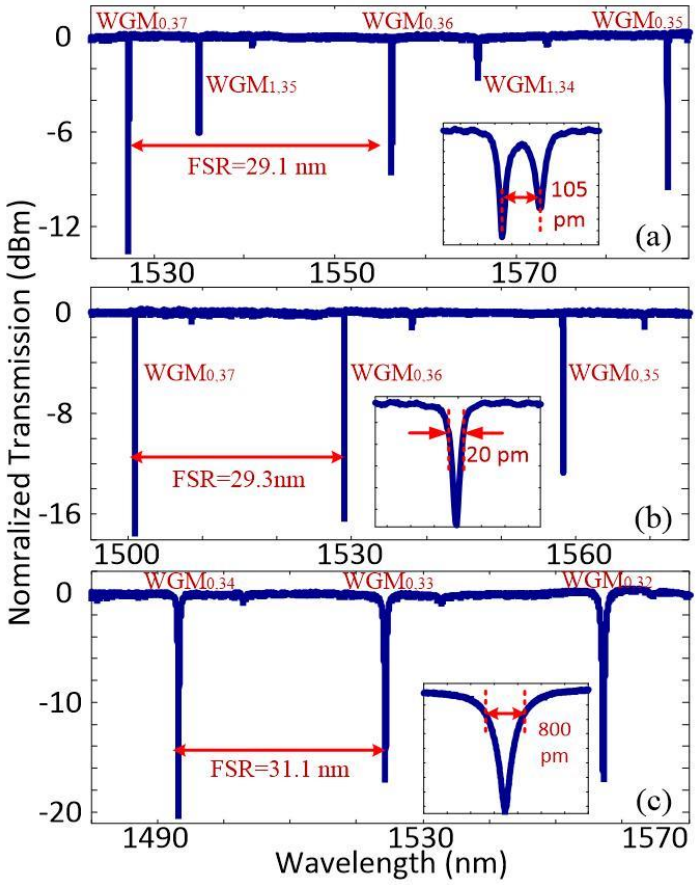

Fig. 8.5 Measured transmission spectrums of the fabricated (a) Type-I MDR, (b) Type-II MDR and (c) Type-III MDR. The insets show the zoom-in views of the $WGM_{0,36}$ mode resonance for the Type-I and Type-II MDRs, the $WGM_{0,33}$ mode resonance for the Type-III MDR.

Fig. 8.5(a) shows the normalized transmission spectrum of the fabricated Type-I MDR. As can be seen, the disk supports the fundamental and the first-order WGMs, which matches well with the simulation result shown in Fig. 8.3 except a small resonance wavelength shift induced by the fabrication imperfections. The inset gives a zoom-in view of the $WGM_{0,36}$ mode resonance. Note that this mode is obviously resonance-splitting, which is caused Rayleigh scattering from the sidewall roughness. A 3-dB bandwidth of 105 pm is shown, corresponding to a normalized splitting Q-factor of 15,600. Fig. 8.5(b) shows the normalized transmission spectrum of the fabricated Type-II MDR. The spectrum is clear and simple, in

which only the fundamental mode is supported and the high-order modes are effectively suppressed. This single-mode operation results from the perfect phase-matching in which the width of the bus waveguide is specifically designed to exactly excite the fundamental mode in the disk, and the slab waveguide introduction which induces the high-order modes to couple into the leaky modes. In addition, no resonance-splitting is observed at a high wavelength resolution of 2.4 pm or 30 MHz. This is attributed to the introduction of a slab waveguide surrounding the disk and the bus waveguide again, which makes the part of sidewall further away from the confined optical mode to weaken Rayleigh scattering from the sidewall roughness. The inset gives a zoom-in view of the $WGM_{0,36}$ mode resonance, which has a 3-dB bandwidth of around 20 pm, which corresponds to a Q-factor of 78,000. Compared with the Q-factor of the Type-I MDR, this Q-factor is significantly increased, which confirms a decreased scattering loss by using a slab waveguide. Note that the Q-factor of our proposed Type-II MDR is still smaller than the one reported in [42]. The main reason is that our proposed MDR has a much smaller radius of 3.7 μm than the radius in [42] as large as 20 μm. And our Q-factor is a loaded Q-factor calculated from the measured fundamental WGM mode resonance while in [42] it is an unloaded Q-factor of the second-order WGM mode resonance which did not consider the coupling loss. The ultra-small size and super-high Q-factor is the distinct advantage of our proposed MDR. Furthermore, the slab waveguide introduction also creates the opportunity for incorporation of a lateral PN junction to realize the electrical tunability of the resonance. Fig. 8.5(c) shows the normalized transmission spectrum of the fabricated Type-III MDR. Again, a clear and simple spectrum is observed, which confirms again the effectiveness of our proposed design in enabling a single-mode operation and mitigating the resonance-splitting problem. The inset presents a

zoom-in view of the $WGM_{0,33}$ mode resonance, which has a 3-dB bandwidth of around 800 pm, corresponding to a Q-factor of 2,000. The Q-factor is heavily decreased due to the coupling loss caused by the different waveguide heights between the disk and the bus waveguide, and the increased radiation loss from the strong optical field near the disk top surface. From the measurement results, the MDR with a height of 220 nm has a significantly improved Q-factor which is useful for narrowband filtering. The MDR with a height of 150 nm has a strong energy around the top surface of the disk, which is useful for refractive index sensing. Their ultra-compact features could elevate a high integration density and high power-efficiency of a chip.

8.2 Its application in microwave photonics

Thanks to its ultra-high Q-factor, the Type-II MDR can find the applications in microwave photonics such as photonic microwave filter and optical microwave filter.

8.2.1 A photonic microwave filter

Microwave photonic filters are important devices due to the high operating frequency and large tunable range. The Type-II MDR can be used to implement a microwave photonic filter (MPF), by taking advantage of its narrow bandwidth. A frequency-tunable MPF based on phase-modulation to intensity-modulation conversion in an MDR is demonstrated. A phase-modulated optical signal is sent to an MDR. If one of the two sidebands falls in the resonance notch of the MDR, the phase-modulated signal is converted to an intensity-modulated signal. The operation corresponds to a microwave filter with a passband determined by the notch of the MDR. The tunability of the microwave filter is achieved by tuning the wavelength of the

input optical carrier. Fig. 8.6(a) presents a zoom-in view of the measured frequency response of the MPF implemented using the Type-II MDR when the center frequency is tuned at 15.3 GHz, and Fig. 8.6(b) presents the measured frequency response with the central frequency tuned from 11 to 14 GHz. The bandwidth of the MPF could be further decreased if a Type-II MDR with a larger radius is employed.

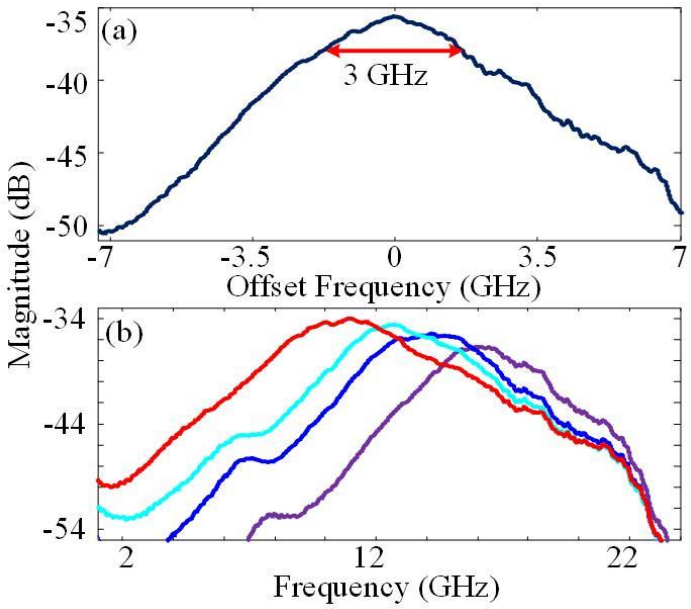

Fig. 8.6 (a) Zoom-in view of the frequency response when the center frequency is tuned at 15.3 GHz; (b) measured frequency responses of the MPF with the central frequency tuned from about 11 to 14 GHz.

8.2.2 An optical delay line

Optical delay lines are basic and important elements that can find applications in microwave photonic delay-line filtering and optical true-time delay beamforming. Since an MRR has a strong dispersion near the resonance and therefore a large group delay, on-chip optical delay lines are usually implemented using several cascaded MRRs. However, the comparatively large size and the relatively poor dispersion of the MRRs would inevitably increase the

system cost. To reduce the cost, a Type-II MDR with a stronger dispersion near the resonance is a better option to realize an optical delay line with a more compact size. Fig. 8.7 illustrates the measured group delay of the three fabricated MDRs. As can be seen in Fig. 8.7(b), the Type-II MDR presents a very large group delay of 231 ps, which offers great potential to realize on-chip optical delay lines.

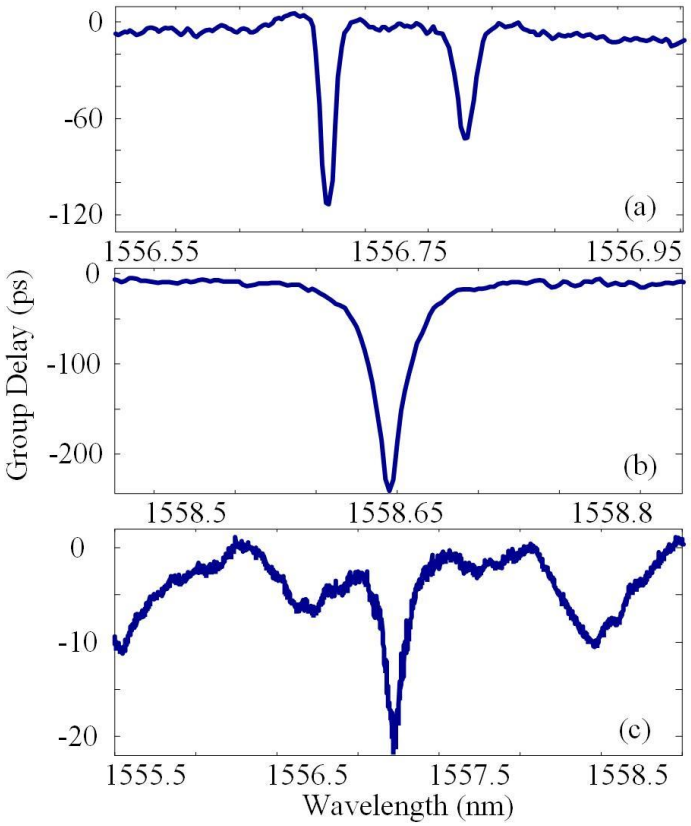

Fig. 8.7 Measured group delay of (a) the $TE_{0,36}$ mode resonance of the fabricated Type-I MDR; (b) of $TE_{0,36}$ of the fabricated Type-II MDR; and (c) $TE_{0,33}$ of the fabricated Type-III MDR.

8.3 Conclusion

In conclusion, to further reduce the footprint of an optical micro-cavity resonator, a silicon-based on-chip ultra-compact MDR with a single-mode operation and an ultra-high Q-factor

was proposed, fabricated and evaluated. The key features of the fabricated MDR included ultra-compact footprint, single-mode operation, no resonance-splitting, and ultra-high Q-factor, which made the MDR have a high potential for microwave photonic applications. The use of the fabricated MDR for the implementation for a microwave photonic filter and an optical delay line was experimentally demonstrated. The main disadvantage of the fabricated MDR is its untunable optical properties, which hinders from a wide application.

CHAPTER 9 SILICON-BASED ON-CHIP ELECTRICALLY TUNABLE MICRODISK RESONATOR

To enable the microdisk resonator (MDR) could be electrically tuned, in this Chapter by incorporating a lateral PN junction in the disk, an electrically tunable MDR is realized. Thanks to its electrical tunability, the use of the fabricated MDR in microwave photonic applications such as a high-speed electro-optic modulator, a tunable photonic temporal differentiator and a tunable optical delay line is experimentally demonstrated.

9.1 Electrically tunable microdisk resonator

To overcome the limitations of untunable properties and to make an MDR highly suitable for microwave photonic applications, we propose a novel design of a silicon-based on-chip electrically tunable MDR by introducing a specifically-designed slab waveguide to surround the disk and the lateral sides of the bus waveguide to suppress the higher-order whispering gallery modes (WGMs), and to support the incorporation of a lateral PN junction for electrical tunability. First, the higher-order WGMs have a tendency to couple into a leaky mode by incorporating a slab waveguide to surround the disk, which enables a single-mode operation. In addition, the introduction of a slab waveguide would make part of the sidewall further away from the fundamental WGM, which could weaken the scattering resulted from the sidewall roughness, and help alleviate the resonance-splitting. Furthermore, in a conventional MDR, it is impossible to implement a lateral PN junction since the center of the fundamental WGM is too close to the edge of the disk which gives an area that is not

sufficiently large to make a PN junction. Thanks to the introduction of the slab waveguide in the proposed work, the area is increased which allows the implementation of a lateral PN junction.

9.1.1 Design of an electrically tunable MDR

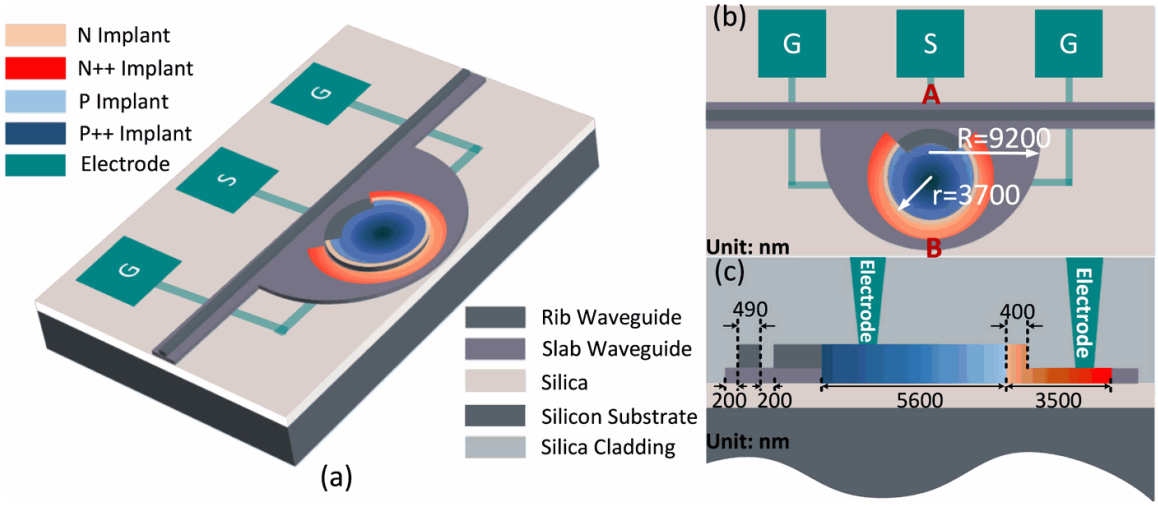

Fig. 9.1(a) Perspective view of an electrically tunable silicon-based on-chip MDR; (b) top view of the proposed MDR; (c) cross-sectional view of the planar along the direction from A to B on (b).

Fig. 9.1(a) illustrates the perspective view of an electrically tunable silicon-based on-chip MDR. It has an all-pass configuration consisting of a bus waveguide and a disk. To clearly illustrate the internal structure of the device, the cladding layer of silica is removed. As can be seen, the proposed MDR has a specifically-designed slab waveguide to surround the disk and the lateral sides of the bus waveguide. The employment of the slab waveguide aims to suppress the higher-order WGMs by coupling into leaky modes to have a single-mode operation and to enable the incorporation of a lateral PN junction to achieve the electrical tunability of the MDR. In addition, the introduction of the slab waveguide makes part of the

sidewall further away from the confined mode, which would weaken the scattering resulted from the sidewall roughness. This helps alleviate the resonance-splitting. To make the design to be compliant with the design rules, the slab waveguide is designed to have a special profile. Near the lateral sides of the bus waveguide, the widths of the slab waveguide are kept identical. Near the disk, in order to support the incorporation of a lateral PN junction, the slab waveguide is designed to have a semicircle profile to wrap the disk. Fig. 9.1(b) shows the top-view of the MDR. To make the disk have one resonance wavelength near 1550 nm in the *C* band, the disk is designed to have a radius of 3.7 μm and the slab waveguide has a radius of 9.2 μm. The lateral PN junction is formed along the edge of the disk. Since the plasma dispersion effect is more sensitive to the change of the free-hole concentration, in order to increase the tuning efficiency by increasing the overlap between the confined light mode with the p-type doping region, most of the disk is designed to be p-type doped, while the edge of the disk and the slab waveguide are n-type doped. To guarantee that the doping does not deteriorate the optical coupling between the bus waveguide and the disk, there is no doping along the arc with an angle of 120^{o} near the coupling region, as shown in Fig. 9.1(b). In addition, three contact windows are opened on the silica pads, with a 2-μm-thick aluminum layer deposited to make the contacts. Fig. 9. 1(c) illustrates the cross-sectional view of the planar structure along the direction from A to B in Fig. 9. 1(b). To meet the phase-matching condition for optical coupling between the bus waveguide and the disk which requires that the effective refractive index of the fundamental TE mode supported by the bus waveguide is equal to that of the fundamental WGM supported by the disk, the bus waveguide is designed to have a specific width of 490 nm. The coupling gap has a width of 200 nm. To optimize the tuning efficiency, the overlap between the PN junction and the

fundamental WGM is maximized by slightly shifting the center of the PN junction inward by 400 nm from the edge of the disk. To minimize the heavy doping induced absorption loss, additional p++ and n++ implantations, 1 μm away from the center of the PN junction, are utilized for ohmic contact formation.

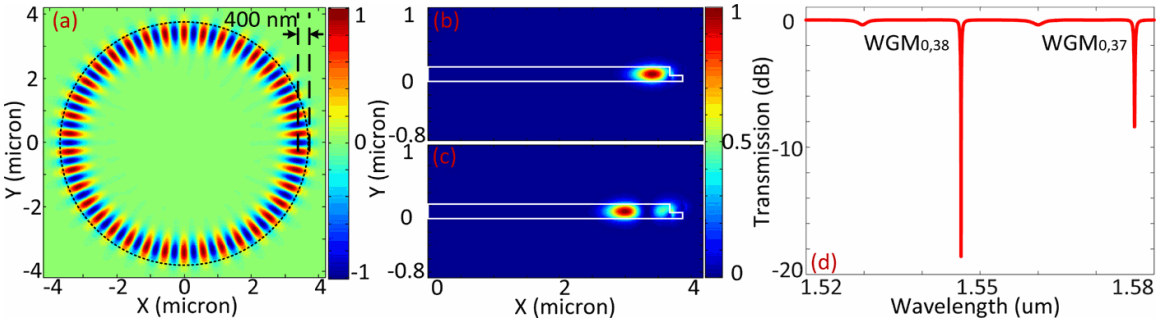

Fig. 9.2 Simulation results: (a) electrical field amplitude of the fundamental WGM at 1546 nm evaluated in the x–y plane at the center of the proposed disk; (b) electrical field profile of the fundamental radial TE mode in the proposed disk; (c) electrical field profile of the first-order radial TE mode in the proposed disk; and (d) transmission spectrum.

Fig. 9.2(a) shows the electrical field amplitude of the fundamental WGM at 1546 nm evaluated in the x–y plane of the proposed MDR. The dotted black line depicts the profile of the disk. As can be seen, the center of the mode has a distance of 400 nm from the edge of the disk, which perfectly matches the slightly-shifted PN junction. In addition, by using the equation $n_{eff} = m\lambda_0 / 2\pi R$, where λ_0 is the resonance wavelength, m is the azimuth harmonic number of the WGM, and R is the disk radius, the effective refractive index of the individual WGM supported by the MDR can be calculated, which could be employed to calculate the width of the bus waveguide to meet the phase-matching condition. Fig. 9.2(b) illustrates the electrical field profile of the fundamental radial TE mode supported by the MDR. It is clear to see that the fundamental TE radial mode decays rapidly in the radial

direction. Thanks to the slab waveguide, part of the sidewall is further away from the confined mode, which would help weaken the scattering resulted from the sidewall roughness. This helps alleviate the resonance-splitting. Moreover, the energy profile of the fundamental radial TE mode exhibits an energy tail outside the disk, which would strengthen the optical coupling between the bus waveguide and the disk. Fig. 9.2(c) illustrates the electrical field profile of the first-order radial TE mode supported by the MDR. Compared with the fundamental radial TE mode, the first-order radial TE mode has a much stronger energy tail, which leads to its coupling into a leaky mode. Fig. 9.2(d) shows the simulated transmission spectrum of the proposed MDR. As can be seen, the MDR has a simple and clear transmission spectrum which presents a single-mode operation. Each notch in the spectrum represents a specific *WGMp,q* resonance in which *p* and *q* are the radial and azimuthal harmonic numbers. The higher-order WGMs are effectively suppressed, which is enabled because the width of the bus waveguide is specifically designed to excite the fundamental WGM in the disk, and the introduction of the slab waveguide makes the higher-order modes have a tendency to couple the light into the leaky mode. Note that in the simulation the sidewall roughness is not considered.

The proposed MDR is fabricated using a standard fabrication process of 248-nm deep ultraviolet lithography at IME, Singapore. Since a standard fabrication process is employed, the fabrication cost especially for high volume production is greatly reduced.

9.1.2 Evaluation of an electrically tunable MDR

Fig. 9.3(a) shows the image of the fabricated MDR captured by a microscope camera. Two TE-mode grating couplers with a center-to-center space of 254 μm are used to couple light

between the chip and the input and output fibers. To minimize the chip footprint and to reduce the bending loss, a strip waveguide is mostly used to guide the light wave signal. Since the bus waveguide in the electrically tunable MDR has a slab waveguide, which is different from the strip waveguide, a double-layer linear taper waveguide with a length of 50 μm is used for the mode transition between the strip waveguide and bus waveguide. The entire device is 167 μm in length and 230 μm in width, giving an ultra-compact footprint of 0.384 mm^2. Fig. 9.3(b) shows the zoom-in view of the disk. This small radius of the disk has an exceptional advantage in achieving high-density integration and reducing the power consumption.

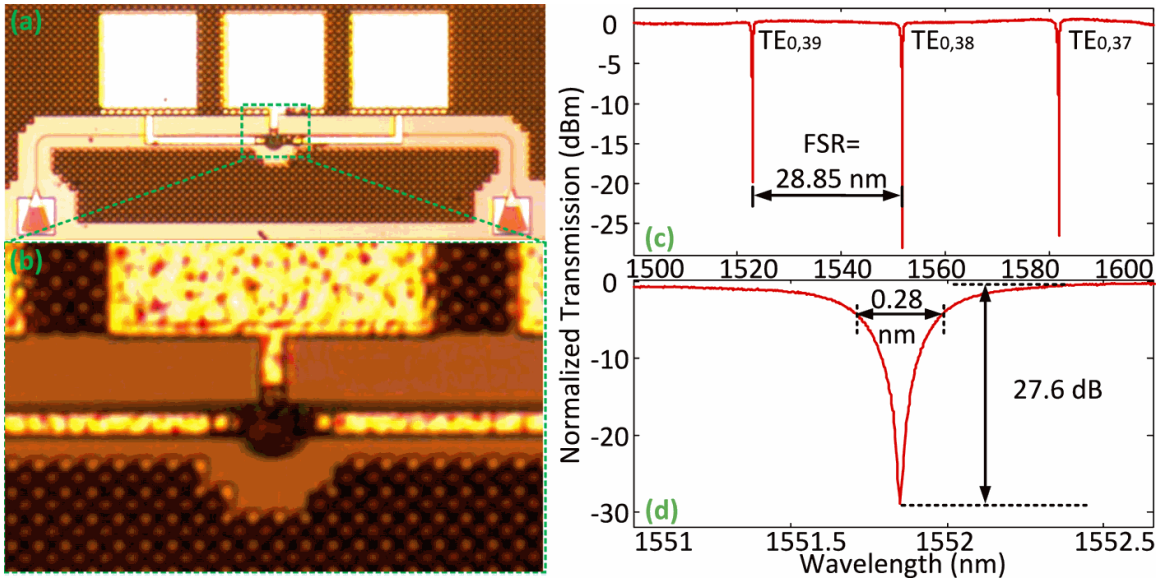

Fig. 9.3 (a) Image of the fabricated MDR; (b) zoom-in view of the microdisk; (c) measured transmission spectrum of the fabricated MDR; and (d) zoom-in view of the resonance of the fabricated MDR at the wavelength of 1551.84 nm.

The optical performance of the fabricated MDR is first evaluated using an optical vector analyzer (LUNA OVA CTe) to measure its transmission spectrum. Fig. 9.3(c) shows the measured transmission spectrum when a zero bias voltage is applied, which exhibits a single-

mode operation. Each notch in the spectrum represents a resonance wavelength and the FSR is estimated to be 28.85 nm, which ensures that in the *C* band there is only one resonance wavelength. This simple and clear transmission spectrum matches well with the simulation result in Fig. 9.2(d) except that the resonance wavelength is shifted due to the fabrication errors, and the high-order WMG modes are completely suppressed due to the sidewall roughness induced scattering loss. The insertion loss of the fabricated MDR is measured to be 13 dB, most of which is caused by the fiber-to-fiber I/O coupling loss. By optimizing the design of the grating couplers, the insertion loss would be largely reduced. In addition, no resonance-splitting is observed, which confirms that the introduction of the slab waveguide weakens the scattering resulted from the sidewall roughness. Fig.9.3(d) shows the zoom-in view of the resonance $WGM_{0,38}$, of which the resonance wavelength is located at 1551.84 nm. The resonance has a 3-dB bandwidth of 280 pm with a Q-factor of 5,500, and an extinction ratio of 27.6 dB.

Then, the DC performance of the fabricated MDR is evaluated when the PN junction is reverse biased. To clearly illustrate the optical performance change when a bias voltage is applied, we show in detail the wavelength shift of the notch at the resonance $WGM_{0,38}$. Fig. 9.4(a) shows the measured voltage-current (V-I) curve of the PN junction when reverse biased. As can be seen, the PN junction reaches breakdown at approximately 15.7 V. Fig. 9.4(b) shows that the notch shift as the bias voltage is increasing. When reverse biased, as the voltage is increasing, more free carriers are extracted and the depletion region is widened. Thus, based on the plasma dispersion effect, the effective refractive index of the waveguide is increased which would lead to a red-shifted of the spectrum. In the meanwhile, the decrease in the number of free carriers would reduce the free-carrier induced absorption loss, which

could elevate the Q-factor, and the extinction ratio is also improved since the coupling condition is reaching the critical condition. For example, when biased at 19 V, the injection current is measured to 500 nA. From the measured resonance spectrum, the Q-factor is increased to 7,050, the extinction ratio is increased to 37.3 dB, and the notch wavelength is red-shifted by 94 pm. Fig. 9.4(c) shows the tuning of the spectral response, which gives a wavelength shift rate of 4.4 pm/V. Then, the DC performance of the fabricated MDR is evaluated for the PN junction being forward biased. Fig. 9.4(d) shows the V-I curve of the PN junction when forward biased, which indicates that the junction is turned on at about -0.8 V. Fig. 9.4(e) shows a blue-shift of the notch as the forward voltage is increasing. The blue shift is resulted from the decrease in the refractive index induced by the free-carrier injection. In addition, the injected free-carrier would also introduce an excess absorption loss, which would degrade the performance of the fabricated MDR. As can be seen in Fig. 9.4(e), when the bias voltage is increasing, the Q-factor and the extinction ratio are reduced. For a current of 1.2 mA when biased at -1.4 V, the Q-factor is reduced to 3,880 and the extinction ratio is reduced to 8.6 dB. The blue shift of the notch wavelength is found to be 0.67 nm. Fig. 9.4(f) shows the tuning of the spectral response which gives a wavelength shift rate of -1.15 nm/V after the PN junction is turned on. When a bias voltage is applied on the fabricated MDR, the notch could be shifted, which could find applications as a tunable optical filter [159]. To improve the Q-factor of the MDR for high wavelength selectivity as an optical filter, one solution is to increase the radius of the disk. To have a filter with a flat-top, a design of cascaded MDRs with specifically designed coupling gaps could be employed.

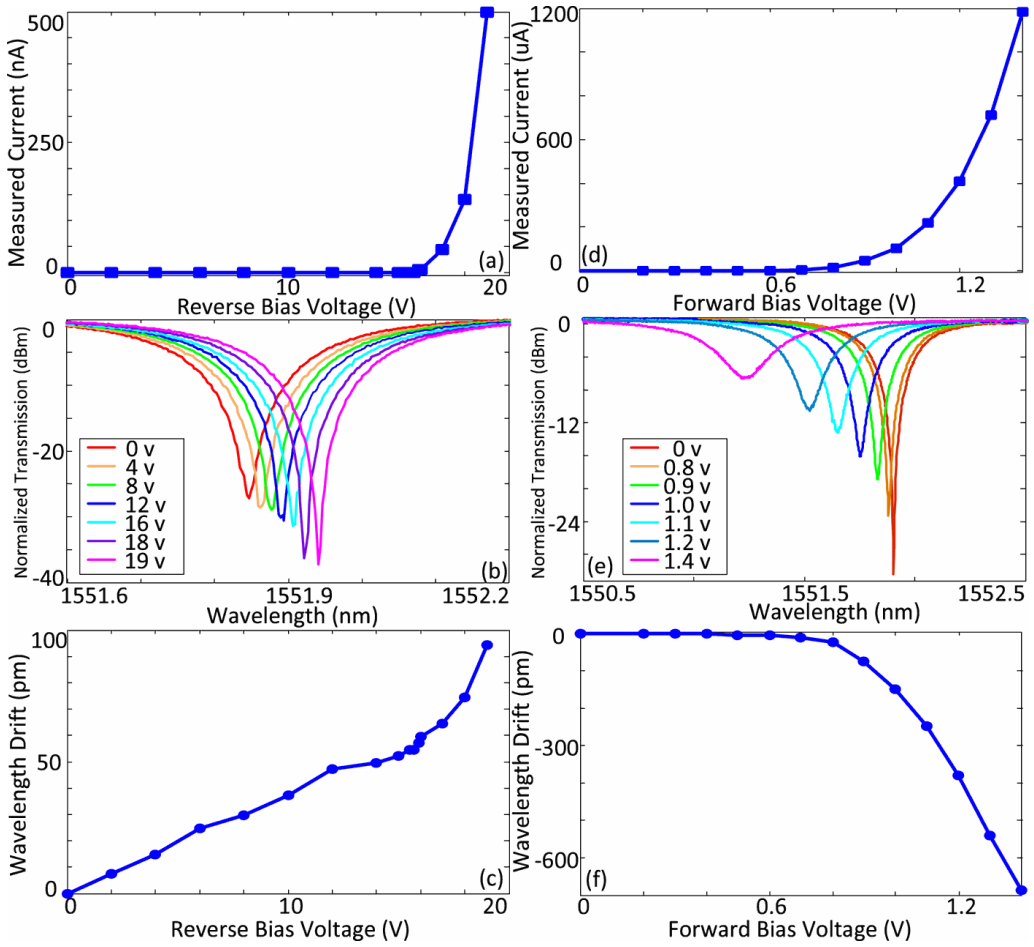

Fig. 9.4 Measurement results for the PN junction being reverse biased: (a) measured V-I curves of the PN junction, (b) wavelength shift of the resonance $WGM_{0,38}$, and (c) wavelength shift when the bias voltage is increased. Measurement results for the PN junction being forward biased: (d) measured V-I curves of the PN junction, (e) wavelength shift of the resonance $WGM_{0,38}$, and (f) wavelength shift when the bias voltage is increased.

9.2 Its applications in microwave photonics

The key features of the fabricated MDR include ultra-compact footprint, single-mode operation, no resonance-splitting, and flexible electrical tunability, which make the MDR

highly suitable for the implementation of a high-speed electro-optic modulator, a tunable fractional-order photonic temporal differentiator and a tunable optical delay line.

9.2.1 A high-speed electro-optic modulator

Since the light-confinement resonating structure of the optical microcavity can enhance the effect of refractive index change, we propose to use the electrically tunable MDR for the implementation of an electro-optic modulator. For a silicon microdisk modulator, its 3-dB modulation bandwidth depends on the *RC* time of the reverse-biased PN junction and the photon lifetime of the cavity. The photon lifetime is determined by the Q-factor of the cavity, given by $\tau = Q\lambda_0 \,/\, 2\pi c$, where c is the speed of light in vacuum. Based on the estimated Q-factor of the fabricated MDR, the photon-lifetime determined cutoff frequency is calculated to be 35.1 GHz according to $f_\tau = 1 \,/\, 2\pi\tau$. An experiment is performed to verify the effectiveness of using the fabricated MDR as a modulator. The AC performance of the fabricated MDR is evaluated using a vector network analyzer (Agilent E8364A) to measure its electro-optic frequency response. Fig. 9.5 shows the measured electro-optic frequency response for a reverse bias voltage tuned from 0 V to 0.9 V when the wavelength of the input light is chosen to be 1551.81 nm in the linear regime. At a bias voltage of 0 V, the 3-dB modulation bandwidth is measured to be 5 GHz, and at a bias voltage of 0.9 V, the 3-dB modulation bandwidth is measured to be 30.5 GHz. As can be found, with the reverse bias voltage increasing from 0 to 0.9 V, the 3-dB modulation bandwidth is increased from 5 to 30.5 GHz. This is because the red-shift of the resonance induced by the increase in the reverse bias voltage changes the photon-lifetime of the input wavelength. As the reverse bias voltage is increasing, the resonance is red-shifted, while the input wavelength keeps unchanged,

which makes the resonance wavelength further away from the input wavelength. Since the photon lifetime of the cavity is wavelength-dependent, at the resonance wavelength, the light-confinement capacity of the cavity is strongest and the photon lifetime is longest. Therefore, the red-shift would lead to a weaker confinement capability of the cavity for the input wavelength and its corresponding photon lifetime is becoming shorter. Thus, the measured 3-dB modulation bandwidth is becoming larger. This photon-lifetime-dependent electro-optic frequency response confirms that the modulation bandwidth of the fabricated MDR is mainly limited by the photon lifetime of the cavity. Compared to a well-developed silicon microring modulator, the fabricated MDR has an equivalent capacity of high-speed electro-optic modulation but an ultra-compact footprint, which indicates a smaller power consumption and a significant potential for the applications in the chip-to-chip interconnect [160].

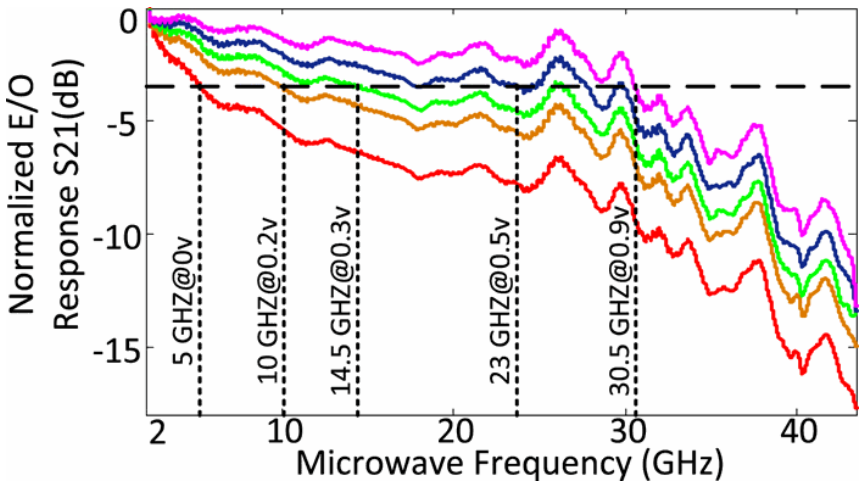

Fig. 9.5 Measured electro-optic frequency response for a reverse bias voltage tuned from 0 V to 0.9 V when the wavelength of the input light is chosen to be 1551.81 nm in the linear regime.

9.2.2 A tunable fractional-order temporal differentiator

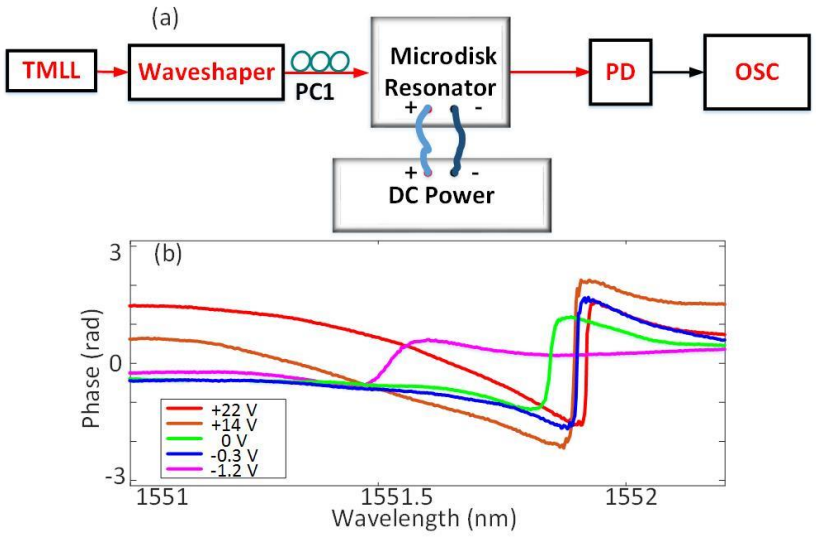

Fig. 9.6 (a) Experimental setup. TMML: tunable mode lock laser, PC: polarization controller, PD: photodetector, OSC: oscilloscope; (b) measured phase responses of the resonance $WGM_{0,38}$ at different bias voltages.

Photonic processing of microwave signals is a topic of interest in microwave photonics. A photonic temporal differentiator, as one of the basic signal processing blocks, is used to perform temporal differentiation of the complex envelope of an arbitrary optical signal.[21] In general, a photonic temporal differentiator can be realized using an optical system that has a transfer function given by $[j(\omega - \omega_0)]^n$, where n is the differentiation order, ω is the optical frequency and ω_0 is the optical carrier frequency. When the differentiation order n is not one, the operator is generalized to be a fractional-order photonic temporal differentiator.[22] MRRs have been intensively investigated in realizing the photonic temporal differentiation. To verify that the fabricated MDR can be used to implement a photonic temporal differentiator with a tunable differentiation order, an experiment based on the setup shown in Fig. 9.6(a) is performed. A short Gaussian pulse from a tunable mode locked laser (TMLL) is sent to a WaveShaper to shape the Gaussian pulse to have a temporal full width at half

maximum (FWHM) of 500 ps. A polarization controller (PC) is used to adjust the polarization state of the input signal to minimize the polarization-dependent loss. The differentiated signal is detected at a 45-GHz photodetector (PD) and its waveform is observed by a sampling oscilloscope (OSC). A power supply is used to provide a bias voltage applied to the MDR via a probe. For the implementation of a temporal differentiator, the phase response is more important than the magnitude response. The magnitude response of an ideal temporal differentiator may not be exactly satisfied by using the transmission band of the disk resonance, but the phase response which plays a key role can be controlled to be identical to that required by an ideal temporal differentiator. Fig. 9.6(b) shows the phase responses of the resonance $WGM_{0,38}$ at different bias voltages. By changing the bias voltage, the phase response is changed, which could be used to realize a temporal differentiator with a different differentiation order. Note that as the bias voltage is tuned, the resonance wavelength also shifts, which requires that the carrier wavelength of the input Gaussian pulse is re-aligned to the resonance wavelength to enable an effective differentiation.

The shaped pulse at the output of the Waveshaper is shown as solid line in Fig. 9.7(a). An ideal Gaussian pulse with an identical temporal width of 500 ps is also shown as dashed line in Fig. 9.7(a), for comparison. The experimentally generated input pulse is close to a Gaussian pulse with a slight deviation. A differentiated pulse is obtained at the output of the PD and the waveform is observed by the OSC. Fig. 9.7(b), (c), (d), (e), and (f) shows a differentiated pulse with differentiation orders of n = 0.38, 0.86, 1.03, 1.12, or 1.53, as solid lines. Simulated pulses at the output of an ideal differentiator are also shown in Fig. 9.7(b)-(f), as dashed lines. As can be seen, a good agreement is achieved between the experimentally generated pulses and the simulated pulses, which confirms the effectiveness of the MDR as

a temporal differentiator. The root mean square error (RMSE) in the worst case (Fig. 9.7(f)) is calculated to be 9%. It should be noted that the difference in the notch is caused mainly due to the limited bandwidth of the PD (45 GHz). In addition, the wavelength shift with the bias voltage change could be eliminated by incorporating a micro-heater in the MDR to introduce an opposite wavelength shift. Thus, a tunable fraction-order temporal differentiator with an unchanged resonance wavelength could be realized. Compared with a temporal differentiator using an MRR, a temporal differentiator using an MDR exhibits a larger tuning order with an ultra-compact footprint, which is highly needed in a more complicated signal processing system where the proposed MDR can be employed as a fundamental signal processing unit.

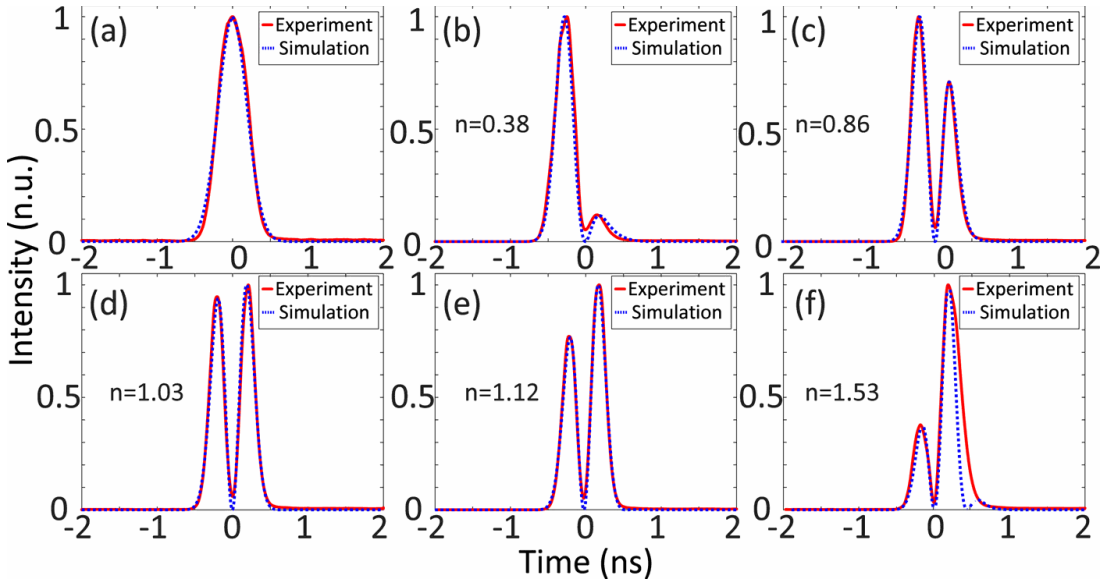

Fig. 9.7 Experimental results: (a) an input Gaussian pulse with an FWHM of 500 ps, and the differentiated pulses corresponding to a differentiation order of (b) n = 0.38, (c) n = 0.86, (d) n = 1.03, (e) n = 1.12, or (f) n = 1.53.

9.2.3 An electrically tunable optical delay line

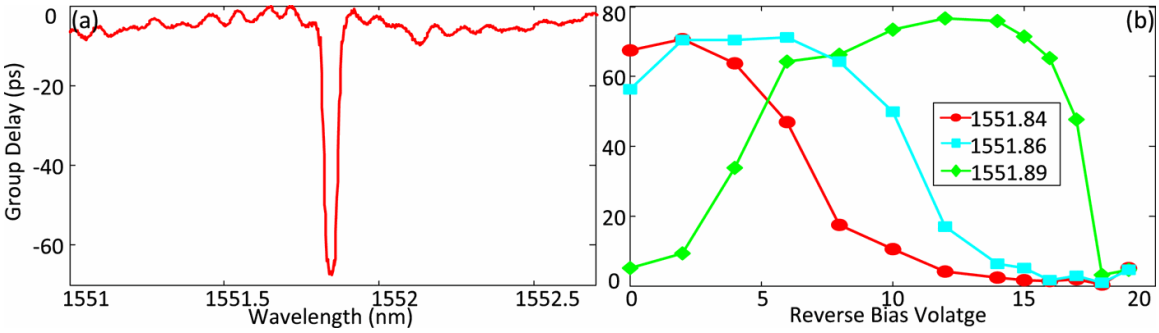

Fig. 9.8 (a) Measured group delay of the resonance $WGM_{0,38}$ in the fabricated MDR and (b) electrical tunability of the group delay at three different wavelengths.

Thanks to the light-confinement capacity, an on-chip microcavity has a strong dispersion near the resonance and thus a large group delay. Recently, an on-chip microcavity has been well studied to realize an optical delay line, which could find important applications in microwave photonic delay-line filtering and optical true-time delay beamforming. For example, an MRR or multiple cascaded MRRs have been used for the implementation of an optical delay line. However, the comparatively large size and the relatively weak dispersion of an MRR would make the footprint of the delay line quite larger. To reduce the footprint, an MDR with a stronger dispersion near the resonance is a good candidate to realize an integrated optical delay line. Fig. 9.8(a) illustrates the measured group delay of the resonance $WGM_{0,38}$ in the fabricated MDR. As can be seen, the MDR presents a very large group delay of 68 ps. The ultra-compact footprint with a strong group delay fully demonstrates its potential in realizing an on-chip optical delay line. Fig. 9.8(b) shows the electrical tunability of the group delay at three different wavelengths. As the reverse bias voltage is increasing, the group delays at the three different wavelengths give different changes. For example, at 1551.84 nm, shown in the red line, as the bias voltage increases, the time delay is firstly increased to 72 ps from 68 ps at a bias voltage of 0 V and then is decreased to zero when the

bias voltage is larger than 15 V. Such a change is resulted from the shift of the resonance at different bias voltages, which demonstrates the electrical tunability of the time delay. Again, the ultra-compact footprint, the large group delay and the flexible electrical tunability make an MDR a better option in realizing an on-chip optical delay line. Note that for an optical delay line, a wider operation width is always preferred. By series-double-coupling several MDRs, a delay line with a wider bandwidth could be achieved [161].

9.3 Conclusion

In conclusion, to enable the MDR could be electrically tuned, by incorporating a lateral PN junction in the disk, an electrically tunable MDR was realized. Thanks to its electrical tunability, the use of the fabricated MDR in microwave photonic applications such as a high-speed electro-optic modulator, a tunable photonic temporal differentiator and a tunable optical delay line was experimentally demonstrated. An electro-optic modulator with a 3-dB modulation bandwidth of ~30.5 GHz was experimentally demonstrated. In addition, a tunable fractional-order photonic temporal differentiator with a tunable differentiation order from 0.38 to 1.53 and an electrically tunable optical delay-line with a tunable time delay as large as 72 ps was also experimentally demonstrated.

The key features of the proposed silicon-based on-chip MDR include ultra-compact footprint, single-mode operation, no resonance-splitting, and flexible electrical tunability, which make the proposed MDR have a high potential for microwave photonic applications. In addition to the use of the proposed MDR for an electrically tunable optical delay-line and a tunable fractional-order photonic temporal differentiator, demonstrated in this paper, the design can also be used to achieve a wideband flat-top optical filter and a wideband optical delay line.

For example, to realize a wideband flat-top optical filter, one may cascade multiple MDRs with specifically designed coupling gaps, to make the MDRs have slightly offset resonances. The same design using cascaded MDRs with specifically designed coupling gaps can also be applied to implement a wideband optical delay line. In addition, the proposed MDR could act as a fundamental signal processing unit, to be employed in a more complicated signal processing system.

CHAPTER 10 SUMMARY AND FUTURE RESEARCH

10.1 Summary

In this thesis, two types of silicon photonic devices, waveguide Bragg gratings and optical micro-cavity resonators, were designed, developed and characterized, and the use of the developed devices in microwave photonic applications such as photonic generation of linearly chirped microwave waveform and photonic processing of microwave signals was studied.

Specifically, in Chapter 3 a silicon-based on-chip phase-shifted waveguide Bragg grating (PS-WBG) was designed, fabricated and characterized, and its use for the implementation of a photonic temporal differentiator was experimentally demonstrated. To have a waveguide grating that is wavelength tunable, in Chapter 4 we proposed to implement a tunable waveguide grating by incorporating a PN junction across the waveguide grating, to use the free-carrier plasma dispersion effect in silicon to achieve wavelength tuning. The use of a pair of wavelength-tunable waveguide gratings to form a wavelength-tunable Fabry-Perot resonator for microwave photonic signal processing was studied. Thanks to its electrical tunability, a high-speed electro-optic modulator, a tunable fractional-order photonic temporal differentiator and a tunable optical delay line were experimentally demonstrated. To increase the bandwidth of a waveguide grating, in Chapter 5 a linearly chirped waveguide Bragg grating (LC-WBG) was designed, fabricated and evaluated. By incorporating two LC-WBGs in two arms of a Mach-Zehnder interferometer (MZI) structure, an on-chip optical spectral

shaper was produced, which was used in a photonic microwave waveform generation system based on spectral-shaping and wavelength-to-time (SS-WTT) mapping for linearly chirped microwave waveform (LCMW) generation. To enable the LC-WBG could be electrically tuned, in Chapter 6 a lateral PN junction was introduced in the grating and thus an electrically tunable LC-WBG was realized. By incorporating two tunable LC-WBGs in a Michelson interferometer structure, an electrically tunable optical spectral shaper was made. By applying the fabricated spectral shaper in an SS-WTT mapping system, a continuously tunable LCMW was experimentally generated.

Compared with a waveguide Bragg grating device, an on-chip optical micro-cavity resonator usually has a much smaller dimension, which is of help to increase the integration density and reduce the power consumption. Different on-chip optical micro-cavity resonators are studied in this thesis. In Chapter 7, an on-chip symmetric MZI incorporating multiple cascaded microring resonators was proposed. By controlling the radii of the rings, the MZI could be designed to have a spectral response with a linearly-varying free spectral range (FSR), which could be used in photonic generation of an LCMW, and to have a multi-channel spectral response with identical channel spacing, which could be used in the implementation of an independently tunable multi-channel fractional-order temporal differentiator. To further reduce the footprint of an optical micro-cavity resonator, in Chapter 8, an ultra-compact microdisk resonator (MDR) with a single-mode operation and an ultra-high Q-factor was proposed, fabricated and evaluated, and its use for the implementation of a microwave photonic filter and an optical delay line was experimentally demonstrated. To enable the MDR to be electrically tunable, in Chapter 9 an electrically tunable MDR was realized by incorporating a lateral PN junction in the disk. The use of the fabricated MDR in

microwave photonic applications such as a high-speed electro-optic modulator, a tunable photonic temporal differentiator and a tunable optical delay line was experimentally demonstrated.

10.2 Future research

A silicon-based on-chip electrically tunable sidewall-Bragg-grating Fabry-Perot filter was designed, fabricated and evaluated. Thanks to its electrical tunability, the use of the fabricated filter was studied for the implementation of a high-speed electro-optic modulator, a tunable photonic temporal differentiator and a tunable optical delay line. However, in the implementation of an electro-optic modulator, the modulation bandwidth was limited by the cavity and fabrication technology. The future work of improving the filter performance as an electro-optic modulator could be done by optimizing the Fabry-Perot cavity design, grating structure design and PN junction design. In the implementation of a tunable photonic temporal differentiator, when the differentiation order is tuned, the notch center of the filter also shifts, which requires that the carrier wavelength is also changed to re-align it to the notch center to enable an effective differentiation. To overcome this problem, the future work will be done by incorporating three independent pairs of electrodes for the two reflectors and the cavity in the filter which could be independently controlled. Thus, a tunable fraction-order temporal differentiator with a fixed resonance wavelength could be realized, and by programming the three independent electrodes, the tuning range of the differentiation order could also be increased. In the implementation of a tunable optical delay line, the main disadvantage is a narrow operation bandwidth of this delay line. The future work is to increase the operation bandwidth of a delay line by incorporating multiple cavity in the filter.

A silicon-based on-chip electrically tunable LC-WBG was proposed, fabricated and evaluated. By incorporating the electrically tunable LC-WBGs in a Michelson interferometer structure, an electrically-tunable optical spectral shaper was realized, which was used in a photonic microwave arbitrary waveform generation system based on SS-WTT mapping for tunable LCMW generation. The future work is to heterogeneously integrate a laser pulse source with this tunable spectral shaper, the dispersive element of an LC-WBG and a high-speed photodetector on a single chip. Thus, an integrated photonic microwave waveform generation system could be done, which would significantly reduce the system size and power consumption with an optimized performance.

A silicon-based on-chip electrically tunable MDR was proposed, fabricated and evaluated. The key features of the fabricated MDR included ultra-compact footprint, single-mode operation, no resonance-splitting, and flexible tunability, which made the MDR have a high potential for microwave photonic applications. In the implementation of a tunable photonic temporal differentiator, when the differentiation order is tuned, the resonance wavelength of the MDR also shifts, which requires that the carrier wavelength is also changed to re-align to the resonance wavelength to enable an effective differentiation. To overcome this problem, the future work will be done by incorporating an independent metallic micro-heater. Thus, a tunable fraction-order temporal differentiator with a fixed resonance wavelength could be realized. In the implementation of a tunable optical delay line, the main disadvantage is a narrow operation bandwidth of this delay line. The future work is to increase the operation bandwidth of a delay line by cascading multiple MDRs with specifically-design coupling gaps.

In conclusion, these reported silicon-based devices exhibit competitive advantages in the optical performance with a comparatively more compact dimension. These successful demonstrations of individual devices pave the way toward realizing a fully functional system integration on a single chip with the use of silicon photonic technology.

REFERENCES

[1] R. A. Soref, "The past, present and future of silicon photonics," *IEEE J. Sel. Topics Quantum Electron.*, vol. 12, no. 6, pp. 1678–1687, Nov. 2006.

[2] B. Jalali and S. Fathpour, "Silicon photonics," *J. Lightw. Technol.*, vol. 24, no. 12, pp. 4600–4615, Dec. 2006.

[3] Z. Zhou, Z. Tu, T. Li, and X. Wang, "Silicon photonics for advanced optical interconnections," *J. Lightw. Technol.*, vol. 33, no. 4, pp. 928–933, Feb. 2015.

[4] M. Asghari and A. V. Krishnamoorthy, "Silicon photonics: Energy-efficient communication," *Nat. Photon.*, vol. 5, no. 5, pp. 268–270, May. 2011.

[5] M. Li, W. H. P. Pernice, C. Xiong, T. Baehr-Jones, M. Hochberg, and H. X. Tang, "Harnessing optical forces in integrated photonic circuits," *Nature*, vol. 456, no. 7221, pp. 458–458, Nov. 2008.

[6] J. Hu, X. Sun, A. Agarwal, and L. Kimerling, "Design guidelines for optical resonator biochemical sensors," *J. Opt. Soc. Am. B*, vol. 26, no. 5, pp. 1032–1041, May. 2009.

[7] H. Takesue, K. Harada, H. Fukuda, T. Tsuchizawa, T. Watanabe, K. Yamada, Y. Tokura, and S. Itabashi, "Silicon Photonics in Quantum Communications," in Conference on *Lasers and Electro-Optics/International Quantum Electronics Conference*, OSA Technical Digest (CD) (Optical Society of America, 2009), paper CMAA1.

[8] M. Foster, A. Turner, M. Lipson, and A. Gaeta, "Nonlinear optics in photonic nanowires," *Opt. Express*, vol. 16, no. 2, pp. 1300–1320, Jan. 2008.

[9] T. Jones, A. Spott, R. Ilic, A. Spott, B. Penkov, W. Asher, and M. Hochberg, "Silicon-on-sapphire integrated waveguides for the mid-infrared," *Opt. Express*, vol. 18, no. 12, pp. 12127–12135, May. 2010

[10]G. T. Reed, "Silicon Photonics: The State of the Art," Wiley, 2008.

[11]W. Bogaerts, P. Dumon, D. Thourhout, and R. Baets, "Low-loss, low-crosstalk crossings for SOI nanophotonic waveguides," *Opt. Lett.*, vol. 32, no. 19, pp. 2801–2803, Oct. 2007.

[12]F. Xia, M.J. Rooks, L. Sekaric, and Y.A. Vlasov, "Ultra-Compact High Order Ring Resonator Filters Using Submicron Silicon Photonic Wires for On-Chip Optical Interconnects," *Opt. Express*, vol. 15, no. 19, pp. 11934–11941, Sep. 2007.

[13]M. A. Popovíc, T. Barwicz, M. R. Watts, P. T. Rakich, L. Socci, E. P. Ippen, F. X. Kärtner, and H. I. Smith, "Multistage high-order microring-resonator add-drop filters," *Opt. Lett.*, vol. 31, no. 17, pp. 2571–2573, Sep. 2006.

[14]G. T. Reed, G. Mashanovich, F. Y. Gardes, and D. J. Thomson, "Silicon optical modulators," *Nat. Photon.*, vol. 4, no. 8, pp. 518–526, Aug. 2010.

[15]J. Michel, J. Liu, and L. C. Kimerling, "High-performance Ge-on-Si photodetectors," *Nat. Photon.*, vol. 4, no. 8, pp. 527–534, Aug. 2010.

[16]T. Murphy, J. Hastings, and H. Smith, “Fabrication and Characterization of Narrow-Band Bragg-Reflection Filters in Silicon-on-Insulator Ridge Waveguides,” *J. Lightw. Technol.*, vol. 19, no. 2, pp. 1938–1942, Dec. 2001.

[17]S. Pal, A. Chauhan, M. Singh, P. Kumar, M. Sharma, N. Pradhan, K. Singh, and C. Dhanavantri, “Realization of long-period corrugated grating in silica-on-silicon-based channel waveguide,” *IEEE Photon. Technol. Lett.*, vol. 21, no. 20, pp. 1490–1492, Oct. 2009.

[18]J. T. Hastings, M. H. Lim, J. G. Goodberlet, and H. I. Smith, “Optical waveguides with apodized sidewall gratings via spatial-phase-locked electron-beam lithography,” *J. Vac. Sci. Technol. B*, vol. 20, no. 6, pp. 2753–2757, Dec. 2002.

[19]X. Wang, W. Shi, R. Vafaei, N. Jaeger, and L. Chrostowski, “Uniform and sampled Bragg gratings in SOI strip waveguides with sidewall corrugations,” *IEEE Photon. Technol. Lett.*, vol. 23, no. 1, pp. 290–292, Oct. 2011.

[20]X. Wang, W. Shi, H. Yun, S. Grist, N. Jaeger, and L. Chrostowski, “Narrow-band waveguide Bragg gratings on SOI wafers with CMOS-compatible fabrication process,” *Opt. Express*, vol. 20, no. 14, pp. 15547–15558, Jun. 2012.

[21]P. Prabhathan, V. M. Murukeshan, J. Zhang, and P. V. Ramana, “Compact SOI nanowire refractive index sensor using phase shifted Bragg grating,” *Opt. Express*, vol. 17, no. 17, pp. 15330–15341, Aug. 2009.

[22]X. Wang, W. Shi, S. Grist, H. Yun, N. Jaeger, and L. Chrostowski, "Narrow-band transmission filter using phase-shifted Bragg gratings in SOI waveguide," *IEEE Photonics Conference*, 2011, pp.869–870.

[23]M. Spasojevic and L. R. Chen, "Discretely tunable optical delay lines using serial and step-chirped sidewall Bragg gratings in SOI," *Electron. Lett.*, vol. 49, no. 9, pp. 608–610, Apr. 2013.

[24]D. Tan, K. Ikeda, R. Saperstein, B. Slutsky, and Y. Fainman, "Chip-scale dispersion engineering using chirped vertical gratings," *Opt. Lett.*, vol. 33, no. 24, pp. 3013–3015, Dec. 2013.

[25] R. Jones, M. J. Paniccia and S. Merritt, "Tunablewaveguide based external cavity laser using a silicon/poly-silicon Bragg grating", *OSA Integrated Photonics Research Technical Digest*, 2004, Paper IThE4.

[26] A. Descos, C. Jany, D. Bordel, H. Duprez, G. B. D. Farias, P. Brianceau, S. Menezo, and B. B. Bakir, "Heterogeneously integrated III–V/Si distributed Bragg reflector laser with adiabatic coupling," *Eur. Conf. Opt. Commun.*, London, U.K., 2013.

[27] W. Shi, H. Yun, C. Lin, M. Greenberg, X. Wang, Y. Wang, S. Fard, J. Flueckiger, N. A. F. Jaeger, L. Chrostowski, "Ultra-compact, flat-top demultiplexer using anti-reflection contra-directional couplers for CWDM networks on silicon," *Opt. Express*, vol. 21, no. 6, pp. 6733–6738, Mar. 2013.

[28] T. Erdogan, “Fiber grating spectra,” *J. Lightw. Technol.*, vol. 15, no. 8, pp. 1277–1294, Aug. 1997.

[29] G. P. Agrawal and S. Radic, “Phase-shifted fiber Bragg gratings and their application for wavelength demultiplexing,” *IEEE Photon. Technol. Lett.*, vol. 6, no. 8, pp. 995–997, Aug. 1994.

[30] L. Chrostowski, S. Grist, J. Flueckiger, W. Shi, X. Wang, E. Ouellet, H. Yun, M. Webb, B. Nie, Z. Liang, K. C. Cheung, S. A. Schmidt, D. M. Ratner, and N. A. F. Jaeger, “Silicon photonic resonator sensors and devices,” *Proceedings of SPIE*, vol. 8236, pp. 823620, Jan. 2012

[31] N. K. Berger, B. Levit, B. Fischer, M. Kulishov, D. V. Plant, and J. Azaña, “Temporal differentiation of optical signals using a phase- shifted fiber Bragg grating,” *Opt. Express*, vol. 15, no. 2, pp. 371–381, Jan. 2007.

[32] Z. Pan, Y. W. Song, C. Yu, Y. Wang, Q. Yu, J. Popelek, H. Li, Y. Li, and A. E. Willner, “Tunable chromatic dispersion compensation in 40 Gbit/s systems using nonlinearly chirped fiber Bragg grating”, *J. Lightw. Technol.*, vol. 20, no. 12, pp. 2239-2246, Dec. 2002.

[33] J. P. Yao, J. Yang and Y. Liu, “Continuous true-time-delay beamforming employing a multiwavelength tunable fiber laser source,” *IEEE Photon. Technol. Lett.*, vol. 14, no. 5, pp. 687-689, May 2002.

[34] K.-M. Feng, J.-X. Cai, V. Grubsky, D. S. Starodubov, M. I. Hayee, S. Lee, X. Jiang, A. E. Willner, and J. Feinberg, “Dynamic dispersion compensation in a 10 Gbit/s optical system

using a voltage controlled tuned nonlinearly chirped fiber Bragg grating," *IEEE Photon. Technol. Lett.*, vol. 11, no. 10, pp. 373-375, Mar. 1999.

[35] E. Choi, J. Na, S. Y. Ryu, G. Mudhana, B. H. Lee, "All-fiber variable optical delay line for applications in optical coherence tomography: Feasibility study for a novel delay line," *Opt. Express*, vol. 13, no. 4, pp. 1334-1345, Feb. 2005.

[36] W. Bogaerts, P. De Heyn, T. Van Vaerenbergh, K. De Vos, S. K. Selvaraja, T. Claes, P. Dumon, P. Bienstman, D. Van Thourhout, and R. Baets, "Silicon microring resonators," *Laser Photon. Rev.*, vol. 6, no. 1, pp. 47–73, Sep. 2011.

[37] S. Xiao, M. Khan, H. Shen, and M. Qi, "A highly compact third-order silicon microring add-drop filter with a very large free spectral range, a flat passband and a low delay dispersion," *Opt. Express*, vol. 15, no. 22, pp. 14765–14771, Oct. 2007.

[38] T. Hu, W. Wang, C. Qiu, P. Yu, H. Qiu, Y. Zhao, X. Jiang, and J. Yang, "Thermally tunable filters based on third-order microring resonators for WDM applications," *IEEE Photon. Technol. Lett.*, vol. 24, no. 6, pp. 524–526, Mar. 2012.

[39] F. Xia, L. Sekaric and Y.A. Vlasov, "Ultracompact optical buffers on a silicon chip," *Nat. Photon.*, vol. 1, no. 1, pp. 65–71, Dec. 2007.

[40] J. Poon, J. Scheuer, Y. Xu, and A. Yariv, "Designing coupled-resonator optical waveguide delay lines," *J. Opt. Soc. Am. B*, vol. 21, no. 9, pp. 1665–1673, Sep. 2004.

[41] M. Soltani, Q. Li, S. Yegnanarayanan, and A. Adibi, "Toward ultimate miniaturization of high Q silicon traveling-wave microresonators," *Opt. Express*, vol. 18, no. 19, pp. 19541–19557, Sep. 2010.

[42] M. Soltani, S. Yegnanarayanan, and A. Adibi, "Ultra-high Q planar silicon microdisk resonators for chip-scale silicon photonics," *Opt. Express*, vol. 15, no. 8, pp. 4694–4704, Apr. 2007.

[43] E. Hosseini, S. Yegnanarayanan, A. Atabaki, M. Soltani, and A. Adibi, "Systematic design and fabrication of high-Q single-mode pulley-coupled planar silicon nitride microdisk resonators at visible wavelengths," *Opt. Express*, vol. 18, no. 3, pp. 2127–2136, Feb. 2010.

[44] G. Cocorullo and I. Rendina, "Thermo-optical modulation at 1.5 um in silicon etalon," *Electron. Lett.*, vol. 28, no. 1, pp. 83–85, Jan. 1992.

[45] R. A. Soref and B. R. Bennett, "Electro-optical effects in silicon," *IEEE J. Quantum Electron.*, vol. 23, no. 1, pp. 123–129, Jan. 1987.

[46] R. L. Espinola, M.-C. Tsai, J. T. Yardley, and R. M. Osgood, "Fast and low-power thermooptic switch on thin silicon-on-insulator," *IEEE Photon. Technol. Lett.*, vol. 15, no. 10, pp. 1366–1368, Oct. 2003

[47] T. Yamane, N. Nagai, S. Katayama, and M. Todoki, "Measurement of the thermal conductivity of silicon dioxide thin films using a 3-omega method," *J. Appl. Phys.*, vol. 91, no. 12, pp. 9772–9776, Jun. 2002

[48] C. K. Tang and G. T. Reed, "Highly efficient optical phase modulator in SOI waveguides," *Electron. Lett.*, vol. 31, no. 6, pp. 451–452, Mar. 1995.

[49] A. Liu, R. Jones, L. Liao, D. Samara-Rubio, D. Rubin, O. Cohen, R. Nicolaescu, and M. Paniccia, "A high-speed silicon optical modulator based on a metal-oxide-semiconductor capacitor," *Nature*, vol. 427, no. 6975, pp. 615–618, Feb. 2004.

[50] F. Y. Gardes, G. T. Reed, N. G. Emerson, and C. E. Png, "A sub-micron depletion-type photonic modulator in Silicon on Insulator," *Opt. Express*, vol. 13, no. 22, pp. 8845–8853, Oct. 2006.

[51] M. Hochberg and T. B. Jones, "Towards a fabless silicon photonics," *Nat. Photon.*, vol. 4, no. 8, pp. 492–494, Aug. 2010.

[52]http://www2.imec.be/be_en/home.html

[53]https://www.a-star.edu.sg/ime/

[54]https://www.lumerical.com/

[55]https://www.mentor.com/company/

[56] J. Capmany and D. Novak, "Microwave photonics combines two worlds," *Nat. Photon.*, vol. 1, no. 6, pp. 319–330, Apr. 2007.

[57] A. J. Seeds, "Microwave photonics," *IEEE Trans. Microw. Theory Tech.*, vol. 50, no. 3, pp. 877–887, Mar. 2002.

[58] A. J. Seeds and K. J. Williams, “Microwave photonics,” *J. Lightwave Technol.*, vol. 24, no. 12, pp. 4628–4641, Dec. 2006.

[59] J. P. Yao, “Microwave Photonics,” *J. Lightwave Technol.*, vol. 27, no. 3, pp. 314–335, Feb. 2009.

[60] J. P. Yao, “A tutorial on microwave photonics - Part I,” *IEEE Photon. Soc. Newsletter*, vol. 26, no. 2, pp. 4–12, Apr. 2012.

[61] J. P. Yao, “A tutorial on microwave photonics - Part II,” *IEEE Photon. Soc. Newsletter*, vol. 26, no.3, pp. 5–12, Jun. 2012.

[62] J. P. Yao, “Photonic generation of microwave arbitrary waveforms,” *Opt. Comm.*, vol. 284, no. 15, pp. 3723–3736, Jul. 2011.

[63] R. A. Minasian, E. H. W. Chan, and X. Yi, “Microwave photonic signal processing,” *Opt. Express*, vol. 21, no. 19, pp. 22918–22936, Sep. 2013.

[64] J. Capmany, J. Mora, I. Gasulla, and J. Sancho, “Microwave photonic signal processing,” *J. Lightw. Technol.*, vol. 31, no. 4, pp. 571–586, Feb. 2013.

[65] R. C. Daniels and R. W. Heath, “60 GHz wireless communications: Emerging requirements and design recommendations,” *IEEE Veh. Technol. Mag.*, vol. 2, no. 3, pp. 41–50, Sep. 2007

[66] R. Skaug and J. F. Hjelmstad, “Spread Spectrum in Communication,” London, U.K., 1985.

[67] A. W. Rihaczek, “Principles of High-Resolution Radar,” Norwood, MA: Artech House, 1996.

[68] H. Kwon and B. Kang, “Linear frequency modulation of voltage controlled oscillator using delay-line feedback,” *IEEE Microw. Wireless Compon. Lett.*, vol. 15, no. 6, pp. 431–433, Jun. 2005.

[69] H. D. Griffiths and W. J. Bradford, “Digital generation of high time bandwidth product linear FM waveforms for radar altimeters,” *IEE Proc-F*, vol. 139, no. 2, pp. 160–169, Apr. 1992.

[70] W. Li and J. P. Yao, “Generation of linearly chirped microwave waveform with an increased time-bandwidth product based on a tunable optoelectronic oscillator and a recirculating phase modulation loop,” *J. Lightw. Technol.*, vol. 32, no. 20, pp. 3573–3579, Oct. 2014.

[71] P. Ghelfi, F. Scotti, F. Laghezza, and A. Bogoni, “Photonic generation of phase-modulated RF signals for pulse compression techniques in coherent radars,” *J. Lightw. Technol.*, vol. 30, no. 11, pp. 1638–1644, Jun. 2012.

[72] H. Gao, C. Lei, M. Chen, F. Xing, H. Chen, and S. Xie, “A simple photonic generation of linearly chirped microwave pulse with large time bandwidth product and high compression ratio,” *Opt. Express*, vol. 21, no. 20, pp. 23107–23115, Oct. 2013.

[73] J.-W. Shi, F.-M. Kuo, N.-W. Chen, S. Y. Set, C.-B. Huang, and J. E. Bowers, “Photonic generation and wireless transmission of linearly/nonlinearly continuously tunable chirped

millimeter-wave waveforms with high time bandwidth product at W-band," *IEEE Photon. J.*, vol. 4, no. 1, pp. 215–223, Feb. 2012.

[74] A. Zeitouny, S. Stepanov, O. Levinson, and M. Horowitz, "Optical generation of linearly chirped microwave pulses using fiber Bragg gratings," *IEEE Photon. Technol. Lett.*, vol. 17, no. 3, pp. 660–662, Mar. 2005.

[75] J. D. McKinney, D. E. Leaird, and A. M. Weiner, "Millimeter-wave arbitrary waveform generation with a direct space-to-time pulse shaper," *Opt. Lett.*, vol. 27, no. 15, pp. 1345–1347, Aug. 2002.

[76] I. S. Lin, J. D. McKinney, and A. M. Weiner, "Photonic synthesis of broadband microwave arbitrary waveforms applicable to ultra-wideband communication," *IEEE Microw. Wireless Compon. Lett.*, vol. 15, no. 4, pp. 226–228, Apr. 2005.

[77] L. R. Chen, "Photonic generation of chirped microwave and millimeter wave pulses based on optical spectral shaping and wavelength-to-time mapping in silicon photonics," *Opt. Commun.*, 2015, DOI: 10.1016/j.optcom.2015.04.023.

[78] V. Torres Company, D. E. Leaird, and A. M. Weiner, "Dispersion requirements in coherent frequency-to-time mapping," *Opt. Express*, vol. 19, no. 24, pp. 24718–24729, Nov. 2011.

[79] C. Wang and J. P. Yao, "Photonic generation of chirped microwave pulses using superimposed chirped fiber Bragg gratings," *IEEE Photon. Technol. Lett.*, vol. 20, no. 11, pp. 882–884, Jun. 2008.

[80] C. Wang and J. P. Yao, "Large time-bandwidth product microwave arbitrary waveform generation using a spatially discrete chirped fiber Bragg grating," *J. Lightw. Technol.*, vol. 28, no. 11, pp. 1652–1660, Jun. 2010.

[81] R. Ashrafi, Y. Park, and J. Azana, "Fiber-based photonic generation of high-frequency microwave pulses with reconfigurable linear chirp control," *IEEE Trans. Microw. Theory Technol.*, vol. 58, no. 11, pp. 3312–3319, Nov. 2010.

[82] A. Rashidinejad and A. M. Weiner, "Photonic radio-frequency arbitrary waveform generation with maximal time-bandwidth product capability," *J. Lightw. Technol.*, vol. 32, no. 20, pp. 3383–3393, Oct. 2014.

[83] Y. Li, A. Rashidinejad, J.-M. Wun, D. E. Leaird, J.-W. Shi, and A. M. Weiner, "Photonic generation of W-band arbitrary waveforms with high time-bandwidth products enabling 3.9 mm range resolution," *Optica*, vol. 6, no. 1, pp. 446–454, Dec. 2014.

[84] D. Marpaung, C. Roeloffzen, R. Heideman, A. Leinse, S. Sales, and J. Capmany, "Integrated microwave photonics," *Lasers Photon. Rev.*, vol. 7, no. 4, pp. 506–538, Jul. 2013.

[85] M. Ferrera, Y. Park, L. Razzari, B. E. Little, S. T. Chu, R. Morandotti, D. J. Moss, and J. Azana, "On-chip CMOS-compatible all-optical integrator," *Nat. Commun.*, vol. 1, no. 29, pp. 1–5, May 2010.

[86] E. J. Norberg, R. S. Guzzon, J. S. Parker, L. A. Johansson, and L. A. Coldren, "Programmable photonic microwave filters monolithically integrated in InP-InGaAsP," *J. Lightw. Technol.*, vol. 29, no. 11, pp. 1611–1619, Jun. 2011.

[87] M. H. Khan, H. Shen, Y. Xuan, L. Zhao, S. Xiao, D. E. Leaird, A. M. Weiner, and M. Qi, "Ultrabroad-bandwidth arbitrary radiofrequency waveform generation with a silicon photonic chip-based spectral shaper," *Nat. Photon.*, vol. 4, no. 2, pp. 117–122, Feb. 2010.

[88] M. Ma, M. Rochette, and L. R. Chen, "Generating chirped microwave pulses using an integrated distributed Fabry–Perot cavity in silicon-on-insulator," *IEEE Photon. J.*, vol. 7, no. 2, art. no. 5500706, Apr. 2015.

[89] X. Xue, X. Zheng, H. Zhang, and B. Zhou, "Widely tunable single bandpass microwave photonic filter employing a non-sliced broadband optical source," *Opt. Express*, vol. 19, no. 19, pp. 18423–18429, Sep. 2011.

[90] J. Azaña, "Ultrafast analog all-optical signal processors based on fiber grating devices," *IEEE Photon. J.*, vol. 2, no. 3, pp. 359–386, Jun. 2010.

[91] H. Shahoei, P. Dumais, and J. P. Yao, "Continuously tunable photonic fractional Hilbert transformer using a high-contrast Germanium doped silica-on-silicon microring resonator," *Opt. Lett.*, vol. 39, no. 9, pp. 2778–2781, May 2014.

[92] A. Altaqui, E. H. W. Chan, and R. A. Minasian, "Microwave photonic mixer with high spurious-free dynamic range," *Appl. Opt.*, vol. 53, no. 17, pp. 3687–3695, Jun. 2014.

[93] W. Liu, W. Li, and J. P. Yao, "An ultra-wideband microwave photonic phase shifter with a full 360^{o} phase tunable range," *IEEE Photon. Technol. Lett.*, vol. 25, no. 12, pp. 1107–1110, Jun. 2013.

[94] R. Ashrafi, M. H. Asghari, J. Azana, “Ultrafast Optical arbitrary-order differentiators based on apodized long-period gratings,” *IEEE Photon. J.*, vol. 3, no. 3, pp. 353-364, Jun. 2011.

[95] J. P. Yao, F. Zeng, and Q. Wang, “Photonic generation of ultra-wideband signals,” *J. Lightw. Technol.*, vol. 25, no. 11, pp. 3219–3235, Dec. 2007.

[96] J. A. N. da Silva and M. L. R. de Campos, “Spectrally efficient UWB pulse shaping with application in orthogonal PSM,” *IEEE Trans. Commun.*, vol. 55, no. 2, pp. 313–322, Feb. 2007.

[97] F. Li, Y. Park, and J. Azaña, “Complete temporal pulse characterization based on phase reconstruction using optical ultrafast differentiation (PROUD),” *Opt. Lett.*, vol. 32, no. 22, pp. 3364–3366, Nov. 2007.

[98] C. Cuadrado-Laborde and M. V. Andrés, “In-fiber all-optical fractional differentiator,” *Opt. Lett.*, vol. 34, no. 6, pp. 833–835, Mar. 2009.

[99] C. Cuadrado-Laborde, “All-optical ultrafast fractional differentiator,” *Opt. Quantum Electron.*, vol. 40, no. 13, pp. 983–990, Mar. 2009.

[100] N. K. Berger, B. Levit, B. Fischer, M. Kulishov, D. V. Plant, and J. Azaña, “Temporal differentiation of optical signals using a phase-shifted fiber Bragg grating,” *Opt. Express*, vol. 15, no. 2, pp. 371–381, Jan. 2007.

[101] F. Liu, T. Wang, L. Qiang, T. Y. Zhang, M. Qiu, and Y. Su, "Compact optical temporal differentiator based on silicon microring resonator," *Opt. Express*, vol. 16, no. 20, pp. 15880–15886, Sep. 2008.

[102] K. A. Rutkowska , D. Duchesne , M. J. Strain , R. Morandotti , M. Sorel, and J. Azaña, "Ultrafast all-optical temporal differentiators based on CMOS-compatible integrated-waveguide Bragg gratings," *Opt. Express*, vol. 19, no. 20, pp. 19514–19522, Sep. 2011.

[103] H. Shahoei, D. Xu, J. Schmid, and J. P. Yao, "Tunable photonic fractional-order differentiator by coupling tuning of an SOI microring resonator," *IEEE Photon. Technol. Lett.*, vol. 25, no. 15, pp. 1408–1411, Aug. 2013.

[104] D. B. Hunter, M. E. Parker, and J. L. Dexter, "Demonstration of a continuously variable true-time delay beamformer using a multichannel chirped fiber grating," *IEEE Trans. Microw. Theory Tech.*, vol. 54, no. 2, pp. 861–867, Feb. 2006.

[105] Y. Liu, J. Yang, and J. P. Yao, "Continuous true-time-delay beamforming for phased array antenna using a tunable chirped fiber grating delay line," *IEEE Photon. Technol. Lett.*, vol. 14, no. 8, pp. 1172–1174, Aug. 2002.

[106] X. Dong, P. Shum, N. Q. Ngo, C. C. Chan, C. Zhao, and J. H. Ng, "A largely tunable CFBG-based dispersion compensator with fixed center wavelength," *Opt. Express*, vol. 11, no. 22, pp. 2970–2974, Nov. 2003.

[107] M. Pisco, S. Campopiano, A. Cutolo, and A. Cusano, “Continuously variable optical delay line based on a chirped fiber Bragg grating,” *IEEE Photon. Technol. Lett.*, vol. 18, no. 24, pp. 2551–2553, Dec. 2006.

[108] S. Yegnanarayanan, P. D. Trinh, F. Coppinger, and B. Jalali, “Compact Silicon-based integrated optics time delays,” *IEEE Photon. Technol. Lett.*, vol. 9, no. 5, pp. 634–635, May. 1997.

[109] J. P. Mack, E. F. Burmeister, H. N. Poulsen, B. Stamenic, J. E. Bowers, and D. J. Blumenthal, “Photonic integrated circuit switch matrix and waveguide delay lines for optical packet synchronization,” in 34th *European Conference on Optical Communication*, 2008, pp 1–2.

[110] J. B. Khurgin, “Expanding the bandwidth of slow light photonic devices based on coupled resonators,” *Opt. Lett.*, vol. 30, no. 5, pp. 513–515, Mar. 2005.

[111] J. Cardenas, M. Foster, N. Sherwood-Droz, C. Poitras, H. Lira, B. Zhang, A. Gaeta, J. B. Khurgin, P. Morton, and M. Lipson, “Wide-bandwidth continuously tunable optical delay line using silicon microring resonators,” *Opt. Express*, vol. 18, no. 25, pp. 26525–26534, Dec. 2010.

[112] Q. Xu, J. Shakya, and M. Lipson, “Direct measurement of tunable optical delays on chip analogue to electromagnetically induced transparency,” *Opt. Express*, vol. 14, no. 14, pp. 6463–6468, Jul. 2006.

[113] S. Khan, M. Baghban, and S. Fathpour, “Electronically tunable silicon photonic delay lines,” *Opt. Express*, vol. 19, no. 12, pp.11780–11785, Jun. 2011.

[114] S. Khan and S. Fathpour, “Complementary apodized grating waveguides for tunable optical delay lines,” *Opt. Express*, vol. 20, no. 18, pp. 19859–19867, Aug. 2012.

[115] I. Giuntoni, D. Stolarek, D. Kroushkov, J. Bruns, L. Zimmermann, B. Tillack, and K. Petermann, “Continuously tunable delay line based on SOI tapered Bragg gratings,” *Opt. Express*, vol. 20, no. 10, pp. 11241–11246, May. 2012.

[116] H. Shahoei, J. Albert, and J. P. Yao, "Optically tunable fractional order temporal differentiator using an optically pumped tilted fiber Bragg grating," *IEEE Photon. Technol. Lett.*, vol. 24, no. 9, pp. 370–372, May. 2012.

[117] F. Kong, W. Li, and J. Yao, “Transverse load sensing based on a dual-frequency optoelectronic oscillator,” *Opt. Lett.*, vol. 38, no. 14, pp. 2611–2613, Jul. 2013.

[118] H.-C. Kim, K. Ikeda, and Y. Fainman, “Tunable transmission resonant filter and modulator with vertical gratings,” *J. Lightw. Technol.*, vol. 25, no. 5, pp. 1147–1151, May 2007.

[119] I. Giuntoni, D. Stolarek, H. Richter, S. Marschmeyer, J. Bauer, A. Gajda, J. Bruns, B. Tillack, K. Petermann, and L. Zimmermann , “Deep-UV technology for the fabrication of Bragg gratings on SOI rib waveguides,” *IEEE Photon. Technol. Lett.*, vol. 21, no. 24, pp. 1894–1896, Dec. 2009.

[120] K. K. Lee, D. R. Lim, L. C. Kimerling, J. Shin, and F. Cerrina, "Fabrication of ultralow-loss Si/SiO_2 waveguides by roughness reduction," *Opt. Lett.*, vol. 26, no. 23, pp. 1888–1890, Dec. 2001.

[121] *Software: MODE Solutions*, Lumerical Solutions, Inc., Vancouver, BC, Canada, 2003.

[122] P. Dong, W. Qian, S. Liao, H. Liang, C. Kung, N. Feng, R. Shafiiha, J. Fong, D. Feng, A. V. Krishnamoorthy, and M. Asghari., "Low loss shallow-ridge silicon waveguides," *Opt. Express*, vol. 18, no. 14, pp. 14474–14479, Jul. 2010.

[123] F. Liu, T. Wang, L. Qiang, T. Y. Zhang, M. Qiu, and Y. Su, "Compact optical temporal differentiator based on silicon microring resonator," *Opt. Express*, vol. 16, no. 20, pp. 15880–15886, Sep. 2008.

[124] H. Shahoei, D.-X. Xu, J. H. Schmid, and J. P. Yao, "Photonic fractional- order differentiator using an SOI microring resonator with an MMI coupler," *IEEE Photon. Technol. Lett.*, vol. 25, no. 15, pp. 1408–1411, Aug. 2013.

[125] M. S. Nawrocka, T. Liu, X. Wang, and R. R. Panepucci, "Tunable silicon microring resonator with wide free spectral range," *Appl. Phys. Lett.*, vol. 89, no. 7, pp. 071110-1–071110-4, Aug. 2006.

[126] J. Dong, A. Zheng, D. Gao, L. Li, D. Huang, and X. Zhang, "Compact, flexible and versatile photonic differentiator using silicon Mach–Zehnder interferometers," *Opt. Express*, vol. 21, no. 6, pp. 7014–7024, Mar. 2013.

[127] H.-C. Kim, K. Ikeda, and Y. Fainman, "Resonant waveguide device with vertical gratings," *Opt. Lett.*, vol. 32, no. 5, pp. 539–541, Mar. 2007.

[128] Y. Painchaud, M. Aubé, G. Brochu, and M. Picard, "Ultra-narrowband notch filtering with highly resonant fiber Bragg gratings," in *Bragg Gratings, Photosensitivity, and Poling in Glass Waveguides*, OSA Tech. Dig., Art. ID BTuC3 (2010).

[129] A. W. Fang, E. Lively, Y. H. Kuo, D. Liang, and J. E. Bowers, "A distributed feedback silicon evanescent laser," *Opt. Express*, vol. 16, no. 7, pp. 4413-4419, Mar. 2008.

[130] J. Sun, Purnawirman, E. S. Hosseini, J. D. B. Bradley, T. N. Adam, G. Leake, D. Coolbaugh, and M. R. Watts, "Uniformly spaced λ/4-shifted Bragg grating array with wafer-scale CMOS-compatible process," *Opt. Lett.*, vol. 38, no. 20, pp. 4002–4004, Oct. 2013.

[131] X. Zou, M. Li, L. Yan, J. Azana, and J. P. Yao, "All-fiber optical filter with an ultra-narrow and rectangular spectral response," *Opt. Lett.*, vol. 38, no. 16, pp. 3096–3098, Aug. 2013.

[132] Y. Wang, J. Flueckiger, C. Lin, and L. Chrostowski, "Universal grating coupler design," *Proc. SPIE, Photonics North*, 89150Y (2013).

[133] Y. Zhang, S. Yang, A. E.-J. Lim, G.-Q. Lo, C. Galland, T. Baehr-Jones, and M. Hochberg, "A compact and low loss Y-junction for submicron silicon waveguide," *Opt. Express*, vol. 21, no. 1, pp. 1310–1316, Jan. 2013.

[134] Q. Xu, B. Shmidt, S. Pradhan, and M. Lipson, "Micrometre-scale silicon electro-optic modulator," *Nature*, vol. 435, no. 7040, pp. 325–327, May. 2005.

[135] M. Li, L. Shao, J. Albert, and J. P. Yao, "Continuously tunable photonic fractional temporal differentiator based on a tilted fiber Bragg grating," *IEEE Photon. Technol. Lett.*, vol. 23, no. 4, pp. 251–253, Feb. 2011.

[136] M. Spasojevic and L. R. Chen, "Discretely tunable optical delay lines using serial and step-chirped sidewall Bragg gratings in SOI," *Electron. Lett.*, vol. 49, no. 9, pp. 608–610, Apr. 2013

[137] D. K. Hunter, M. C. Chia, and I. Andonovic, "Buffering in optical packet switches," *J. Lightw. Technol.*, vol. 16, no. 12, pp. 2081–2094, Dec. 1998.

[138] S. Blais and J. Yao, "Photonic true-time delay beamforming based on superstructured fiber Bragg gratings with linearly increasing equivalent chirps," *J. Lightw. Technol.*, vol. 27, no. 9, pp. 1147–1154, May, 2009.

[139] A. Melloni, A. Canciamillia, C. Farrari, F. Morichetti, L. Faolain, T. Krauss, R. De La Rue, A. Samarelli, and M. Sorel, "Tunable delay lines in silicon photonics: Coupled resonators and photonic crystals, a comparison," *IEEE Photon. J.*, vol. 2, no. 2, pp. 181–194, Apr. 2010.

[140] W. Bogaerts and S. K. Selvaraja, "Compact single-mode silicon hybrid rib/strip waveguide with adiabatic bends," *IEEE Photon. J.*, vol. 3, no. 3, pp. 422–432, Jun. 2011.

[141] S. Mallet, “A Wavelet Tour Signal Processing,” San Diego, CA, USA: Academic, 1999.

[142] R. Ashrafi, Y. Park, and J. Azana, “Fiber-based photonic generation of high-frequency microwave pulses with reconfigurable linear chirp control,” *IEEE Trans. Microw. Theory Tech.*, vol. 58, no. 11, pp. 3312–3319, Nov. 2010.

[143] M. Li and J. P. Yao, “Photonic generation of continuously tunable chirped microwave waveforms based on a temporal interferometer incorporating an optically-pumped linearly-chirped fiber Bragg grating,” *IEEE Trans. Microw. Theory Tech.*, vol. 59, no. 12, pp. 3531–3537, Dec. 2011.

[144] A. Rashidinejad and A. M. Weiner, “Photonic radio-frequency arbitrary waveform generation with maximal time-bandwidth product capability,” *J. Lightw. Technol.*, vol. 32, no. 20, pp. 3383–3393, Oct. 2014.

[145] J. Klauder, A. Price, S. Darlington, and W. Albersheim, “The Theory and Design of Chirp Radars,” *BSTJ*, vol. 39, pp. 745–808, Jul. 1960.

[146] H. Yun, W. Shi, Y. Wang, L. Chrostowski, and N A. F. Jaeger, “2×2 adiabatic 3-dB coupler on silicon-on-insulator rib waveguides,” *Proc. SPIE Photon. North*, vol. 8915, pp. 89150V, May 2013.

[147] G. Agrawal, “Fiber-Optic Communication Systems,” 3rd Edition, Wiley, 2002.

[148] Y. Park, M. Scaffardi, L. Potì, and J. Azaña, "Simultaneous singleshot real-time measurement of the instantaneous frequency and phase profiles of wavelength-division-multiplexed signals," *Opt. Express*, vol. 18, no. 6, pp. 6220–6229, Mar. 2010.

[149] M. Li and J. P. Yao, "Multichannel arbitrary-order photonic temporal differentiator for wavelength-division-multiplexed signal processing using a single fiber Bragg grating," *J. Lightw. Technol.*, vol. 29, no. 17, pp. 2506–2511, Sep. 2011.

[150] Y. Zhang, S. Yang, A. E.-J. Lim, G.-Q. Lo, C. Galland, T. Baehr-Jones, and M. Hochberg, "A compact and low loss Y-junction for submicron silicon waveguide," *Opt. Express*, vol. 21, no. 1, pp. 1310–1316, Jan. 2013.

[151] Q. Chang, Q. Li, Z. Zhang, M. Qiu, T. Y, and Y. Su, "A tunable broadband photonic RF phase shifter based on a silicon microring resonator," *IEEE Photon. Technol. Lett.*, vol. 21, no. 1, pp. 60–62, Jan. 2009.

[152] L.-W. Luo, G. Wiederhecker, K. Preston, and M. Lipson, "Power insensitive silicon microring resonators," *Opt. Lett.*, vol. 37, no. 4, pp. 590–592, Feb. 2012.

[153] W. H. P. Pernice, C. Schuck, M. Li, and H. X. Tang, "Carrier and thermal dynamics of silicon photonic resonators at cryogenic temperatures," *Opt. Express*, vol. 19, no. 4, pp. 3290–3296, Feb. 2011.

[154] M. R. Watts, W. Zortman, D. Trotter, R. Young, and A. Lentine, "Vertical junction silicon microdisk modulators and switches," *Opt. Express*, vol. 19, no. 22, pp. 21989–22003, Oct. 2011.

[155] L. Zhou and A. W. Poon, "Silicon electro-optic modulators using p-i-n diodes embedded 10-micron-diameter microdisk resonators," *Opt. Express*, vol. 14, no. 15, pp. 6851–6857, Jul. 2006.

[156] S. M. Grist, S. A. Schmidt, J. Flueckiger, V. Donzella, W. Shi, S. Talebi Fard, J. T. Kirk, D. M. Ratner, K. C. Cheung, and L. Chrostowski, "Silicon photonic micro-disk resonators for label-free biosensing," *Opt. Express*, vol. 21, no. 7, pp. 7994–8006, Apr. 2013.

[157] M. Borselli, T. J. Johnson, and O. Painter, "Beyond the Rayleigh scattering limit in high-Q silicon microdisks: theory and experiment," *Opt. Express*, vol. 13, no. 5, pp. 1515–1530, Mar. 2005.

[158] M. Borselli, K. Srinivasan, P. E. Barclay, and O. Painter, "Rayleigh scattering, mode coupling, and optical loss in silicon microdisks," *Appl. Phys. Lett.*, vol. 85, no. 17, pp. 3693–3695, Oct. 2004.

[159] F. Xia, M. Rooks, L. Sekaric, and Y. Vlasov,"Ultra-compact high-order ring resonator filters using submicron silicon photonic wires for on-chip optical interconnects," *Opt. Express*, vol. 15, no. 19, pp. 11934–11941, Sep. 2007.

[160]A. V. Krishnamoorthy, R. Ho, X. Zheng, H. Schwetman, J. Lexau, P. Koka, G. Li, I. Shubin, and J. Cunningham, "Computer systems based on silicon photonic interconnect," *Proc. IEEE*, vol. 97, no. 7, pp. 1337–1361, Jul. 2010.

[161] T. Kato and Y. Kokubun, "Bessel-Thompson filter using double-series- coupled microring resonator," *J. Lightwave Technol.*, vol. 26, no. 22, pp. 3694–3698, Nov. 2008.

PUBLICATION

Journal paper

[13] **W. Zhang** and J. P. Yao, "Silicon-Based On-Chip Electrically-Tunable Spectral Shaper for Continuously Tunable Linearly Chirped Microwave Waveform Generation," *IEEE/OSA J. Lightw. Technol*., vol. 34, no. 20, pp. 4664-4672, Oct. 2016. (**Invited**)

[12] **W. Zhang** and J. P. Yao, "Electrically-tunable silicon-based on-chip microdisk resonator for integrated microwave photonic applications," *APL Photonics*, vol. 1, no. 8, 080801, Nov. 2016. (**Invited**)

[11] **W. Zhang** and J. P. Yao, "Optically tunable Fano resonance in a grating-based Fabry-Perot cavity-coupled microring resonator on a silicon chip," *Opt. Lett*., vol. 41, no. 11, pp. 2474-2477, Jun. 2016.

[10] **W. Zhang** and J. P. Yao, "Silicon-based integrated microwave photonics," *IEEE J. Quantum Electron.*, vol. 52, no. 1, 0600412, Jan. 2016. (**Invited**)

[9] **W. Zhang** and J. P. Yao, "Photonic Generation of Linearly Chirped Microwave Waveforms Using a Silicon-Based On-Chip Spectral Shaper Incorporating Two Linearly Chirped Waveguide Bragg Gratings," *IEEE/OSA J. Lightw. Technol*., vol. 33, no. 24, pp. 5047-5054, Dec. 2015.

[8] J. Zhang, **W. Zhang** and J. P. Yao, "Ultrafast three-dimensional serial time-encoded imaging with high vertical resolution," *IEEE/OSA J. Lightw. Technol*., vol. 33, no. 22, pp. 4622-4626, Nov. 2015

[7] N. Ehteshami, **W. Zhang**, and J. P. Yao, "Optically tunable full 360^{o} microwave photonic phase shifter using three cascaded silicon-on-insulator microring resonators," *Opt. Comm*., accepted.

[6] **W. Zhang**, N. Ehteshami, W. Liu, and J. P. Yao, "Silicon-based on-chip electrically tunable sidewall-Bragg-grating Fabry-Perot filter," *Opt. Lett.*, vol. 40, no. 13, pp. 3153-3156, Jun. 2015

[5] **W. Zhang**, W. Li, H. Shahoei, and J. P. Yao, "Independently tunable multi-channel fractional-order temporal differentiator based on a silicon-photonic symmetric Mach-Zehnder interferometer incorporating cascaded microring resonators," *IEEE/OSA J. Lightw. Technol.*, vol. 33, no. 2, pp. 361-367, Jan. 2015.

[4] **W. Zhang**, W. Li and J. P. Yao, "All-optical temporal differentiator based on an integrated sidewall phase-shifted Bragg grating," *IEEE Photon. Technol. Lett*., vol. 26, no. 23, pp. 2383-2386, Dec. 2014.

[3] **W. Zhang** and J. P. Yao, "Ultra-wideband RF photonic phase shifter using two cascaded polarization modulators," *IEEE Photon. Technol. Lett*., vol. 26, no. 9, pp. 911-914, May 2014.

[2] W. Li, **W. Zhang**, and J. P. Yao, "A wideband 360^{o} photonic-assisted microwave phase shifter using a polarization modulator and a polarization-maintaining fiber Bragg grating," *Opt. Express*, vol. 20, no. 28, pp. 29838-29843, Dec. 2012.

[1] **W. Zhang** and J. P. Yao, "Photonic generation of millimeter-wave signals with tunable phase shift," *IEEE Photon. J.*, vol. 4, no. 3, pp. 889-894, Jun. 2012.

Conference papers

[10] **W. Zhang** and J. P. Yao, “Silicon-based on-chip electrically tunable phase-shifted waveguide Bragg grating for integrated microwave photonic applications," MWP2016, Long Beach, California, USA, Oct. 2016. (**Best Student Paper**)

[9] **W. Zhang** and J. P. Yao, “Silicon-based on-chip microdisk resonators for integrated microwave photonic applications,” OFC2016, M2B.6, Anaheim Convention Center, Anaheim, California, USA, 20-24 Mar. 2016.

[8] **W. Zhang** and J. P. Yao, "Photonic generation of linearly chirped microwave waveform with a large time-bandwidth product using a silicon-based on-chip spectral shaper," MWP2015, 26-29 Oct. 2015, Paphos, Cyprus. (**Best Student Paper**)

[7] N. Ehteshami, **W. Zhang**, and J. P. Yao, "Optically tunable single passband microwave photonic filter based on phase-modulation to intensity-modulation conversion in a silicon-on-Insulator microring resonator," MWP2015, 26-29 Oct. 2015, Paphos, Cyprus.

[6] **W. Zhang** and J. P. Yao, "All-optically controlled Fabry-Perot cavity-assisted add-drop microring resonator on a silicon chip," CLEO 2015, 10-15 May 2015, San Jose, USA, paper SM3I.3.

[5] W. Liu, **W. Zhang**, and J. P. Yao, "A bandstop microwave photonic delay-line filter with both tunable stop-band rejection ratio and tunable frequency," IMS 2015, TU3G-1, 17-22 May 2015, Phoenix, Arizona, USA.

[4] **W. Zhang** and J. P. Yao, "Largely chirped microwave waveform generation using a silicon-based on-chip optical spectral shaper," MWP2014, Sapporo, Japan, 20-23 Oct. 2014.

[3] W. Li, **W. Zhang**, and J. P. Yao, "Frequency-hopping microwave waveform generation based on a frequency-tunable optoelectronic oscillator," OFC 2014, 9-13 March 2014, San Francisco, USA, paper W1J.2.

[2] W. Li, **W. Zhang**, and J. P. Yao "An ultra-wideband 360^{o} photonic-assisted microwave phase shifter," OFC 2013, 17-21 March 2013, Anaheim, CA, USA.

[1] **W. Zhang** and J. P. Yao, "Photonic generation of millimeter-wave signals with tunable phase shift," MWP 2012,11-14 September 2012, Amsterdam, The Netherlands.